

Optical Information Processing

Thesis by

Christophe Moser

In Partial Fulfillment of the Requirements

for the Degree of

Doctor of Philosophy



California Institute of Technology

Pasadena, California

2001

(Submitted December 1, 2000)

To my family

Acknowledgements

When I came to Caltech in 1995 as a visitor from industry on a generous one-year grant from the Swiss Academy of Engineering Science (SATW), my intention was to get to know a different way of life and to be exposed to the best science of a top institution. I immediately felt good in this environment thanks to my close friends at the vision lab, directed by Professor Pietro Perona. In particular, J-Y Bouguet, Enrico Di Bernardo, Luis Goncalves and Mario Munich helped me tremendously with their kindness and friendship.

I have always been fascinated by the field of optics. Prof. Demetri Psaltis welcomed me in his group to work on a project involving optics and vision. I am very grateful to Prof. Psaltis for believing in me from the start. A former student in the group, George Barbastathis, now professor at MIT, is another key person that I would like to thank for his support. Prof. Psaltis and George encouraged me to pursue a Ph.D. and my year stay turned into five years. It was a wonderful experience that I am glad to have undertaken. Demetri has been a patient and very creative advisor always available for discussion and advice. He has become a good friend and mentor along the years as well. During the course of the Ph.D., I encountered periods of excitement and periods of doubt. I found that perseverance and optimism are necessary ingredients to overcome difficult moments. My girlfriend, Melissa, has always been a motivator at my side revitalizing my mood with her everlasting smile and love.

I would like to thank more people that I have interacted with during my Ph.D.: Professors Ali Adibi and Prof. Karsten Buse for their insight on doubly doped lithium niobate; Professor George Barbastathis for his contribution in the three-dimensional conoscopic sensor; Michael Levene, Greg Steckman, Ernest Chuang, Greg Billock, Xin An, Allen Pu, Jean-Jacques Drolet, Jose Mumbru, George Panotopoulos, Yun-

ping Yang and visiting professor Nam Kim for fruitful discussions; Professor Anshel Gorokovsky, from CUNY, for his guidance on spectral hole burning; Wenhai Liu and Zhiwen Liu for their contribution to the spectral hole burning project and Iouri Solomatine for preparing the polymer samples; Benjamin Schupp, who helped me during his diploma work; and Irena Maravic for the experiments on localized recording.

Special thanks go to Lucinda Acosta for adding an atmosphere of fiesta, not only during Cinco de Mayo, but all year long. I owe her all the funny nicknames: "Mosero," "Moserito," "Suizo Ranchero" and many more... I also thank Yayun Liu who runs the organization of the labs perfectly and for her kindness to me.

To my roommate Alfredo Fontanini and many others who have lived in the always lively 965 E. Del Mar. And to Alberto Pesavento for the enjoyable golf games at the Rosebowl.

My warmest thoughts go to my family: my parents, sister (with the 'beauf'!) who have supported me with their love and affection during all these years of study and to whom I dedicate this work. Finally, I dedicate this to my nephew of two years old, Hugo, who is making many more discoveries than I do everyday!

Abstract

The title of this work *Optical Information Processing* reflects the multi-facets of this thesis.

In the first three chapters, I look at specific aspects of optical data storage. Enabled by new recording materials, a read-write holographic memory is explored. The memory combines a two-dimensional layered architecture and holography. Recording dynamics are analyzed and compared with conventional memories. A novel multiplexing method, based on the confinement of spherical waves in waveguides, allows the implementation of flat read-only memories with no moving parts. Novel polymer films at low temperatures show extremely selective frequency absorption which yields up to hundred thousands of independent frequency channels. This radically different multiplexing scheme is combined with Bragg multiplexing to increase the storage density. Femtosecond pulses can be stored and retrieved in these materials. For further processing, a pulse shaper and an all-optical logic capable of processing Terahertz pulse streams are experimentally demonstrated.

The last two chapters look at three-dimensional surface measurements. A profilometer and a wavefront sensor based on the propagation of light in birefringent crystals are investigated. The performance of both sensors is theoretically modeled and experimentally verified. A third sensor is designed for an ophthalmic application.

Contents

Acknowledgements	iv
Abstract	vi
1 Introduction	1
2 Holographic recording of localized holograms	5
2.1 Recording in LiNbO ₃ :Fe:Mn crystals	7
2.2 Recording speed of localized holograms	12
2.3 Maximum diffraction efficiency of localized holograms	22
2.3.1 Effect of finite recording time	29
2.4 Physical justification of the 1/M dependence	36
2.5 Characterization of an optical memory based on localized recording .	41
2.5.1 SNR of localized holograms	44
2.5.2 Selective erasure cycles	52
2.5.3 Phase conjugate implementation	55
2.5.4 Memory capacity	59
2.6 Pulse shaping	62
3 Folded shift multiplexing	70
3.1 Shift multiplexing	70
3.2 Folded shift multiplexing	75
4 Spectral hole-burning in naphthalocyanine derivatives in the 800 nm region for holographic storage applications	87
4.1 Introduction	87
4.2 Material preparation	92

4.2.1	Hole burning properties	93
4.2.2	Holographic storage	98
4.3	M/# of absorption and index holograms in SHB media	102
4.3.1	Absorption kinetics	103
4.3.2	M/# of pure absorption holograms	105
4.3.3	M/# of pure index holograms	107
4.4	Ultra fast all-optical logic	112
4.4.1	Principle	113
4.4.2	Experimental gates	115
4.4.3	AND gate	116
4.4.4	OR gate	117
4.4.5	XOR gate	118
4.4.6	Cascading gates	119
4.4.7	Optical computation	121
5	Three-dimensional measurement using conoscopic patterns	124
5.1	Introduction	124
5.2	Theory	125
5.2.1	Path difference in the tilted crystal geometry	126
5.2.2	Analytical expression of the path difference	130
5.3	Profilometer	132
5.3.1	Fringe interpolation	136
5.3.2	Application: corneal curvature change	137
5.4	3-D measurements using shear conoscopy	140
5.4.1	Introduction	140
5.4.2	Phase extraction from a shear interferogram	141
6	Feasibility study of Intraoperative Corneal Topography Monitoring During Photorefractive keratectomy	148
6.1	Introduction	148
6.2	Material and methods	149

6.3	Results	155
6.3.1	Performance of the topographer	155
6.3.2	Topographer accuracy on test sphere	155
6.3.3	Topographer accuracy on de-epithelialized swine eyes in vitro .	157
7	Conclusion	162
A	moving-edge method	164
	Bibliography	166

List of Figures

2.1	Basic holographic recording system. SLM: Spatial Light Modulator. R: reference beam. S: Signal beam.	5
2.2	Band diagram of LiNbO ₃ doped with iron (left) and doubly doped with iron and manganese (right). CB: conduction band; VB: valence band. Both elements occur in two valence states. Electrons are excited from Fe ²⁺ by visible light and ultra violet light and from Mn ²⁺ by ultra violet-light only. Free electrons in the CB can recombine with Fe ³⁺ or Mn ³⁺	8
2.3	Recording and non-destructive read-out processes. The plot represent light intensities I for visible and ultra violet light and the concentration of electrons N trapped in the iron (Fe ²⁺) and manganese (Fe ²⁺) centers against the spatial dimension x directed along the grating vector. . .	11
2.4	Localized recording in doubly doped LiNbO ₃	13
2.5	Recording set-up for the 50 holograms experiment. The camera CCD and detector are interchangeable.	14
2.6	(a) 50 images recorded in a LiNbO ₃ :Fe,Mn crystal. Each peak corresponds to the diffraction efficiency of a hologram stored at a different spatial location as the crystal is translated in the direction perpendicular to the reference beam. Center to center spacing between each hologram is 80μm (b) Hologram #25 is selectively erased by continuous illumination of UV and red reference.	16
2.7	Localized and distributed recording system. The relevant diffraction efficiency is given by the power ratio: $\frac{\text{diffracted power}}{\text{input power}}$	18
2.8	Ratio of total recording time between the localized and the distributed volume methods in function of the number of holograms to record for two different values of the ratio $\frac{\tau_e}{\tau_w}$ and $t_1 = \frac{\tau_e}{20}$	21

2.9	Recording set-up. The half wave plate positioned before the polarizing beam-splitter distributes the power between the reference and signal beam. The waveplate is mounted on a rotation stage for continuous power distribution.	23
2.10	Recording curves of a localized hologram. The dashed curve is recorded with equal power. The plain curve is recorded with equal intensity in the reference and signal beam. The lateral extension of the reference beam is 50 times smaller than the signal diameter.	24
2.11	Ratio of saturation diffraction efficiency between localized holograms recorded with equal intensity and localized holograms recorded with equal power in function of the number of holograms $M = L/L'$	26
2.12	Power distribution during recording between reference and signal beam represented by the parameter $\alpha = P_r/(P_r + P_s)$	27
2.13	Recording with continuous power distribution between reference and signal beam (solid curve) for a number of holograms M equal to 50. The dashed curves for equal power and equal intensity recording are shown for comparison.	28
2.14	Diffraction efficiency η in doubly doped $\text{LiNbO}_3:\text{Fe},\text{Mn}$ as a function of the ratio τ_e/τ_ω . The two sets of curves correspond to a number of recorded holograms equal to 50 and 1000.	32
2.15	Exposure schedule computed from eqn. 4.11 for $M=1000$ holograms. .	33
2.16	Set-up for the 50 strong holograms recording. LD: laser diode; PBS: polarizing beam splitter.	34
2.17	Diffraction efficiency η versus spatial location. (i) η of each localized hologram measured immediately after each recording; (ii) η measured after the recording of 50 holograms.	35
2.18	Diffraction efficiency η versus angle for 50-angle-multiplexed holograms. 36	
2.19	Vectorial sum of the grating vectors produced by the interference of two plane waves. (a) coherent addition; (b) random walk.	38
2.20	Recording set-up for the SNR measurement.	42

2.21	Recording and read-out curve for a plane wave hologram in a 90 degree-cut LiNbO ₃ crystal doped with 0.15 wt. % Fe ₂ O ₃ and 0.015 wt. % MnO. The recording beams are from a solid state green laser (wavelength 532 nm, ordinary polarization, $1/e^2$ beam diameter 2.0 mm and intensity 80 mW/cm ² per beam). The sensitizing light is from a laser diode (Nichia, wavelength 401 nm, linearly polarized, intensity 20 mW/cm ²).	43
2.22	Spectrum of the 90 degree crystal used in the SNR experiment (#86D, 0.15 wt. % Fe ₂ O ₃ and 0.015 wt. % MnO) and 778-12 (0.075 wt. % Fe ₂ O ₃ and 0.015 wt. % MnO).	44
2.23	a) Recording curves with a focused reference green beam (wavelength=532 nm, spot size=30 μ m ($1/e^2$ value)) and erasing with reference beam only. The different curves are recorded with increasing exposure. b) Persistence β^2 as a function of recording time.	45
2.24	Recording of 40 localized holograms. The plot shows the diffraction efficiency versus the spatial shift of the crystal.	47
2.25	Recording of 100 localized holograms. The plot shows the diffraction efficiency versus the spatial shift of the crystal.	48
2.26	Three sample reconstructions and SNR values from the 40 holograms.	49
2.27	Three sample reconstructions and SNR values from the 100 holograms experiment.	50
2.28	SNR comparison: (a) direct imaging; (b) imaging through crystal; (c) after 40 holograms.	51
2.29	SNR comparison: (a) direct imaging; (b) imaging through; crystal(c) first hologram; (d) after 100 holograms	52
2.30	Diffraction efficiency vs spatial shift before and after 55 refresh cycles of the central hologram - - 100 μ m reference focus.	53
2.31	Histogram and reconstruction of the central hologram before and after the refresh cycle - 100 μ m focus.	54
2.32	Diffraction efficiency vs spatial shift before and after 55 refresh cycles of the central hologram - 25 μ m reference focus.	55

2.33	Histogram and reconstruction of the central hologram before and after the refresh cycle - $25\mu\text{m}$ focus	56
2.34	Experimental set-up of the phase conjugate memory module. WP= half wave plate. BSP= polarizing beam splitter. Cl= cylindrical lens.	57
2.35	Spatial selectivity of the forward and conjugate reconstruction.	58
2.36	Compact module using a mirror for phase conjugation. Also shown is the spatial selectivity of the forward and conjugate reconstruction. . .	59
2.37	Reconstructed hologram by phase conjugation.	60
2.38	Memory capacity of the phase conjugate module.	61
2.39	Reflection geometry for temporal pulse shaping. The writing beams are plane waves interfering in the medium producing a grating vector in the direction of the read beam propagation.	62
2.40	Pulse shaping recording set-up.	64
2.41	Second order autocorrelation of the probe beam in a BBO crystal. . .	65
2.42	Linear cross correlation with the femtosecond source pulse and the diffracted pulse. a) grating with no modulation; b) grating with amplitude modulation.	66
2.43	First order correlation between the probe beam and signal beams. The probe beam and signal beam recombine with a small angle in order to produce a visible fringe pattern on the CCD camera. The DC components are subtracted from the image.	68
2.44	Pulse shaping recording system in waveguides. A photolithographic ultra-violet projection system sensitize the waveguide with sub-micrometer feature size.	69
3.1	Angle multiplexing.	72
3.2	K-sphere representation.	73
3.3	Numerical computation of the diffraction efficiency as a function of the incident beam angle.	74

3.4	(a) Shift multiplexing in the 90-degree geometry; (b) Shift multiplexing by total internal reflection in a crystal slab.	76
3.5	Recording geometry and notation.	77
3.6	Wavefront versus propagation distance in the slab. The dashed curve represents a perfect spherical wavefront and the plain curve represent the wavefront unfolded from total internal reflection in the slab. The phase change after reflection is magnified by 1000 to note the deformation.	78
3.7	Shift selectivity for different locations z_i ($i=1,2,3$) along the slab. Numerical aperture (N.A) of the reference wave is 0.18.	79
3.8	Shift selectivity for different locations z_i ($i=1,2,3$) along the slab. Numerical aperture (N.A) of the reference wave is 0.65.	80
3.9	Set-up for the shift multiplexed 50 holograms.	81
3.10	Read-out of 50 shift multiplexed holograms in the slab crystal.	82
3.11	a) Pattern imaged through the crystal slab. b) Sample reconstruction of hologram #20.	83
3.12	Implementation of a read-only memory based on folded shift multiplexing in thin slabs.	84
4.1	Wavelength selective absorption by chromophores embedded in a polymer host. The optical transition of the chromophores depends on the local surrounding environment.	89
4.2	Diffracted field from an absorption grating $\alpha_1(\omega)$ and the corresponding index of refraction $n_1(\omega)$ grating obtained from the Krmaers-Kronig relation.	90
4.3	Chemical structures of four chromophores. (a) 2,11,20,29-tetra-tert-butyl-2,3-naphthalocyanine (H_2 -TBNP). (b) zinc 2,11,20,29-tetra-tert-butyl-2,3-naphthalocyanine (Zn-TBNP). (c) nickel 2,11,20,29-tetra-tert-butyl-2,3-naphthalocyanine (Ni-TBNP). (d) silicon 2,3-naphthalocyanine dioctyloxide (Si-NPDO).	93
4.4	Absorption spectra of several naphthalocyanines at 8 K.	94

4.5	Normalized spectral hole profiles for Zn-TBNP at 1.5 K at different exposure with burning intensity of 192 mW/cm ²	95
4.6	Hole burning kinetics for H ₂ -TBNP (a) and Zn-TBNP (b) at 1.5 K. (a.1). Experimental kinetics recorded using a laser diode with intensity 0.2 mW/cm ² for the sample with concentration 7·10 ⁻⁴ mol/l. (a.2) Experimental kinetics recorded with intensity of 192 mW/cm ² . (a.3) All fitting curves used $a = 0.9$ and $s = 2.6 \cdot 10^{-11}$ cm ² . Experimental kinetics recorded with intensities (b.1) 192 mW/cm ² and (b.2) 10 mW/cm ² . The corresponding fitting curves were obtained by fitting simultaneously both experimental datasets with the same values of a_c , w , and D , and the proper burning intensity for each dataset. Both fitting curves used $a = 0.9$ and $s = 1.7 \cdot 10^{-11}$ cm ²	97
4.7	Experimental set-up for the hologram recording. The mask, composed of random binary pixels, is imaged onto the sample inside the cryostat by a 4f system and is recorded with a plane wave reference.	100
4.8	Holograms of random bit patterns 100×100 μm recorded in three polymer films at 1.9 K: a) 400 μm TBN in PVB matrix (788 nm). b) 400 μm SiNDO in PVB matrix (777 nm). c) 1.5 mm TBN in polystyrene (788nm).	101
4.9	Diffraction efficiency η versus normalized recording time t/KI_o for M multiplexed holograms. The recording time t is constant for all exposures.	106
4.10	$M\#$ for absorption holograms. The wavelength of the writing and reading beam is unchanged ($\lambda_{write} = \lambda_{read}$).	107
4.11	$M\#$ comparison between pure absorption holograms and Π -holograms when the non-burnable background absorption is equal to zero ($B=0$).	109
4.12	$M\#$ versus optical density when multiplexing Π -holograms. The parameter B is the non-burnable background absorption.	110
4.13	$M\#$ versus optical density derived from the experimental absorption kinetics shown in the inset of the plot.	111

4.14	Principle of the all-optical gate by second harmonic generation. . . .	113
4.15	Amplitude coding.	114
4.16	Boolean representation of the system shown in fig. 4.14.	115
4.17	Experimental set-up describing the implementation of the optical gates. The beam splitters BS_1, \dots, BS_3 and delay lines $D_1 \dots D_4$ are used to generate the set of inputs. The singlet lens is used as a position dependent focal length. The frequency-doubled light generated by pairs of inputs interfere and serve as the basis for the optical gates.	116
4.18	Picture of the experimental set-up shown in fig. 4.17.	117
4.19	Experimental truth table of the optical AND gate.	118
4.20	OR gate.	118
4.21	Experimental truth table of the optical OR gate.	119
4.22	Experimental truth table of the optical XOR gate.	120
4.23	Amplitude modulation by photoinduced absorption.	121
4.24	Relaxation time of photoinduced excitation in PMBPA polymers. . .	121
4.25	Implementation of a 2 bit adder using the optical gates developed in this section.	123
5.1	Interference between the ordinary and extraordinary rays in a birefringent crystal. The incident light is polarized. After the analyzer is placed at the output, the so-called conoscopic pattern is produced. The pattern consists of concentric disks of alternating low and high intensities.	125
5.2	Geometry illustrating the use of a lens and a tilted crystal to increase the conoscopic resolution.	127
5.3	Experimental measurement set-up of the path difference $G(x)$ described by eqn. 5.10.	129
5.4	Conoscopic pattern produced by the set-up of fig. 5.3. A cross section of the conoscopic pattern is shown to fit with theory.	130
5.5	A cross section of the conoscopic pattern is shown to fit with theory.	131

5.6	Plots of the path difference using the approximation (eqn. 5.13) and the exact expression (eqn. 5.10) for a crystal tilt angle of 25 degrees .	132
5.7	Plots of the path difference using the approximation (eqn. 5.13) and the exact expression (eqn. 5.10) for a crystal tilt angle of 35 degrees.	133
5.8	Depth resolution of the scanning conoscopic system as a function of the crystal tilt angle and the focal length of the collimated lens. . . .	134
5.9	Depth resolution of the scanning conoscopic system as a function of the crystal tilt angle and the crystal thickness.	135
5.10	Function $D(\psi)=\frac{C(\psi)}{\cos(\psi)}$ versus crystal tilt angle ψ	136
5.11	Fringe interpolation by subtraction of two translated interferograms.	137
5.12	Subtracted interferograms with increasing defocus.	138
5.13	Curvature measurement set-up.	139
5.14	Experimental measurement of curvature change by translating a plastic cornea.	140
5.15	The incident wavefront is laterally sheared by double refraction in a birefringent crystal.	142
5.16	Five phase shifted conoscopic interferograms.	144
5.17	Phase difference $w(x, y)$ computed with the phase shifting method. .	145
5.18	3-D extraction of an aspherical surface using the shear lateral interferometer and the hermite polynomial expansion. The plot shows the wavefront reconstruction.	146
5.19	Measured wavefront difference between the lateral shear interferometer and the Twyman-Green interferometer.	147
6.1	Topographer principle. Projection and triangulation are used to measure the three-dimensional shape of the object.	150
6.2	Binary fringe patterns of increasing spatial frequency projected by the SLM.	151
6.3	Example of a fringe pattern and its video inverse. Subtraction yields zero mean signal.	152

6.4	Modification of the system to reduce the effect of scattering on images of projected fringes.	153
6.5	Prototype of the topographer under the VISX excimer laser at the Doheny Eye Institute facility.	154
6.6	Histogram showing the shift between extracted feature points before and after translating the sphere by 2 micrometers.	155
6.7	Elevation map of the test sphere.	156
6.8	Spurious scattering by fibrils within the cornea and by the anterior surface of the cornea.	157
6.9	Stripes generated on the cornea using the set-up of fig. 6.8.	158
6.10	Vertical cross section of fig. 6.9. Subtraction of a fringe pattern and its corresponding video inverse (left) produces clean zero-crossings (right).	159
6.11	Histogram of the difference between the three-dimensional reconstruction of the cornea surface before and after 80 pulses ablation over an area of 1.25 mm ² at the apex of the cornea.	160
6.12	Central ablation depth versus the number of Excimer pulses incident on the cornea.	161
A.1	Principle of measuring the beam width with the moving-edge method.	164
A.2	Measurement of the transmitted power as a function of the edge position x' , and determination of the beam width w_e	165

List of Tables

4.1 Spectroscopic and hole burning parameters for naphthalocyanines doped polymers at 1.5 K.	99
---	----

Chapter 1 Introduction

”The cost for 128 kilobytes
of hard-disk memory will fall below US\$100
in the near future”

Creative Computing magazine, 1981

The information storage sector is a major subsystem of the immense computer industry. Today storage requirements are reaching hundreds of gigabytes (Gbyte = 10^9 bytes) to handle a wide range of desktop audio/video applications and tens of terabytes (Tbyte= 10^{12} bytes) to handle commercial servers and archival memory needs. Extreme pressure exists to reduce the cost of memory. Currently, the cost of memory for magnetic-based hard disks is 0.62 cents per megabyte (75 GB for \$468, IBMTM Deskstar 75 GXP, year 2000). In comparison, the cost of memory in 1981 was \$340 per megabyte (SeagateTM 5 MB, \$1700). For the past 20 years, the price per megabyte of memory has fallen at a constant yearly rate of 45% [1].

Optical data storage technology shares common attributes with the ubiquitous magnetic hard disk. Both technologies rely on mechanical rotation of the medium and assembly head. Thus, optical storage drives such as CD, DVD and magneto-optic disc drives benefited from the motorized technology developed for hard disks. Each bit of data is recorded on a localized area of the medium’s surface. Access time and transfer rates are limited by the speed of disk rotation (latency) and the linear translation of the head assembly (seek). A fundamental difference exists between hard disks and commercial optical data storage devices. The read-head assembly of hard disks is flying at nanometers distances above the medium while an optical read-head assembly lies millimeters away from the medium. This allows optical media to be transferable/portable. To obtain significant improvements in access time and data transfer rates, a different approach to the traditional sequential bit recording/reading

process needs to be developed. Optical technologies based on holography present an attractive solution because of the inherent parallelism of recording and reading data. Although a lot of research has been devoted to holographic-based storage, it has never achieved the business impact that was expected. The recent development of new recording materials, spatial light modulators, semi-conductor lasers and array detectors has triggered a renewed interest in holographic technology [2].

In the core of this thesis (chapters 2, 3 and 4), I will address the use of holography for data storage and optical processing. The novelty of this work arises from the development of new holographic materials.

In chapter 2, I present a recording technique called *holographic localized recording* that allows holograms to be recorded in a defined *localized* area in the volume of the novel material. I analyze the inter-play between recording time and diffraction efficiency, and compare them to conventional holographic memories. The holographic memory based on the localized recording method is characterized by measuring the signal-to-noise ratio of random bit images for a memory size of up to 100 holograms. An architecture is presented which enables the storage of more than 1000 localized holograms. The major advantages of this memory in comparison to conventional holographic memories are that no exposure schedule is necessary, and that any hologram can be selectively erased and rewritten without significantly affecting the other stored holograms. In conventional holographic memories, the diffraction efficiency is inversely proportional to the square of the number of stored holograms. Using localized holographic recording, the diffraction efficiency falls proportionally to $1/M$ rather than $1/M^2$, where M is the number of holograms. In addition to holographic memories, localized recording is applicable to temporal signal processing. I show that temporal filtering of femtosecond pulses can yield large time-bandwidth values using localized recording.

In chapter 3, I introduce a new technique called folded shift multiplexing that is an extension of shift multiplexing where light propagates into waveguides. The first part of chapter 3 reviews the theory of diffraction from volume gratings which leads to shift multiplexing. Although the first part of chapter 3 is not my work, it

is included here to understand the principles behind folded shift multiplexing. The major advantage of this method is that it enables the construction of flat memory modules, the size of silicon flash cards.

In chapter 4, I present a series of new frequency selective polymer materials in the near infrared region (800 nm). I benefited from the suggestions of Prof. A. Gorokhovskiy at CUNY and from Iouri Solomatine at Caltech who produced these polymers. My contribution is to demonstrate that holograms can be recorded and retrieved in these materials using absorption gratings at very low temperatures. Spectral Hole Burning (SHB) in these material yields GHz optical frequency selectivity at cryogenic temperatures and Terahertz inhomogeneous bandwidth. The optical frequency adds a further dimension that increases conventional holographic memory capacity. We show that capacity is further increased by using angle multiplexing of absorption holograms in these materials. The large inhomogeneous bandwidth (> 10 THz) of these polymer materials allows spatio-temporal optical processing and storage of femtosecond pulses. Optical processing of pulses requires that digital logic operations be performed. Electronic detectors have response times on the order of $\simeq 100$ ps, too slow to process femto and picosecond pulses. An all-optical method is needed to build the logic. I show an implementation of ultra-fast optical gates that is compatible with the spectral hole memory developed in this chapter.

In the subsequent chapters 5 and 6, I investigate two types of optical contactless three-dimensional sensors. This work was motivated by a collaboration with Prof. P. McDonnell, a pioneer in laser vision correction at the Doheny Eye Institute at the University of Southern California. Two types of sensors were developed to accurately measure the topography of the human eye during the time of the laser correction procedure. The first sensor is based on conoscopic patterns. These patterns are created by the interference of the two eigen-modes propagating in a bi-refringent crystal. Conoscopic patterns contain information about the three-dimensional wavefront. My contribution to this work is shared with Prof. G. Barbastathis. We theoretically and experimentally demonstrate the lateral and depth resolution of the sensor and its limi-

tations. This project was awarded a SBIR grant (Small Business Innovative Research) from the National Eye Institute. The second sensor utilizes structured lighting and triangulation and is based on the work of Prof. P. Perona and J. Y. Bouguet at the Caltech Vision laboratory. Although many sensors based on structured lighting have been proposed and demonstrated, ours was the first implemented for monitoring *in vivo* the shape of the human cornea under laser vision surgery.

Chapter 2 Holographic recording of localized holograms

In this section, I expand upon the differences between conventional optical storage and holographic storage and motivate the use of localized holograms. These elements will help to realize the concept of a hybrid memory device based on the advantages of holography and localized sequential bit recording. The construction of this hybrid memory is enabled by the recent discovery of a new recording material.

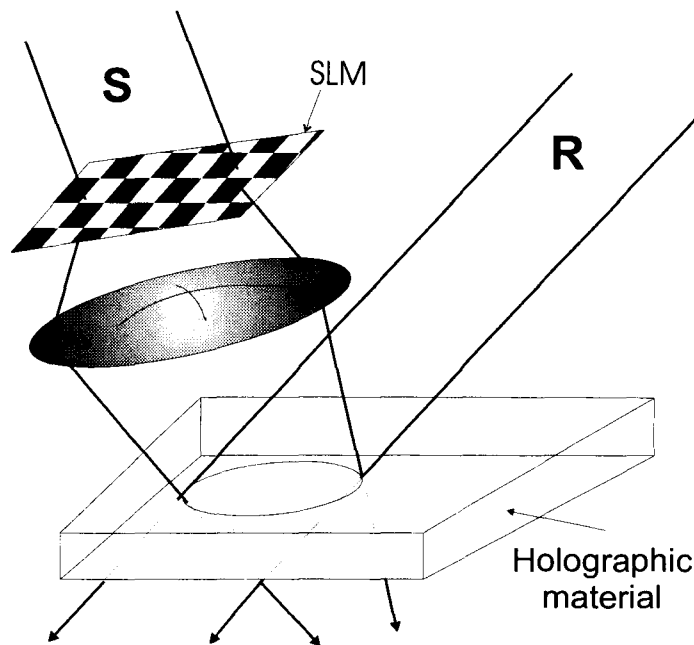


Figure 2.1: Basic holographic recording system. SLM: Spatial Light Modulator. R: reference beam. S: Signal beam.

In conventional optical recording, a data bit is stored by *locally* changing the physical or chemical property of the medium. In magneto-optical (M-O) media, the magnetic properties are changed with light, while for recordable CDs (CD-R), light changes the reflectivity of an organic dye (cyanine, phthalocyanine dyes). In contrast, holographic recording distributes an individual bit *throughout the volume*

of the recording medium. Information is recorded using two coherent beams (instead of one light beam for CD-R and M-O drives) which interfere inside the medium. One of the beams is the signal beam which is composed of multiple bits forming a page. Bits are imprinted by passing a light beam through a spatial light Modulator (SLM). Binary SLMs code a digital (0) as a dark spot on the image and a digital (1) as a bright spot. The second beam is the reference beam (fig. 2.1). The two beams produce a three-dimensional interference pattern of high and low intensities which is imprinted in the material by changing the physical or chemical properties of the medium. When the perturbation of the medium is illuminated by the reference beam, the light is diffracted and recreates the signal beam containing the data. An array detector can be placed to capture the diffracted light and hence can detect electronically the data bits [3, 4].

Multiple pages can be stored in the same volume by changing, for example, the angle of the reference beam [5] for each subsequent data page. In two-dimensional optical data storage systems, the storage capacity is proportional to X^2/λ^2 , where X is the physical size of the recording medium in each of the two dimensions and λ is the wavelength of light. In holographic memories, the three-dimensional interference pattern utilizes the depth of the medium, increasing de-facto the areal storage density. The storage capacity is proportional X^3/λ^3 , where the extra factor L/λ is equal to the number of pages recorded which can be on the order of 10^3 [24, 26].

The delocalization of bits of information in holographic storage unfortunately has the disadvantage of producing non-selective erasure: the erasure of a particular bit of information cannot be performed without affecting the other bits distributed throughout the volume. For multiple read-write memories, this represents a major drawback.

The work presented in this chapter shows that by combining the parallelism of holography and conventional two-dimensional localized single-bit-oriented optical storage, a practical memory device can be implemented. The resulting optical memory features multiple read-write capability and selective erasure with a transfer rate similar to that of conventional holographic memories (several GB/s) and a storage

density equal to that of two-dimensional optical memories (1-2 bit/ μm^2).

The recording medium selected for the realization of the memory is lithium niobate. Iron-doped lithium niobate ($\text{LiNbO}_3\text{:Fe}$) is a photorefractive recording material that has been studied extensively. Many optical systems involving iron-doped lithium niobate have been developed for large scale storage applications [6, 7, 8, 9, 10, 11]. This material has excellent optical properties, stability and the ease of growing large homogeneous bouls (4 inches in diameter) at a low cost (a few US dollars for 1 cm^3). However, volatility, which is the decay of the stored information in the material upon optical readout, is a major limitation for practical use of iron-doped lithium niobate (the same phenomenon applies to all other known photorefractive materials). Volatility arises because the read-out light has the same optical frequency as the light used to record the information, yielding an almost symmetric behavior between the writing and reading process. Recently, researchers have shown that upon addition of a second dopant, *manganese*, to LiNbO_3 , the properties of the resulting material called doubly doped $\text{LiNbO}_3\text{:Fe:Mn}$ change dramatically [12, 13, 14, 15, 16]. One of the benefits of the added dopant is that the information becomes persistent upon optical read-out.

A second benefit is the gating effect: the medium becomes recordable only when illuminated with violet light (365-420nm). In regions not illuminated with violet light, recording is not efficient. This effect allows **localized** sensitizing (gating): by focusing a coherent violet beam with a spherical lens, a tube-like region is sensitized inside the crystal. Similarly, violet light focused by a cylindrical lens produces a thin sensitized sheet. In this chapter, I will address the effect of localization on the holographic recording performances.

2.1 Recording in $\text{LiNbO}_3\text{:Fe:Mn}$ crystals

In this section, we review the optical properties of doubly-doped LiNbO_3 . In LiNbO_3 , the energy level of the iron centers is located in the gap between the valence band and conduction band. Iron exists in two different valence states: Fe^{2+} and Fe^{3+} . Light excites electrons from Fe^{2+} into the conduction band (CB) as illustrated

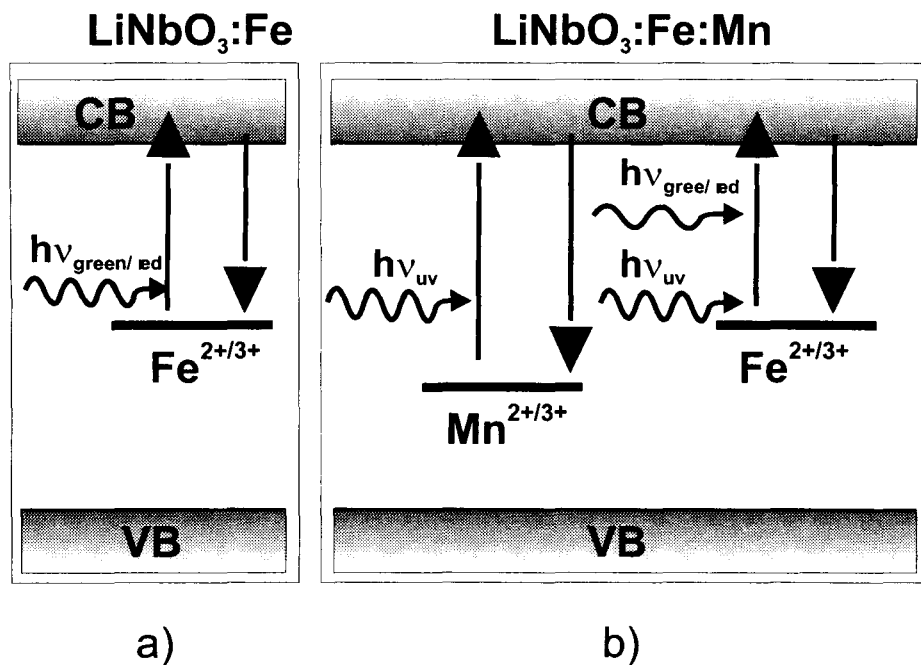


Figure 2.2: Band diagram of LiNbO_3 doped with iron (left) and doubly doped with iron and manganese (right). CB: conduction band; VB: valence band. Both elements occur in two valence states. Electrons are excited from Fe^{2+} by visible light and ultra violet light and from Mn^{2+} by ultra violet-light only. Free electrons in the CB can recombine with Fe^{3+} or Mn^{3+} .

in Figure 2.2 a). A spatially sinusoidal light pattern excites electrons proportionally to the light intensity; therefore, the distribution of the electrons in the conduction band is a replica of the light pattern. Electrons migrate in the conduction band due to the bulk photovoltaic effect, drift, and diffusion and get trapped by the Fe^{3+} centers elsewhere. The mobility of electrons in LiNbO_3 and the large recombination coefficient create a migration on the order of 1 nm each time an electron is photoexcited. This distance is much smaller than a period of the light pattern. The process comes to a steady state when the sum of all the forces involved in the migration of the electrons cancel each other. The equations describing the photorefractive band transport are described by the Kukhtarev equations [17, 18, 19]. Illumination of the grating, stored in the Fe centers, with homogenous light of the same wavelength, reveals the hologram and at the same time causes a uniform electron excitation. As a result, the charged pattern is redistributed homogeneously and the hologram is eventually

completely washed away after sufficient read-out time.

Several approaches have been proposed to enhance the persistence of the charge pattern. One approach is to change the read-out wavelength. The absorption cross section of LiNbO_3 away from the center peak at 477 nm, in the longer wavelength region, is much weaker and therefore the erasure is considerably reduced [20, 21, 22, 23, 24]. The problem with that approach is that the Bragg matching condition complicates the read-out especially when multiple hologram of images with high spatial frequencies are recorded. Another approach is to copy the space charge pattern onto a pattern of immobile ions, a process called thermal fixing [25, 26, 27, 28]. The recording occurs at high temperature (180° Celsius) and the ions become mobile and tend to compensate for the field generated by the electronic pattern. The grating imprinted in the ions is a perfect replica of the electronic grating. When the crystal cools down, the ions become immobile and the grating becomes fixed and insensitive to the read-out. However, for multiple image recording, the process becomes complicated and the high temperature requirement is not practical. Similarly, the electronic pattern can be copied onto ferro-electric domains by applying an external electric field ("electrical fixing") [29, 30, 31, 32, 33].

An all-optical method that yields non-volatile storage uses two-step recording [34, 35]: the simultaneous presence of a recording light of low photon energy and a gating light of high photon energy excites electrons via virtual or real intermediate levels to the conduction band. Upon read-out, the gating light is turned off and the low energy read-out light cannot by itself generate free electrons which makes the grating stable upon read-out. However, this approach has low sensitivity which is the major drawback.

The method using two dopants in LiNbO_3 is similar to two-step recording in that it requires the simultaneous presence of a recording light of one wavelength and gating or sensitizing light of a lower wavelength to generate a stable grating upon read-out. There is a fundamental difference in the recording properties between the two methods. For two-step recording only intensity matters; the gating light intensity required is approximately 1 W/cm^2 . For two-center recording only the intensity ratio

between recording and gating matters [15]. The sensitivity of the two-center method is several orders of magnitude higher than the two-step method. Thus, two center recording is more attractive than the two-step method for applications. The band diagram for $\text{LiNbO}_3:\text{Fe}:\text{Mn}$ is shown in fig. 2.2 (b). Manganese centers are located deeper in the band gap than the iron centers. The oxidation state of the crystal is such that, initially, the manganese centers are partially filled with electrons and that the iron centers are completely empty, i.e., only Fe^{3+} is present. The crystal is transparent for wavelengths of light equal to or greater than the $\text{Fe}^{2+}/3+$ transition level (477 nm). As a result, no charges are available to record a grating. When the crystal is illuminated with light at a shorter wavelength, the deep manganese traps are ionized. Electrons are sent to the conduction band and then recombine with either the Mn^{3+} or Fe^{3+} centers, thus populating a portion of the iron centers with electrons. The crystal becomes absorptive for a range of visible wavelengths. The central idea is to sensitize the crystal with short wavelength light (typically 400 nm), while recording with longer wavelength illumination (typically 532 nm, 632 nm). The sensitizing light yields a continuous supply of electrons to the iron centers from which the recording light generates an electronic pattern in the conduction band. In fig. 2.3, the light intensities (I) and concentrations of electrons in the traps (N) are plotted against the spatial coordinates x . Initially (Fig.2.3 (a)), the crystal is pre-sensitized with short wavelength light, which we call UV light in the remainder of this thesis (although we will use 400 nm which is not quite UV). The visible light is turned off during this process. This pre-sensitization step populates the iron level with electrons. During recording (Fig.2.3 (b)), the UV light is turned on and the visible recording interference pattern excites electrons from the Fe^{2+} centers. The free electrons move in the CB due to the bulk photovoltaic effect and are trapped elsewhere by Fe^{3+} and Mn^{3+} . The concentration of electrons in the iron centers (Fe^{2+}) creates a pattern that is close to 180° out of phase with the light intensity pattern. This phase shift occurs because the electrons are generated in the bright regions of the interference pattern and trapped in the dark regions. The phase difference is not exactly 180° out of phase because the photoexcited electrons from the iron centers travel a small

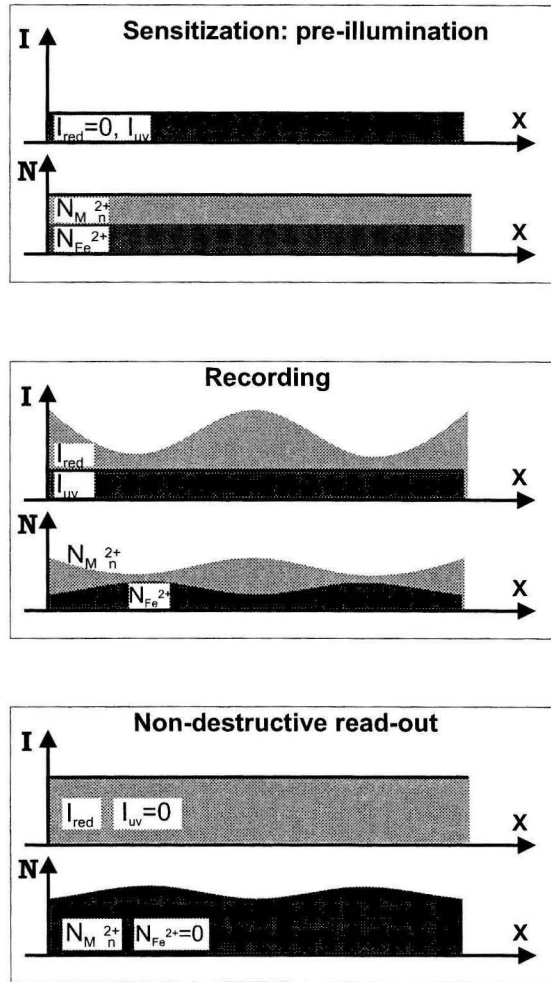


Figure 2.3: Recording and non-destructive read-out processes. The plot represent light intensities I for visible and ultra violet light and the concentration of electrons N trapped in the iron (Fe^{2+}) and manganese (Fe^{2+}) centers against the spatial dimension x directed along the grating vector.

distance before getting trapped. A grating is recorded similarly in the manganese centers by trapping part of the electrons excited from the iron level. The electron concentration in Mn^{2+} hence follows the recording light intensity pattern; therefore, the distribution of electron in manganese is approximately 180° out of phase with the electron concentration in iron. The extra transfer of electrons from Fe^{2+} to Mn^{3+} is due to the visible light: in bright regions of the interference pattern, some electrons are excited from the Fe centers and transferred back to the Mn centers via the conduction band. In dark regions, the transfer is much weaker due to the small

visible intensity. Therefore, the modulated Mn^{2+} grating is synchronized with the visible light intensity pattern. After recording, the UV light is switched off. The uniform visible reading light uniformly excites the electrons from the iron centers until all of them are trapped in manganese. During this process part of the space charge field decreases because the electron pattern stored in the iron centers is erased and the electrons in the conduction band tend to compensate any space charge field. However, after removal of all the electrons from Fe^{2+} by the visible reading light, the remaining portion of the space-charge grating that is stored in the manganese level persists against further read-out illumination. It is still possible to erase the hologram in manganese by exposing the grating to UV light.

2.2 Recording speed of localized holograms

We will use the property of gating in doubly doped Fe, Mn crystals to record localized holograms and study their holographic recording speed. In holographic data storage [36], pages of information are overlapped in the volume of the recording medium. Coherent erasure of a particular page also erases all the other pages stored in the same volume, due to the destructive read-out of holograms in photorefractive crystals such as $\text{LiNbO}_3:\text{Fe}$ [38]. In paragraph 2.1, we have reviewed the principles leading to non-destructive read-out in doubly-doped LiNbO_3 [12]. When holograms are multiplexed in such crystals [37], the erasure of a single page of information requires the sensitizing UV light to be present, causing the erasure of all the other pages of information stored in the same volume. One of the properties of localized holograms is that erasure is selective. The information stored elsewhere in the volume of the crystal is unaffected. As described in the last section, thin holograms can be recorded inside the volume by localizing the sensitizing beam. The approach described in this chapter for the recording of localized holograms is illustrated in Fig. 2.4.

The sensitizing beam is focused by a cylindrical lens, defining a thin disk with thickness of a few tens of micrometers in the crystal (within the depth of focus of the lens). The reference recording beam is co-propagating with the sensitizing beam and

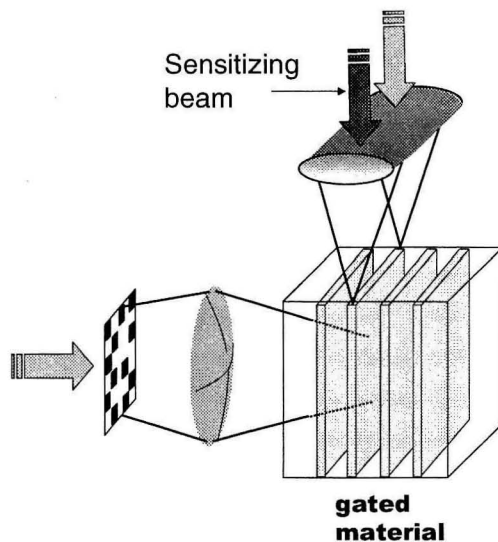


Figure 2.4: Localized recording in doubly doped LiNbO_3 .

focused by the same cylindrical lens. The signal beam interferes with the reference beam in a 90 degree geometry. Each page (hologram) takes up a slice of the volume. Multiple pages are recorded by physically moving the crystal (or the reference, sensitizing beam). This implementation of localized holograms can be considered the holographic analog of the three-dimensional optical two-photon memories architecture [41],[42]. In a two-photon memory architecture, a spot (bit) is written in the volume of a molded organic polymer only in locations where two beams with sufficient photon energies, one carrying the information and the other specifying the location, intersect temporally and spatially. The recorded bits are then read by fluorescence when excited by single photons absorbed within the written spot volume. The bits are arranged by page. Each page can be as thin as $30\mu\text{m}$.

In contrast, the localized method relies on holography to record the information. The localized recording method and architectures described in this chapter can be applied to any other gated material that produces non-volatile read-out [34]-[40].

The localized recording method implemented in this section follows the idea of fig. 2.4 described in section 2.2. We experimentally demonstrate the recording of 50 localized holograms in doubly-doped LiNbO_3 . We show that the time required to record a memory composed of M pages (holograms) is comparable to the total recording time of the conventional distributed volume recording method.

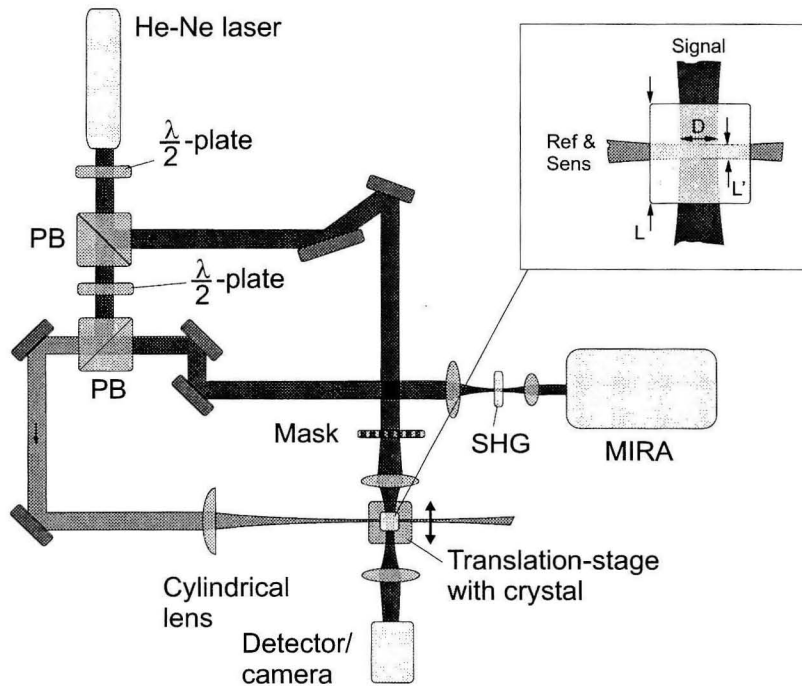


Figure 2.5: Recording set-up for the 50 holograms experiment. The camera CCD and detector are interchangeable.

We performed experiments with a congruent 90 degree-cut LiNbO_3 crystal doped with 0.075 wt. % Fe_2O_3 and 0.015 wt. % MnO . Figure 2.5 illustrates the experimental set-up. We used a frequency doubled femtosecond laser as a sensitizing light source (wavelength 405 nm), and a 15 mW HeNe laser for generation of the coherent red light (wavelength 633 nm, ordinary polarization). We recorded a plane wave hologram using two red beams interfering in a 90 degree geometry crystal illuminated by the sensitizing light. When read-out only with the red reference beam, the hologram is erased with a time constant which is only three times the writing time constant. The persistence of the hologram reported in [12] with continuous light (cw) sensitizing is

on the order of 10^4 . This effect cannot be explained by the repetition rate of the femtosecond laser (76 MHz). Because we use the light of the femtosecond laser for sensitizing, the high repetition rate can be considered as continuous for holographic recording. We used a continuous cw UV source as well and identical persistence were observed. This crystal was grown by a different manufacturer than the crystal used for the experiments in [12]. Although the concentration of iron and manganese are the same for the two crystals, it is unknown what process in the growing caused these differences in persistence. Nevertheless, this 90 degree crystal shows photochromism and sensitizing was necessary to record holograms.

An intensity transmission mask is imaged by a 4-f system onto a CCD camera. The reference beam is focused by an 8 cm cylindrical focal lens. The UV beam is co-propagating with the red reference beam. The lateral extension ($1/e^2$ value in intensity) of both focused beams inside the crystal is $40 \mu\text{m}$. The diameter of the focused beam is measured with the knife edge method (appendix A). The signal diameter is 1.5 mm inside the crystal (fresnel region). The $4 \times 4 \times 4 \text{ mm}^3$ crystal is mounted on a computer controlled translation stage. A photodetector measures the diffracted power with the signal and UV beams blocked. At each spatial location, the crystal is pre-sensitized with the focused UV beam for 10 sec. We used an exposure schedule for the recording of 50 holograms because of the non-persistence of holograms as explained above. Holograms are recorded with the red beams for 4.5 min on average (reference = $720 \mu\text{W}$, signal = $120 \mu\text{W}$, UV = $100 \mu\text{W}$). Multiple holograms are recorded by translating the crystal between exposures. A center to center separation of $80 \mu\text{m}$, which is equal to twice the lateral extension of the red and UV beam is used between spatial locations. The experimental result is shown in fig. 2.6(a). Each peak in the plot results from the diffraction efficiency of a localized hologram as the crystal is translated in the direction perpendicular to the reference beam. In fig. 2.6(b), hologram number 25 was selectively erased by continuous illumination of UV. The detector is then replaced by a camera and an example of a reconstructed image is shown in fig. 2.6(a). The imaging lens captured the totality of the diffracted light. We did not quantitatively measure the fidelity of the reconstruction. This

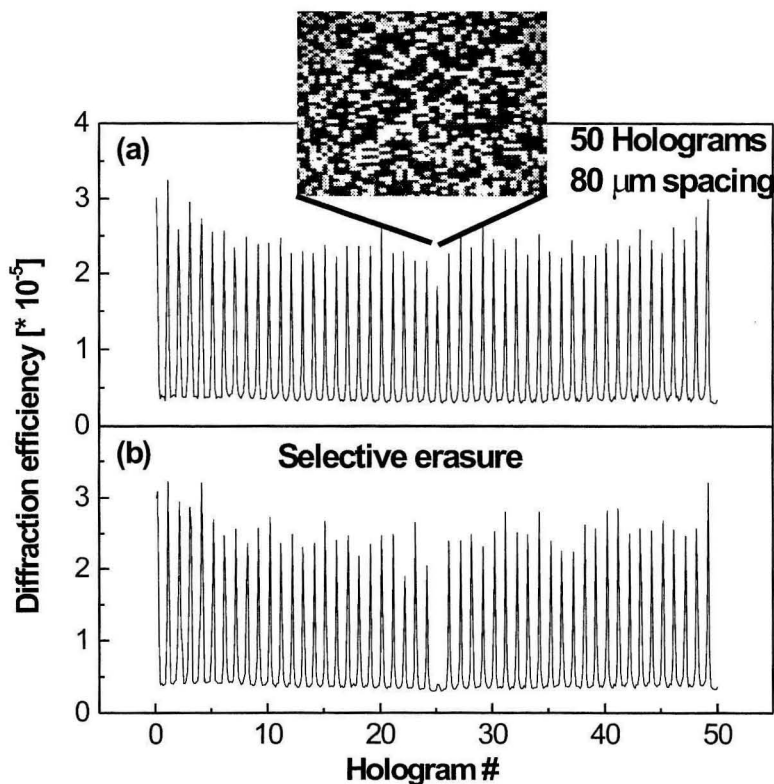


Figure 2.6: (a) 50 images recorded in a $\text{LiNbO}_3:\text{Fe,Mn}$ crystal. Each peak corresponds to the diffraction efficiency of a hologram stored at a different spatial location as the crystal is translated in the direction perpendicular to the reference beam. Center to center spacing between each hologram is $80\mu\text{m}$ (b) Hologram #25 is selectively erased by continuous illumination of UV and red reference.

experiment demonstrates that holograms can be recorded locally in $\text{LiNbO}_3:\text{Fe,Mn}$ crystal, enabling selective non-coherent erasure.

The following analysis compares the total recording time of M holograms using conventional distributed volume holographic recording in doubly-doped LiNbO_3 [37] and localized recording in the same crystal as described in this section. The analysis calculates the recording time required to achieve the same final diffraction efficiency for the two methods. The total power for recording is fixed and equal for both recording methods in order to make the comparison fair since the results derived in this section scale identically with total power for both methods. The power is divided equally between the reference and signal beams for distributed recording because it optimizes the recording speed. We keep the reference and signal power equal in the

case of localized recording for the same reason.

For distributed volume hologram recording, an exposure schedule is necessary to obtain equalized diffraction efficiency for M holograms. The square root of the final diffraction efficiency is equal to [43]:

$$\begin{aligned}
 \sqrt{\eta} &= C A_o \left(1 - e^{-\frac{t_M}{\tau_w}}\right) \\
 &\simeq C \frac{A_o}{\tau_w} t_M \\
 &= C \frac{M_{\#}}{\frac{\tau_e}{t_1} + M - 1},
 \end{aligned} \tag{2.1}$$

where M is the number of holograms, $M_{\#} = \frac{A_o \tau_e}{\tau_w}$ is the M -number parameter, A_o is the square root of the saturation diffraction efficiency after red-erasure, τ_w and τ_e are the writing and erasure time constants respectively, t_1 is the recording time of the initial hologram and $t_M = \frac{\tau_e}{\frac{\tau_e}{t_1} + M - 1}$ is the recording time of the last hologram. This relation differs from the usual equation by a factor C , which is the square root of the ratio between the signal and reference beam area in the crystal: $C = \sqrt{\frac{A_s}{A_r}}$. It is more appropriate to express the diffraction efficiency as a power ratio rather than an intensity ratio. The optical power is proportional to the number of photons per second incident on the sensitive area of the detector:

$$P = \frac{\text{number of photons } h\nu}{\text{second}}. \tag{2.2}$$

where $h\nu$ is the energy of one photon of frequency ν . In the holographic system of fig. 2.7 (a), the holograms are reconstructed with an extended reference beam. The reconstruction is imaged onto a camera of area A_{det} . In fig. 2.7 (b), holograms are reconstructed using a focused reference beam. Similarly to (a), the reconstruction is imaged onto a camera of area A_{det} . Because the detection area is the same for both system, the diffracted power can be compared between system (a) and (b). The incident power on the holographic system is equal to the laser power in both the localized and distributed system; therefore, the relevant diffraction efficiency is the ratio between diffracted power and input power. For conventional holographic

recording the reference and signal beam are usually the same size. In this case the diffraction efficiency expressed as an intensity or power ratio is identical.

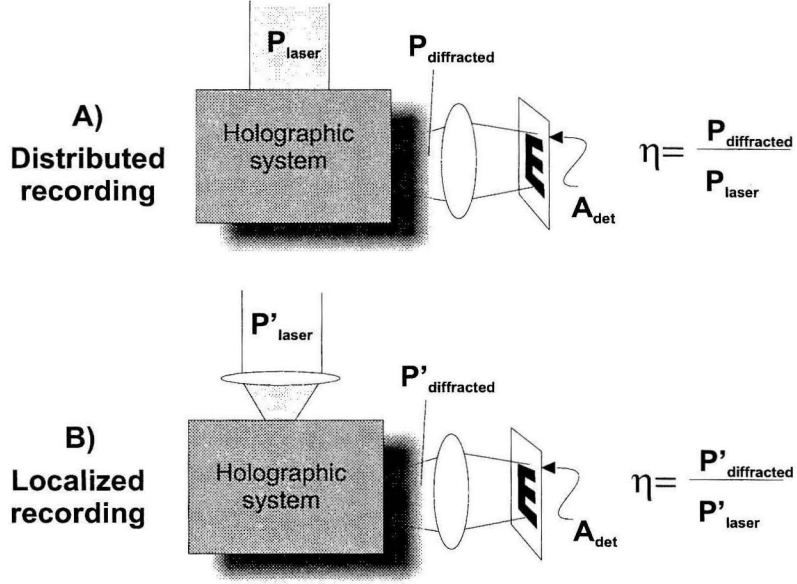


Figure 2.7: Localized and distributed recording system. The relevant diffraction efficiency is given by the power ratio: $\frac{\text{diffracted power}}{\text{input power}}$.

The total recording time for M distributed volume holograms is equal to:

$$T_{\text{tot}} = \tau_e \ln \left(1 + (M - 1) \frac{t_1}{\tau_e} \right). \quad (2.3)$$

For the localized method, the total recording time for M holograms is simply:

$$T'_{\text{tot}} = M t'_s, \quad (2.4)$$

where t'_s is the time to record one hologram. In the following relations, the primed variables correspond to the localized recording. The square root of the diffraction efficiency of one localized hologram recorded for time t'_s is equal to: $\sqrt{\eta'} \simeq C \sqrt{M} \frac{A'_o}{\tau'_w} t'_s$ with $t'_s \ll \tau'_w$. The extra factor \sqrt{M} comes from the fact that the area of the reference beam has been reduced by M ($\frac{L}{M} = L'$, see inset of fig. 4.17). Since A'_o is proportional to the modulation depth $m' = \frac{\sqrt{I'_r I_s}}{I'_r + I_s}$ and interaction length L' , and $\tau'_w \propto \frac{1}{I'_r + I_s}$ [18],

the recording slope S' for the localized recording is equal to:

$$\begin{aligned} S' &= C \sqrt{M} \frac{A'_o}{\tau'_w} = C \sqrt{M} \frac{A_o}{\tau_w} \frac{1}{M} \sqrt{\frac{I'_r I'_s}{I_r I_s}} \\ &= C \frac{A_o}{\tau_w} = S. \end{aligned} \quad (2.5)$$

Since $S = C \frac{A_o}{\tau_w}$ is the recording slope for the distributed volume recording, this relation shows that, as long as $t'_s \ll \tau'_w$, the ratio between the recording slopes is independent of L' . We experimentally verified this result by measuring the recording slope of the square root of the diffraction efficiency (computed as a power ratio) for different interaction lengths L' , keeping the power in the reference and signal beams constant. For two orders of magnitude difference in interaction length L (3.5 mm to 40 μm), we observed a drop of 20 percent in recording slope. We attribute this drop to the experimental errors due to the difficulty of overlapping UV and red reference beam in the crystal for small lateral extension. We will use the result of eq. 2.5 to compare the recording speed of the localized recording and the distributed volume recording. The final diffraction efficiency for the two cases are:

$$\begin{aligned} \sqrt{\eta'} &= C \frac{A_o}{\tau_w} t'_s \\ \sqrt{\eta} &= C \frac{A_o}{\tau_w} t_M. \end{aligned} \quad (2.6)$$

Equations 2.6 show that the total recording time of the localized hologram method is shorter than that of the distributed volume method, because t_M is the shortest recording time of the exposure schedule. This result, however, is valid only if holograms are recorded in the linear region of the recording curve. We have to be careful, because the localized recording time constant τ'_w becomes, using $\frac{\tau'_w}{\tau_w} = \frac{I_r + I_s}{I'_r + I'_s}$:

$$\tau'_w = \tau_w \frac{I_r + I_s}{M I_r + I_s} = \tau_w \frac{2}{M + 1} \simeq \frac{\tau_e}{M}, \quad (2.7)$$

where I_r and I_s are the reference and signal intensities respectively. We set $I_r = I_s$ in eqn. 2.7 because, for distributed volume recording, the recording beams have

similar area and equal power. Experimentally, τ_e is roughly equal to τ_w in doubly-doped LiNbO₃ as a result of constant sensitizing illumination in the crystal volume throughout the recording process of the M holograms [37]. This is different with localized recording since the sensitizing light is localized and does not erase previous holograms. Thus, from eqn. 2.7, the last recording time of the exposure schedule for the distributed volume recording ($\simeq \frac{\tau_e}{M}$) is of the same order of magnitude as the writing time constant of the localized holograms. Therefore, the holograms are being recorded in the non-linear region. The total recording time of the localized recording has to be computed using the exact form of the recording curve:

$$\sqrt{\eta'} = C \frac{A_o}{\tau_w} \tau_w' \left(1 - e^{-\frac{t'_s}{\tau_w}} \right) = C \frac{A_o}{\tau_w} t_M. \quad (2.8)$$

Substituting eqn. 2.7 in eqn. 2.8 and solving for t'_s , we can obtain the total recording time:

$$T'_{tot} = M t'_s = \frac{-2M}{M+1} \tau_w \ln \left(1 - \frac{\tau_e}{\tau_w} \frac{M+1}{2 \left(\frac{\tau_e}{t_1} + M - 1 \right)} \right).$$

The total recording time for the distributed volume method is given by eqn. 2.3. We note that the ratio of T'_{tot} and T_{tot} depends on the ratio of time constants $\frac{\tau_e}{\tau_w}$, the number of holograms M and the initial recording time t_1 of the exposure schedule. A practical value for t_1 is taken as $\frac{\tau_e}{20}$. The graph of fig. 2.8 plots the ratio of total recording time for both method T'_{tot} and T_{tot} against the number of holograms for two values of $\frac{\tau_e}{\tau_w}$. We see from this graph that, for $\frac{\tau_e}{\tau_w} = 1$, the total recording time of the localized method can be shorter than the total recording time of volume holograms for $M > 10$ holograms. As the ratio $\frac{\tau_e}{\tau_w}$ increases, this advantage of the localized recording method quickly vanishes. There exists a ratio $\frac{\tau_e}{\tau_w}$ above which the localized holograms cannot reach the diffraction efficiency obtained with distributed volume holograms independently of the exposure time allotted. For $M=1000$ and $t_1 = \frac{\tau_e}{20}$, this threshold ratio is equal to 2.1.

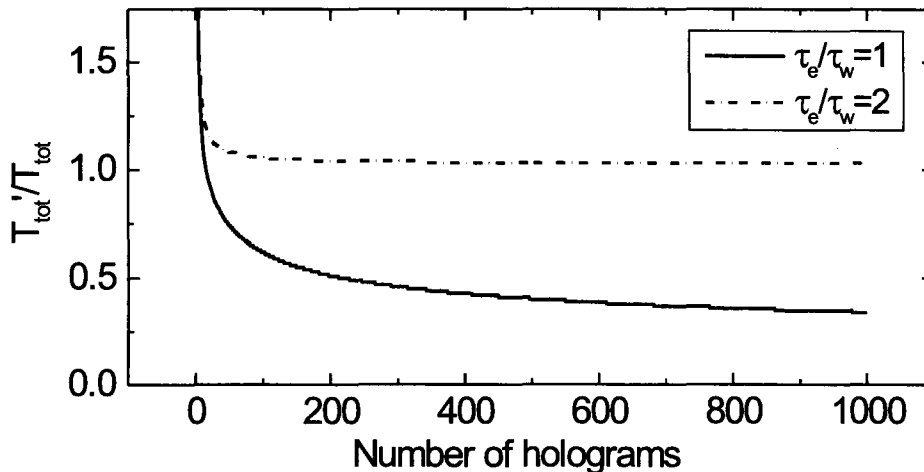


Figure 2.8: Ratio of total recording time between the localized and the distributed volume methods in function of the number of holograms to record for two different values of the ratio $\frac{\tau_e}{\tau_w}$ and $t_1 = \frac{\tau_e}{20}$.

Another basis to compare the two methods is in terms of storage density. We consider first the experiment described in this section. Fifty localized holograms with equal diffraction efficiency of $2 \cdot 10^{-5}$ were recorded. The effective $M_{\#}^{\text{loc}}$ of the localized method is equal to $M \sqrt{2 \cdot 10^{-5}} = 0.22$. If we use the same crystal for distributed volume recording (with $M=50$), we can compute the $M_{\#}$ using a single plane wave hologram recording in the same crystal. Assuming equal recording and erasing time constants (see discussion above), we found $M_{\#}^{\text{vol}} = 0.18$. This result suggests that 50 holograms for both methods can be recorded in the same volume with approximately the same diffraction efficiency. We need to know how this result scales with M . The maximum number of localized holograms that can be stored in a given crystal thickness is limited by the diffraction of the focused sensitizing and reference beam. Let a typical spot size for a high bandwidth signal beam recorded in the Fourier plane be $\simeq 3\text{mm}$. This translates to an optimal focusing of $15\mu\text{m}$ ($1/e^2$ value) for the sensitizing beam and thus a center to center spacing of $30\mu\text{m}$. Therefore, if we assume a crystal thickness of 1 cm, 330 localized holograms could be

recorded with a diffraction efficiency equal to $2 \cdot 10^{-5}$. In comparison, the diffraction efficiency of 330 holograms stored with the distributed volume method would be equal to $\eta = \left(\frac{M_{\#}^{vol}}{330}\right)^2 = 1.9 \cdot 10^{-6}$. The larger final diffraction for the localized recording comes at the expense of a longer recording time because in this case, each hologram would have to be recorded in the non-linear region. Of course, if we are willing to accept a lower diffraction efficiency for $M=330$, then this could also be obtained with localized recording at a shorter recording time as explained earlier.

2.3 Maximum diffraction efficiency of localized holograms

We reported in the previous section the recording of 50 localized holograms spatially multiplexed in a $\text{LiNbO}_3:\text{Fe,Mn}$ crystal using a 90 degree geometry [44]. In this section, we demonstrate the recording of strong localized holograms in $\text{LiNbO}_3:\text{Mn,Fe}$ that improves the $M_{\#}$ by a factor M , where M is the number of holograms.

The localized holograms are written with a focused reference beam and an extended signal beam with the same technique described in section 2.2. The recording geometry is illustrated in fig. 2.9. The main difference between this set-up and the previous set-up shown in fig. 2.5 is the half wave plate positioned before the polarizing beam-splitter. The purpose of the beam splitter is to distribute the laser power between the reference and signal beam. According to the relative power distribution between the reference and signal beam, the recording dynamics of the holograms varies: this is caused by the large difference in the area of the beams at the overlapping region. We will show that, under a particular power distribution, the final diffraction efficiency does not decrease proportionally to $1/M^2$ but to $1/M$ when recording is done in doubly doped LiNbO_3 . The significance of such a result is important for many applications if we consider that for 100 holograms, the diffraction efficiency of each of the 100 holograms can be a factor of 100 times larger than conventional recording in iron doped only LiNbO_3 . The holograms in the experiment of section 2.2

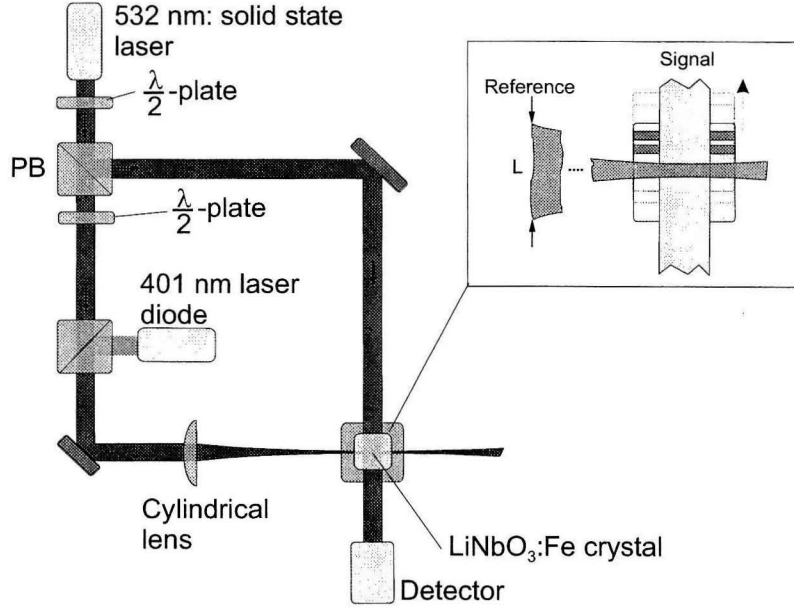


Figure 2.9: Recording set-up. The half wave plate positioned before the polarizing beam-splitter distributes the power between the reference and signal beam. The waveplate is mounted on a rotation stage for continuous power distribution.

were recorded so as to maximize recording speed and did not reach large diffraction efficiency.

The recording slope S in photorefractives is given by:

$$S = \frac{A_o}{\tau_w} \propto \sqrt{P_r P_s}. \quad (2.9)$$

where P_r and P_s are the power in the reference and signal beam respectively. Eq. 2.9 is subject to $P_r + P_s = P_{total} = \text{constant}$. Thus the recording slope is maximized for equalized power $P_r = P_s$. In this case the recording slope is optimized but the saturation diffraction efficiency is low because of the low resulting modulation depth. The saturation diffraction efficiency (A_o) is proportional to the modulation depth (m):

$$A_o \propto m = \frac{\sqrt{I_r I_s}}{I_r + I_s}. \quad (2.10)$$

This quantity is maximized for equal intensity $I_r = I_s$ independent of the total power.

The following experiment illustrates this dynamic. We used a 90 degree-cut LiNbO₃ crystal doped with 0.01 wt. % Fe₂O₃. We used a Coherent solid state laser, wavelength 532 nm, linearly polarized, for the recording beams. A cylindrical lens focuses the reference beam (6 mm diameter) in the crystal. The reference beam interferes with a plane wave signal beam (6 mm diameter) as shown in the set-up of fig. 4.17. The total power is distributed into the reference and signal beam using a half wave-plate and a polarizing beam splitter. In the first experiment, the reference and signal beam have equal power. In the second experiment, the intensity between

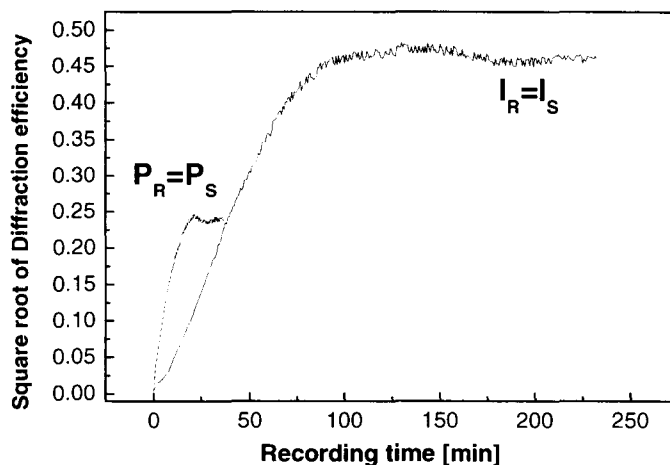


Figure 2.10: Recording curves of a localized hologram. The dashed curve is recorded with equal power. The plain curve is recorded with equal intensity in the reference and signal beam. The lateral extension of the reference beam is 50 times smaller than the signal diameter.

the reference and signal beam is equalized. The result is shown in fig. 2.10 for the case of a reference beam focused to a lateral extension equal to $120\mu m$ ($1/e^2$ value). As predicted, the curve recorded with equal power has a larger recording slope than the curve recorded with equal intensity and saturates at a much lower diffraction efficiency. We study the trade-off between recording time and saturation diffraction efficiency and applied the results in the case of recording a large number of holograms

in doubly doped LiNbO₃ [44, 37]. We start by letting α be the ratio of the power in the reference beam and the total power:

$$\alpha = \frac{P_r}{P_r + P_s}. \quad (2.11)$$

We take the area of the unfocused reference beam and signal beam as equal. The primed variables correspond to the recording with a focused reference. The square root of the diffraction efficiency computed as power ratio is given by [43]:

$$\sqrt{\eta'} = \sqrt{M} A'_o \left(1 - e^{-\frac{t}{\tau'_w}}\right). \quad (2.12)$$

where A'_o and τ'_w are the saturation diffraction efficiency and recording time constants of the localized recording respectively. M is the number of holograms which is equal to the ratio between the lateral extension of the unfocused reference to the focused reference ($\frac{L}{L'}$, see fig. 4.17). $A'_o = A_o \frac{m'L'}{mL}$, where A_o is the saturation diffraction efficiency for the unfocused reference beam recording ($m = \frac{1}{2}$). Using eq. 2.11, the saturation diffraction efficiency A'_o can be calculated according to:

$$A'_o = \frac{2 A_o}{\sqrt{M}} \frac{\sqrt{\alpha(1-\alpha)}}{1 + \alpha(M-1)}. \quad (2.13)$$

The writing time constant can be written as:

$$\tau'_w = \frac{\tau_w}{1 + \alpha(M-1)}. \quad (2.14)$$

Replacing eq. 2.13,2.14 in eq. 2.12, we obtain:

$$\sqrt{\eta'} = 2 A_o \frac{\sqrt{\alpha(1-\alpha)}}{1 + \alpha(M-1)} \left(1 - e^{-\frac{t}{\tau_w}(1+\alpha(M-1))}\right). \quad (2.15)$$

The parameter α varies from 0 to 1 corresponding to the total power being concentrated in the signal and reference beam respectively. Any value of α between 0 and 1 means that the total power is distributed between the reference and signal beam.

α takes the value $\frac{1}{2}$ for equal power in reference and signal beam. For equal intensities, $\alpha = \frac{1}{M+1}$. The ratio of the saturation diffraction efficiency in the cases of equal intensity and equal power recording is computed from eq. 2.15 and is given by:

$$\frac{\eta_{equal\ intensity}}{\eta_{equal\ power}} = \frac{(M+1)^2}{4M} \simeq \frac{M}{4}. \quad (2.16)$$

We have experimentally measured this ratio by recording holograms with equal

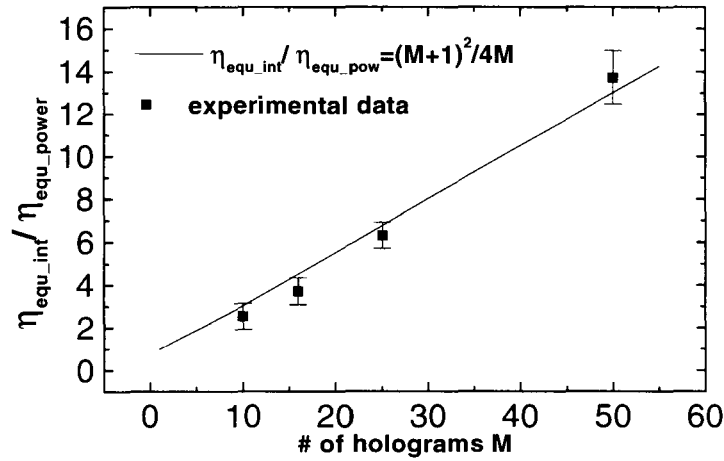


Figure 2.11: Ratio of saturation diffraction efficiency between localized holograms recorded with equal intensity and localized holograms recorded with equal power in function of the number of holograms $M = L/L'$.

power and equal intensities for four values of M (10,16,25,50). Fig. 2.11 shows the experimental ratio of the diffraction efficiency vs M, in good agreement with eq. 2.16. The diffraction efficiency of a single strong localized hologram is computed by plugging $\alpha = \frac{1}{M+1}$ in eq. 2.12 and 2.13 giving $\sqrt{\eta'} = \frac{A_o}{\sqrt{M}} \left(1 - e^{-\frac{2t}{\tau_w}}\right)$. Assuming a very long erasing time constant ($\gg M \tau_w$), the final diffraction efficiency after recording M strong holograms is given by $\eta' = \frac{A_o^2}{M}$. If we define an effective M number $M_{\#}^{eff} = A_o^2$, the result can be written as:

$$\eta' = \frac{M_{\#}^{eff}}{M}. \quad (2.17)$$

Note that $M_{\#}^{eff} \leq 1$.

As we will see, the recording time for each hologram is very long and the stability of the set-up becomes an issue. We empirically found a recording method that is repeatable and robust which we describe here. The power is progressively distributed from the reference beam into the signal beam during recording. The intent is to ensure that the recording slope is maximum during the recording process. To compute the optimal ratio of power during recording, we start from eqn. 2.15 and make the partial derivative with respect to α equal to 0. At each time increment, we have an equation in α to solve. The resulting equation is solved numerically for each time increment. This procedure converges well at each time step t_n if the initial guess for α is taken as the previous value found for α at time step t_{n-1} . The initial value for α is $\frac{1}{2}$ at $t=0$. For $M=50$, the optimal power routing, described by the parameter α vs time, is shown in fig. 2.12. The power in the reference beam is quickly depleted to the signal beam. The resulting value of $\alpha(t)$ is used to record a localized hologram. The experimental recording curve using this power routing is shown in fig. 2.13. A smooth recording curve is achieved with this method. In the following experiments,

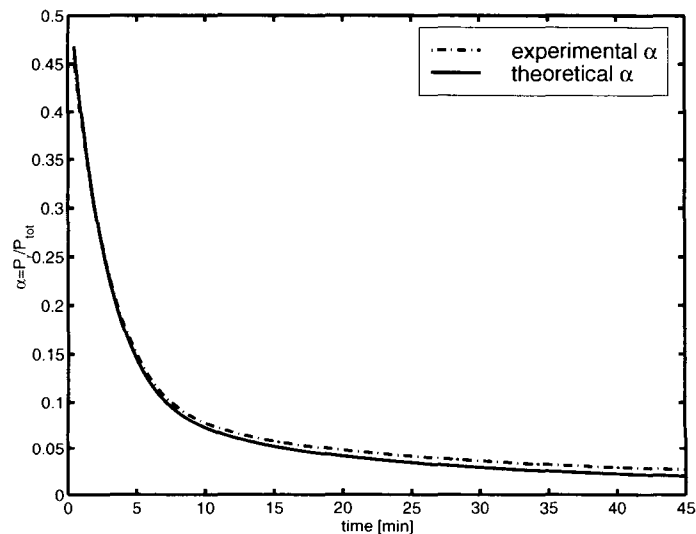


Figure 2.12: Power distribution during recording between reference and signal beam represented by the parameter $\alpha = P_r / (P_r + P_s)$.

the holograms are recorded using the method of continuous power routing. We now

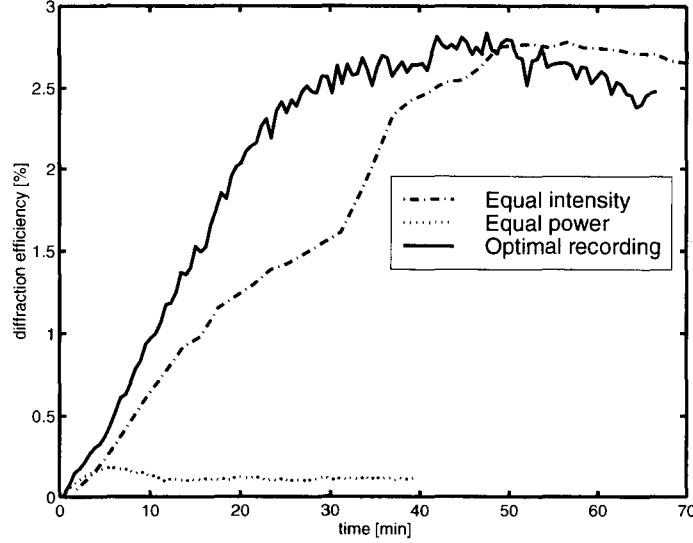


Figure 2.13: Recording with continuous power distribution between reference and signal beam (solid curve) for a number of holograms M equal to 50. The dashed curves for equal power and equal intensity recording are shown for comparison.

apply those results to the case of localized holographic recording in doubly doped LiNbO_3 . The advantage of this material compared to iron doped LiNbO_3 is that localized holograms are not erased during the recording of subsequent holograms. We showed theoretically and experimentally in section 2.2 ([44]) that M localized holograms recorded in doubly doped LiNbO_3 using equal power in the reference and signal beam yield a final diffraction efficiency equal to that obtained using distributed volume recording and with approximately the same total recording time. We have the choice of increasing the final diffraction efficiency of localized holograms by a factor of $\frac{M}{4}$ (eqn. 2.11) when intensities are equalized yielding a final diffraction efficiency that varies as $1/M$ instead of $1/M^2$. The total recording time can be estimated assuming that each hologram is recorded for one time constant τ'_w :

$$T'_{\text{localized total}} = M \tau'_w = M \frac{\tau_w}{2} \simeq M \tau_e. \quad (2.18)$$

where we assume that the erasing time constant τ_e of the distributed volume recording is roughly equal to the writing time constant τ_w . We used eqn. 2.14 to compute τ'_w . Since the total recording time of the distributed volume method is equal to $\tau_e \ln(M)$,

the total recording time for the localized holograms is increased by a factor $\simeq \frac{M}{\ln(M)}$.

2.3.1 Effect of finite recording time

We have theoretically shown that when each localized hologram is recorded to saturation with equalized recording intensities, we can achieve a final diffraction efficiency, for the M spatially stored holograms, that varies as $\frac{1}{M}$. In deriving this result, we have assumed that the erasing time constant is infinite. To be more accurate, we have to take into account the finite erasing time constant of doubly doped LiNbO_3 . Referring to the recording geometry illustrated in sections 2.2 and 2.3, the recorded holograms are erased only by the signal beam. An important parameter, which determines the final diffraction efficiency, is the ratio between the erasing time constant τ_{e_2} of the grating stored in Mn and the writing time constant τ'_w : this means a high recording speed (large sensitivity S) and a slow erasure (large erasing time constant τ_{e_2}). It turns out that these two parameters cannot be maximized independently. The absorption coefficient of the crystal in the red (633nm, He-Ne laser) is much less than in the blue (488nm, Argon). The Argon line at 488nm is more effective for the recording from Fe traps. However, blue light has higher energy per photon than red light, which increases the probability of sending electrons from the Mg traps to the conduction band, thus erasing the hologram. An optimal choice for these two parameters can be found by selecting the appropriate recording wavelength. We compare the recording for red light at 633nm, easily obtainable from He-Ne lasers or red laser diodes, and for green light at 514nm from An Argon laser. The sensitivity S is defined by:

$$S = \beta \frac{d\sqrt{\eta}}{dt} \Big|_{t=0} = \beta \frac{A_o}{I_R L \tau_w}. \quad (2.19)$$

where I_R is the total recording intensity, L the crystal thickness, A_o the saturation diffraction efficiency and β is the ratio of $\sqrt{\eta}$ after sufficient read-out to $\sqrt{\eta}$ at the end of recording (before read-out). In the green (514 nm), S is 20 times larger than the sensitivity in the red (633 nm) [15]. Using eqn. 2.19 and the following measured

values for ordinary polarization:

$$A_o^{514} = 0.44, A_o^{632} = 0.30. \quad (2.20)$$

We obtain a ratio of the writing time constant at 633nm and 514nm equal to (assuming equal recording intensity in the red and green):

$$\frac{\tau_w^{633}}{\tau_w^{514}} = 13.6. \quad (2.21)$$

The ratio of erasing time constant between red and green light for equal erasing intensities were measured in ref. [15]:

$$\frac{\tau_e^{632}}{\tau_e^{514}} = 294. \quad (2.22)$$

The writing and erasing time constant at 514nm are equal to:

$$\begin{aligned} \tau_w^{514} &= 3 \cdot 10^3 \text{ s } (34mW/cm^2) \\ \tau_e^{514} &= 2 \cdot 10^5 \text{ s } (17mW/cm^2). \end{aligned} \quad (2.23)$$

We obtain from eqn. 2.21, 2.22 and 2.23 the following erasing-writing asymmetry ratios (considering that the erasing intensity is half the recording intensity):

$$\left(\frac{\tau_e}{\tau_w} \right)_{633} = 1441, \left(\frac{\tau_e}{\tau_w} \right)_{514} = 67. \quad (2.24)$$

Red light offers a larger recording-erasing asymmetry than green light. This advantage is counterbalanced by a lower saturation diffraction efficiency A_o for red light compared to green light. To analyze this compromise, we derive a recording exposure schedule. The equalized final diffraction efficiency after the recording schedule is compared to the saturation value of a single hologram as a function of the asymmetry ratio $\frac{\tau_e}{\tau_w}$.

We start with the expression of the recording strength over time of localized

holograms recorded with equal intensity in the reference and signal beam:

$$\sqrt{\eta} = \frac{A_o}{\sqrt{M}} \left(1 - e^{-\frac{t}{\tau_w}}\right). \quad (2.25)$$

The m^{th} hologram has recording strength:

$$\sqrt{\eta_m} = \frac{A_o}{\sqrt{M}} \left(1 - e^{-\frac{t_m}{\tau_w}}\right) e^{-\sum_{m'=m+1}^M \frac{t'_{m'}}{\tau'_{e2}}}. \quad (2.26)$$

where τ'_{e2} and τ'_w are the erasing and recording time constants.

In order to equalize the strength of the hologram, we require that $\sqrt{\eta_{m+1}} = \sqrt{\eta_m}$. With eqn. 2.26, this last expression is equal to:

$$\left(1 - e^{-\frac{t_m}{\tau_w}}\right) e^{-\frac{t_{m+1}}{\tau'_{e2}}} = \left(1 - e^{-\frac{t_{m+1}}{\tau_w}}\right). \quad (2.27)$$

Since the recording time t_m of any hologram is smaller than the erasing time constant τ'_{e2} , we can rewrite eqn. 2.27 as:

$$\left(1 - e^{-\frac{t_m}{\tau_w}}\right) \left(1 - \frac{t_{m+1}}{\tau'_{e2}}\right) = \left(1 - e^{-\frac{t_{m+1}}{\tau_w}}\right). \quad (2.28)$$

The exposure schedule (t_m , $m=1\dots M$) is computed by solving numerically eqn. 2.28 given an initial recording time t_1 . The final diffraction efficiency is then computed for various asymmetry ratios $\frac{\tau'_w}{\tau'_{e2}}$. In the simulation represented in figure 2.14, the first hologram is recorded with a time equal to two writing time constants. The plot shows the final diffraction efficiency after the exposure schedule versus the asymmetry ratio $\frac{\tau'_w}{\tau'_{e2}}$. Two sets of curves are shown corresponding to a number of recorded holograms equal to 50 and 1000. The asymmetry ratio for wavelengths 632.8 nm and 514 nm is equal to 1441 and 67 respectively. We see from this plot that recording with red light achieves a better final diffraction efficiency due to a larger asymmetry ratio than green light. Using red recording with a number of holograms equal to 1000, the diffraction efficiency after the exposure schedule is equal to 0.6% compared to 0.08% for green recording. When the number of holograms is lower ($M=50$), the diffraction efficiency

after the exposure schedule is equal to 1.9% using red recording compared to 1.4% for green recording. The difference between red and green recording becomes important for large number of holograms. The exposure schedule for 1000 holograms is illustrated in fig. 2.15. For applications such as diffractive optical elements and ROM

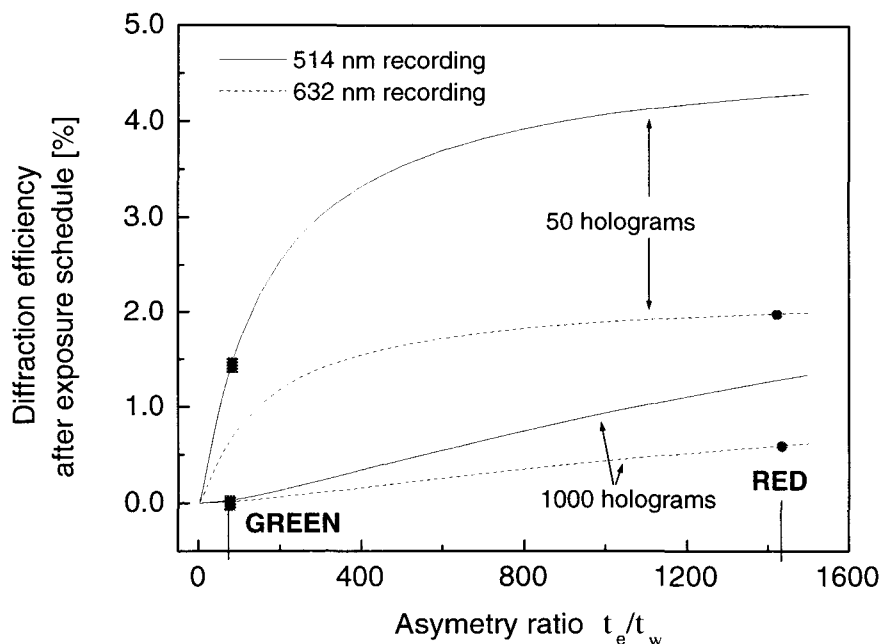


Figure 2.14: Diffraction efficiency η in doubly doped $\text{LiNbO}_3:\text{Fe,Mn}$ as a function of the ratio τ_e/τ_w . The two sets of curves correspond to a number of recorded holograms equal to 50 and 1000.

(Read Only Memory) memories which require high diffraction efficiency and multiple read-out, red recording is preferred. For a multiple read-write memory application, green recording is preferred because of a larger recording speed than red.

We experimentally recorded 50 localized holograms with equal writing intensity in the reference and signal beam using the geometry illustrated in fig. 2.16. This experiment differs from the 50 localized hologram experiments in section 2.2. Here the diffraction efficiency is maximized with equal intensity between the recording beams whereas in the previous experiment equal power was used to maximize recording

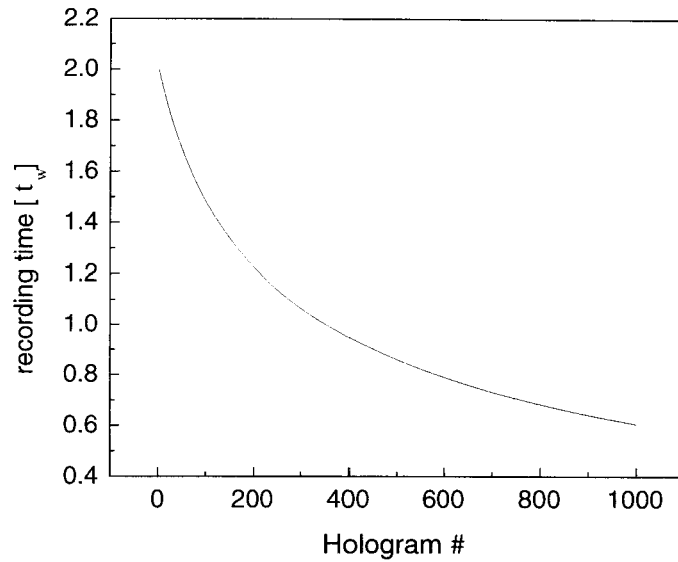


Figure 2.15: Exposure schedule computed from eqn. 4.11 for $M=1000$ holograms.

speed. We use a 0.85 mm thick crystal doped with 0.075 wt. % Fe_2O_3 and 0.01 wt. % MnO in transmission geometry. For localized recording, we use a green recording wavelength of 532 nm with a reference beam focused by a cylindrical lens yielding a lateral extension of $40\mu\text{m}$ ($1/e^2$ value). The violet sensitizing beam (401 nm) is co-propagating with the same the green reference beam. The signal has a diameter of 3 mm at the crystal. Each hologram is recorded up to saturation for a recording time equal to two writing time constants (green intensity= $100\text{ mW}/\text{cm}^2$, violet intensity= $10\text{ mW}/\text{cm}^2$, extra-ordinary polarization). Center to center spacing between adjacent holograms is $60\mu\text{m}$.

The total spatial multiplexing is done over 3mm. Figure 2.17(i) shows the diffraction efficiency of each recorded localized hologram immediately after each recording. An average diffraction efficiency of 2×10^{-2} is achieved. Some of the holograms are not recorded very well due to instabilities during the long recording time of each hologram (20 minutes). Fig. 2.17(ii) shows the final diffraction efficiency after the recording of all 50 holograms. It shows that the early holograms have been significantly erased due to the recording green signal beam and scattering from the violet sensitizing

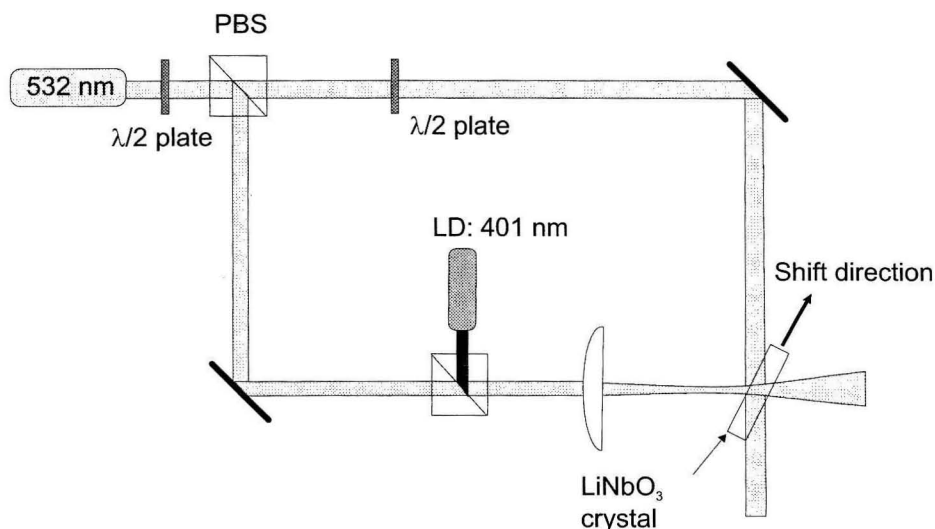


Figure 2.16: Set-up for the 50 strong holograms recording. LD: laser diode; PBS: polarizing beam splitter.

laser. The average diffraction efficiency is approximately 10^{-3} . The distributed volume recording experiment is performed using the same crystal [37]. Figure 2.18 shows the diffraction efficiency for 50 angle multiplexed holograms using ordinary polarization. The measured diffraction efficiency is equal to 5×10^{-5} for ordinary polarization and extrapolating from that experiment, the diffraction efficiency for extra-ordinary polarization will be 10 times higher (5×10^{-4}) due to the higher value of the electro-optic coefficient for extra-ordinary polarization. The diffraction efficiency obtained with the localized method is twice of that obtained with the distributed recording method. Eqn. 2.17 predicts that the diffraction efficiency obtained experimentally should be a factor 50 larger.

We can explain this discrepancy by three factors. The first factor is due to the finite erasure time constant of the grating stored in the manganese traps when using green recording beams. Due to the long recording time of each localized hologram, the total exposure becomes large enough to significantly erase the early holograms. According to fig. 2.14, the diffraction efficiency of the first hologram decreases by a factor of 4.17 from the saturation diffraction efficiency obtained after initial green erasure. The second factor is the erasure of adjacent holograms caused by the sensitizing beam. This erasure is caused by scattering from the crystal surface and fanning

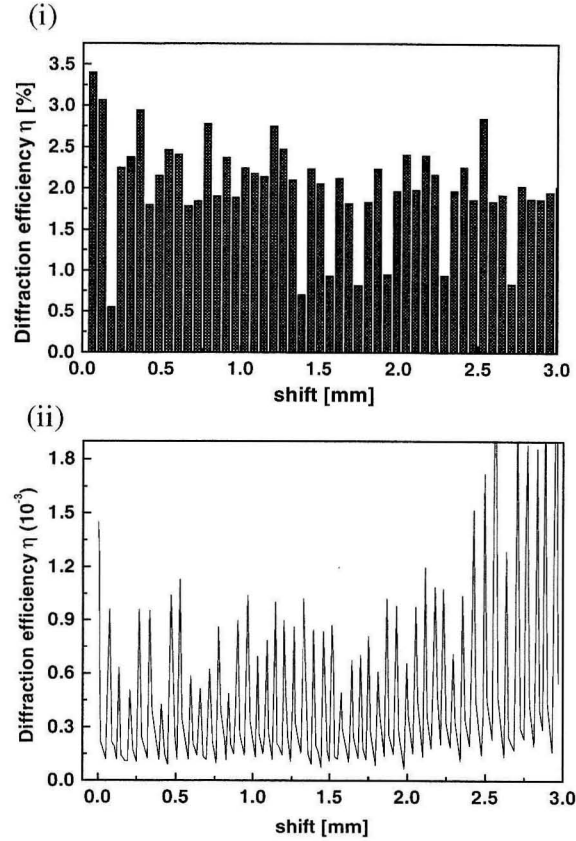


Figure 2.17: Diffraction efficiency η versus spatial location. (i) η of each localized hologram measured immediately after each recording; (ii) η measured after the recording of 50 holograms.

caused by the long recording time of each localized hologram. This factor varies with the center to center spacing of localized holograms. In this experiment, we found that the diffraction efficiency of adjacent holograms is decreased by a factor of 2.5 when the center to center spacing is 1.5 times the $1/e^2$ spot size. The third factor is due to the fact that the localized holograms are not adjacent ($20\mu\text{m}$ gap between two consecutive localized holograms). This gap causes a loss of 2.2 in diffraction efficiency. Overall, the saturation diffraction efficiency of each localized hologram is decreased by a factor of 22.9 which agrees well with values obtained experimentally. All three factors can be reduced or completely eliminated if the recording material

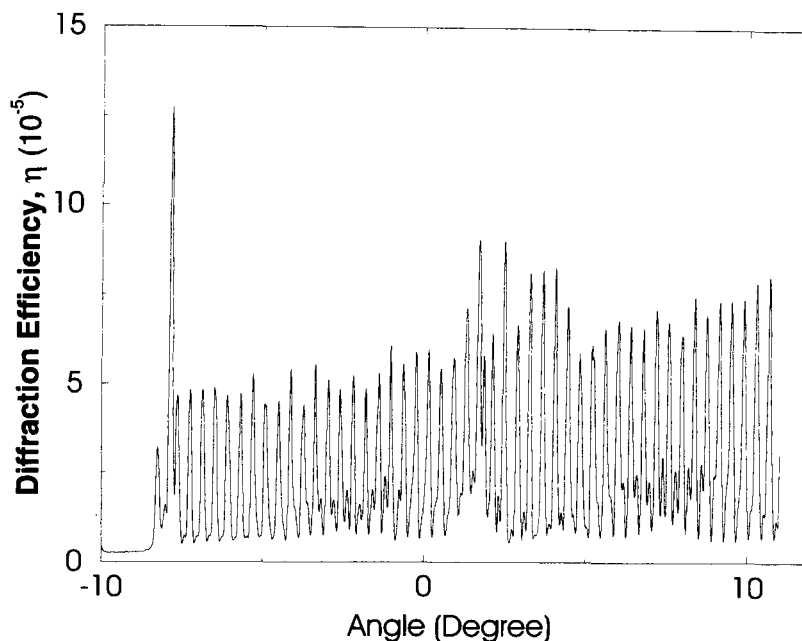


Figure 2.18: Diffraction efficiency η versus angle for 50-angle-multiplexed holograms.

properties can be improved to reduce erasure at the recording wavelength (this is true for red wavelength, but recording is slow in the red) and using coated and well polished crystals.

The main problem to solve in order to obtain larger $M_{\#}$ using localized recording is related to the sensitizing light. Since the focused beam has a gaussian shape, the localized holograms are spaced by twice the waist of the focused beam in order to avoid erasure of adjacent holograms while recording the next hologram. Even though the center to center spacing is equal to twice the waist, the erasure of adjacent holograms caused by the sensitizing beam shows a strong effect.

2.4 Physical justification of the $1/M$ dependence

In section 2.3, we showed by derivation that the diffraction efficiency of localized holograms follows a $1/M$ behavior where M is the number of holograms. In this section, we give an intuitive argument for this result. A paradox comes from the fact that the same number of electrons are available to build up the holograms for both methods, localized and distributed: why does the localized method yield a much

higher diffraction efficiency?

We start by noting that the maximum diffraction efficiency obtainable given a certain dynamic range follows a $1/M$ law, where M is the number of holograms. This result can be understood with the following arguments. The optical field is specified by an amplitude and phase mask. The field in the volume is found by propagating the field and is uniquely determined by the boundary conditions on the mask [68]. For monochromatic optical systems, the resolution (a pixel) is on the order of one wavelength of light λ . The number of degrees of freedom (or pixels) available on a mask of area A is $o(A/\lambda^2)$. The number of independent degrees of freedom inside a volume of crystal V is equal to the number of independent gratings that can be recorded: $o(V/\lambda^3)$ [69]. Therefore, a single monochromatic field cannot specify an arbitrary hologram. The number of degrees of freedom needs to be raised by a factor of $V/A\lambda$. A practical approach is to record $V/A\lambda$ exposures with the appropriate field distribution at each exposure. It has been shown [67] that the number of exposures M yields a $1/M^2$ dependence on the diffraction efficiency of each equalized hologram. However, if the field is coherent polychromatic with M wavelengths, the number of degrees of freedom is increased by M . Therefore, a single exposure with a field composed of M wavelengths illuminating a mask can specify the same hologram as if it is recorded with M exposures of the appropriate monochromatic field at each exposure. In the case of a polychromatic single exposure, the diffraction efficiency varies as $1/M$ [67]. The advantage of a polychromatic field over a monochromatic field is that coherence between different wavelengths can yield greater a modulation depth. For the multiple exposures method, there is no coherence effect between each exposure. Consider a grating recorded by two plane waves:

$$\begin{aligned} R_l &= R_o e^{\vec{k}_{rl} \cdot \vec{r} + \phi_{rl}} \\ S_l &= S_o e^{\vec{k}_{sl} \cdot \vec{r} + \phi_{sl}}. \end{aligned} \tag{2.29}$$

After M exposures, the perturbation modulation is equal to:

$$\epsilon(\vec{r}) \propto \sum_{l=1}^M \frac{\epsilon_o}{M} R_l \cdot S_l^* + c.c. = \sum_{l=1}^M \frac{\epsilon_o}{M} R_o \cdot S_o e^{\vec{K}_{rl,sl} \cdot \vec{r} + \phi_{rl,sl}} + c.c. \quad (2.30)$$

where $\vec{K}_{rl,sl} = \vec{k}_{rl} - \vec{k}_{sl}$ and $\phi_{rl,sl} = \phi_{rl} - \phi_{sl}$.

If each exposure is performed with the same plane wave propagation vectors, then $\vec{K}_{rl,sl} = \vec{K}$ and $\phi_{rl,sl} = \phi \forall l = 1 \dots M$. The perturbation 2.30 becomes:

$$\epsilon(\vec{r}) \propto \epsilon_o R_o \cdot S_o e^{\vec{K} \cdot \vec{r} + \phi}. \quad (2.31)$$

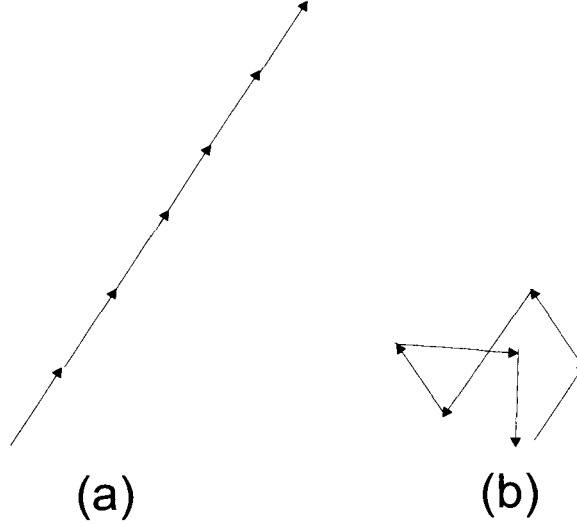


Figure 2.19: Vectorial sum of the grating vectors produced by the interference of two plane waves. (a) coherent addition; (b) random walk.

This is, in fact, a single exposure of a grating: the maximum modulation ϵ_o is achieved by coherent superposition of the product of the fields. When the multiple exposures are not coherent, i.e., when each exposure produces a grating with a different grating vector $\vec{K}_{rl,sl}$ and different phase $\phi_{rl,sl}$, the perturbation modulation is not maximized throughout the volume. In fact, if we consider the sum in eqn. 2.30 as a random walk, the standard deviation of the perturbation modulation grows as \sqrt{M} (fig. 2.19). This argument shows that the localized method uses more effectively the available dynamic range than the distributed method.

The $1/M^2$ dependence comes from multiple exposures as we have described. The diffraction efficiency is proportional to the square of the total index change Δn_o and to the square of the interaction length L . In the case of distributed recording, the dynamic range Δn_o is divided into M equal parts if we consider M exposures:

$$\eta_{dist} = \left(\frac{\Delta n_o}{M} L \right)^2. \quad (2.32)$$

In the case of localized recording, each localized hologram is recorded to saturation Δn_o and the interaction length is given by L/M such that:

$$\eta_{loc} = \left(\Delta n_o \frac{L}{M} \right)^2. \quad (2.33)$$

It seems that nothing is gained with localized recording. However, by writing down these equations, the diffraction efficiency is defined implicitly in terms of ratio of optical intensities. It is erroneous to compare both method using intensities (section 2.2). The correct diffraction efficiency is given by power ratio as is suggested by fig. 2.7. In this case, eqn. 2.33 is multiplied by a factor M that comes from the area of the incident beam divided by M . The diffraction efficiency then follows a $1/M$ dependence.

The localized method can be seen as an implementation of a cascade of thin holograms. If the thickness of the thin holograms can be of the order of one wavelength, then an arbitrary hologram can be built by recording many exposure of localized holograms. In the implementation that uses a cylindrical lens to generate the planes, the thickness of each plane is limited by diffraction. A system composed of two femtosecond pulses (10 fs duration) focused by a spherical lens into the LiNbO_3 crystal could generate the sensitizing light locally by non-collinear second harmonic generation. Due to phase mismatch, the frequency-doubled light cannot be generated for more than 1-2 μm in LiNbO_3 when the incident light is in the NIR (800nm). A two-dimensional scanning system would be needed to sensitize a thin page. Such a

system has not been built in the frame of this thesis, but could be an implementation for the generation of arbitrary diffractive optical elements.

2.5 Characterization of an optical memory based on localized recording

In this section, we experimentally demonstrate and characterize a memory module that features selective page erasure and read-out persistence using the localized recording method in doubly-doped LiNbO₃ developed in the previous sections. Pages of information can be selectively erased without partially erasing the whole memory. Data pages can be written over erased pages multiple times without exposure schedule. Information is read millions of times before refreshing is required. We quantify the optical quality of the holograms by measuring their signal to noise ratio (SNR) for a memory size up to 100 holograms. A compact phase conjugate read-out architecture is also presented and experimentally demonstrated. Using the compact architecture, one module reaches a capacity of 1.3 Gbit for a density of 1.3 bits/ μm^2 . In section 2.2, we demonstrated the feasibility of this scheme by recording multiple localized holograms. In this section, we report the experimental measurement of the SNR as a function of the number of localized holograms and their lateral extent (thickness of the focused plane). We also investigate the SNR after multiple selective refresh-erasure cycles of a localized hologram at the same location.

A typical recording erasing curve, using the set-up of fig. 2.20, and two recording plane waves (532 nm, 2mm diameter, ordinary polarization, 80 mW/cm² per beam, intensity of the violet beam is 20 mW/cm², wavelength=401 nm) is shown in fig. 2.21. The recording is done with the violet beam on. During read out, the violet beam is turned off and a reference beam with twice the intensity reads-out the hologram in the Bragg condition. The erasing curve is fitted with a bi-exponential function giving two time constants, $\tau_{e_1} = 1,083$ sec. and $\tau_{e_2} = 30,403$ sec., which correspond respectively to the fast erasure of the grating in Fe and a slower erasure of the grating in Mn [45]. The crystal was oxidized for 6 hours at 900 °C in an O₂ atmosphere. The oxidation state could not be further reduced by longer oxidation. The slow erasure time constant τ_{e_2} is about 15 times shorter than that obtained in a similar crystal with half the concentration of Fe₂O₃ (0.075 wt. % Fe₂O₃, transmission geometry)[12]. The

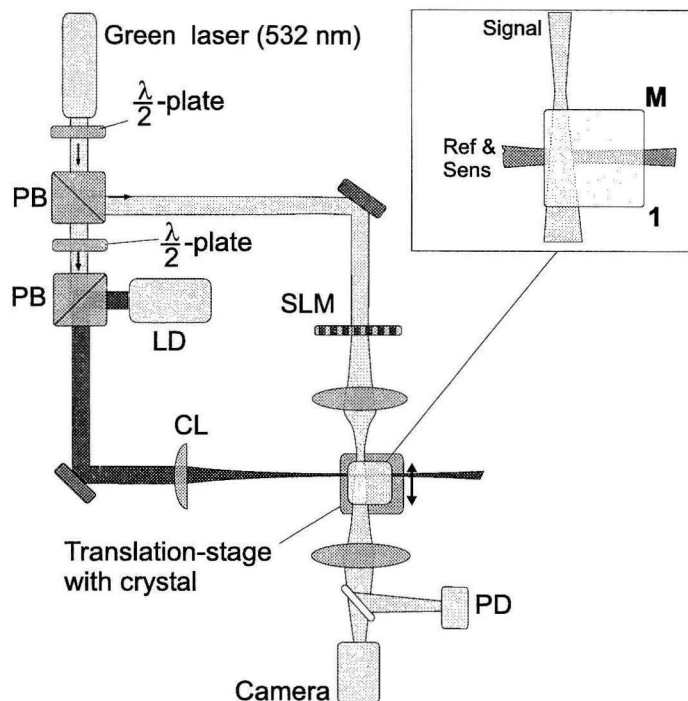


Figure 2.20: Recording set-up for the SNR measurement.

ratio of erasing time constant to the recording time constant is equal to $\frac{\tau_{e2}}{\tau_w} = 140$. The spectrums of both crystals are shown in fig. 2.22. In this figure, the spectrum of the crystal used in this experiment (#86D) still has remnant electrons in iron (peak center at 480nm) which explains the loss of persistence upon read-out.

The localized holograms are recorded with equal power in the reference and signal beams in order to maximize the recording slope, therefore minimizing the recording time of each hologram [46]. We observed that when holograms are not recorded to saturation, as is the case for the recording shown in fig. 2.21, the persistence upon read-out of the holograms varies with the recording time. The persistence parameter (β^2) is defined as the ratio between the diffraction efficiency after sufficient read-out (flat part of the erasing curve) and the diffraction efficiency immediately after recording. We experimentally measured the persistence as a function of recording time. Holograms are recorded using the set-up shown in fig. 2.20. Fig. 2.23 (a) shows recording and erasing curves for increasing recording times. The persistence (β^2) is extracted from the recording curves of fig. 2.23 (a). The result is presented

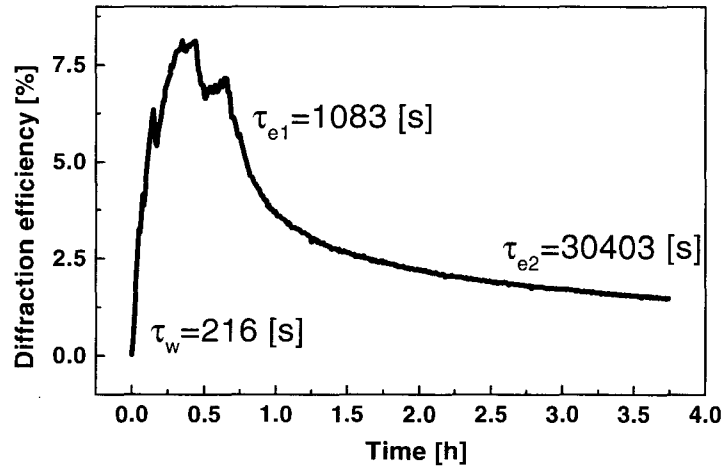


Figure 2.21: Recording and read-out curve for a plane wave hologram in a 90 degree-cut LiNbO₃ crystal doped with 0.15 wt. % Fe₂O₃ and 0.015 wt. % MnO. The recording beams are from a solid state green laser (wavelength 532 nm, ordinary polarization, 1/e² beam diameter 2.0 mm and intensity 80 mW/cm² per beam). The sensitizing light is from a laser diode (Nichia, wavelength 401 nm, linearly polarized, intensity 20 mW/cm²).

in fig. 2.23 (b). We observe that holograms recorded for short times have very poor persistence. This result is independent of the amount of pre-sensitizing time with the violet beam. We attribute this result to the dynamics of the recording. Bleaching and sensitizing in LiNbO₃:Fe:Mn are typically slow mechanisms. After the crystal is pre-sensitized for some time, the iron traps are filled up with electrons. During the early recording period, the grating is mainly built with electrons coming from the filled up iron centers. After sufficient recording time, equilibrium is reached between the rate of electrons transferred from Mn to Fe and vice versa. The grating is then efficiently recorded in the Mn centers and persistence reaches a stable value. For recording in the green at 532 nm, the maximum persistence obtained is $\beta^2 = 0.34$, meaning that about a third of the diffraction efficiency remains after initial erasure. When the memory is recorded initially using the localized method, it is important to record the holograms for an amount of time enough to achieve maximum persistence.

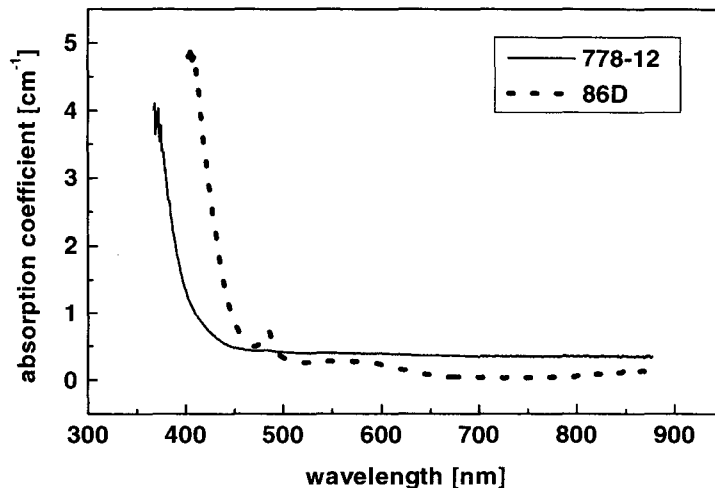


Figure 2.22: Spectrum of the 90 degree crystal used in the SNR experiment (#86D, 0.15 wt. % Fe_2O_3 and 0.015 wt. % MnO) and 778-12 (0.075 wt. % Fe_2O_3 and 0.015 wt. % MnO).

The final diffraction efficiency of the holograms after the memory is written will then be maximized.

2.5.1 SNR of localized holograms

We present the SNR of reconstructed holograms for two experiments. In the first experiment, a focused reference beam with a $1/e^2$ lateral spot size equal to $100\mu\text{m}$ is used. In the second experiment, the focused reference beam has a lateral spot size equal to $25\mu\text{m}$. The lateral spot size $W(z)$ in the crystal increases with distance z as $W(z) = W_o \left(1 + \frac{z}{z_o}\right)^{\frac{1}{2}}$, where $z_o = \frac{\pi W_o^2 n}{\lambda_o}$ is the depth of focus, W_o is the waist at focus and n is the index of refraction for ordinary polarization.

The set-up for SNR measurement is the one shown in fig. 2.20. The reference beam is focused by a cylindrical lens of focal length 4 cm. The sensitizing beam from a laser diode (Nichia, 401nm) is co-propagating with the green (Coherent, 532 nm, ordinary polarization) reference beam. A Spatial Light Modulator (SLM) of 640×480 pixels is used to display random binary patterns. The 4-f imaging system is not pixel matched.

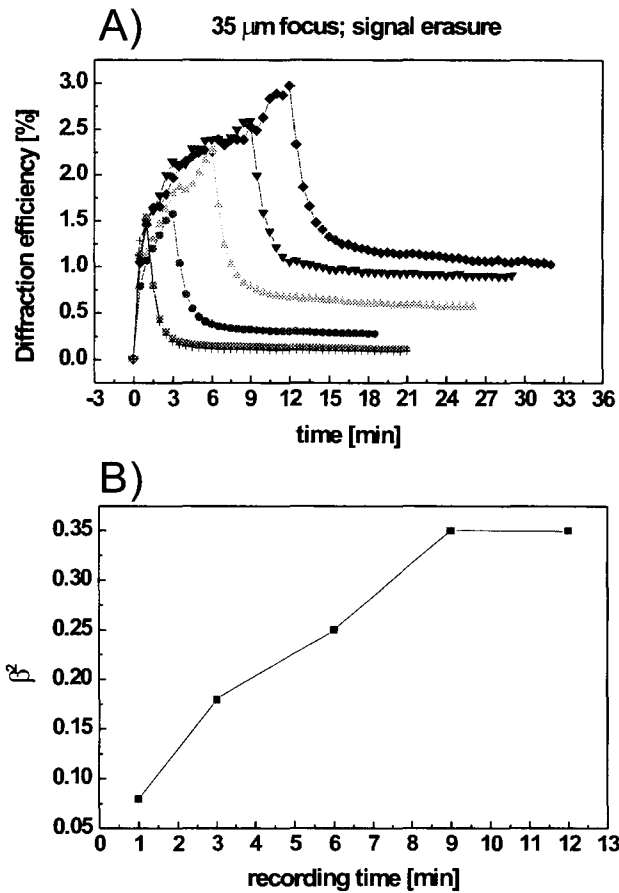


Figure 2.23: a) Recording curves with a focused reference green beam (wavelength=532 nm, spot size= $30\mu\text{m}$ ($1/e^2$ value)) and erasing with reference beam only. The different curves are recorded with increasing exposure. b) Persistence β^2 as a function of recording time.

Instead 4×4 SLM pixels are used to represent 1 data pixel. The imaging system from the SLM to the detector array consists of an achromat lens with $F/\# = 2.5$ placed in front of the SLM and an objective Nikon lens with $F/\# = 1.4$. The imaging system's magnification of 0.29 allows us to image the entire SLM surface onto the camera. A removable mirror can be placed after the second imaging lens to measure the diffracted power while leaving the camera in place. The focal plane of the first lens is located 3mm before the crystal's surface; therefore, the holograms are recorded in the Fresnel region. An iris is placed at the focal plane of the first imaging lens to filter out the high orders generated by the SLM. The signal beam propagates through

the crystal close to one of its edges. This ensures that the violet light sensitizes efficiently the entire area to be recorded as shown in the inset of fig. 2.20. The holograms are recorded from position 1 (exit crystal facet) to M (entrance crystal facet). In this configuration, the signal beam interferes with the reference beam before it propagates through the recorded holograms, thus reducing distortion of the signal. At the overlap between the focused reference and the signal beam, the signal diameter is 1.5mm. The experiments in this chapter are performed with a congruent 90 degree-cut LiNbO₃ crystal doped with 0.15 wt. % Fe₂O₃ and 0.015 wt. % MnO. The crystal dimensions are 1×1×1×cm³. The signal, reference and violet beam intensities are 30 mW/cm², 300 mW/cm² and 100 mW/cm², respectively, for the 100μm spot size experiment. For the 25μm spot size experiment, the intensities are 60 mW/cm², 200mW/cm² and 600mW/cm² respectively. A diffraction efficiency of $5 \cdot 10^{-5}$ is the smallest value that yields a good contrast image on a video camera sampling at 30Hz, from which we compute the SNR. The spacing between each localized hologram is chosen to be twice the lateral spot size to avoid erasure of the previous hologram while sensitizing the next hologram. Each hologram is sensitized for 5 minutes and recorded for 3 minutes with a different random binary bit pattern displayed on the SLM. No exposure schedule is needed to write the entire memory.

Figs. 3.10 and 2.25 show the diffraction efficiency versus position for the first and second experiment, respectively. Each peak corresponds to the diffraction efficiency of a hologram stored at a different spatial location as the crystal is translated in the direction perpendicular to the reference beam. Samples of reconstructed holograms from both experiments are shown in fig. 2.26 and fig. 2.27.

To measure the SNR, we use 5 windows of 30×30 superpixels (1 superpixel is composed of 4×4 camera pixels) located on the 4 corners and at the center of the image. For each superpixel, the edges are left out, so effectively 3×3 pixels form a superpixel. SNR is computed using the formula:

$$SNR = \frac{\mu_1 - \mu_0}{\sqrt{\sigma_1^2 + \sigma_0^2}}, \quad (2.34)$$

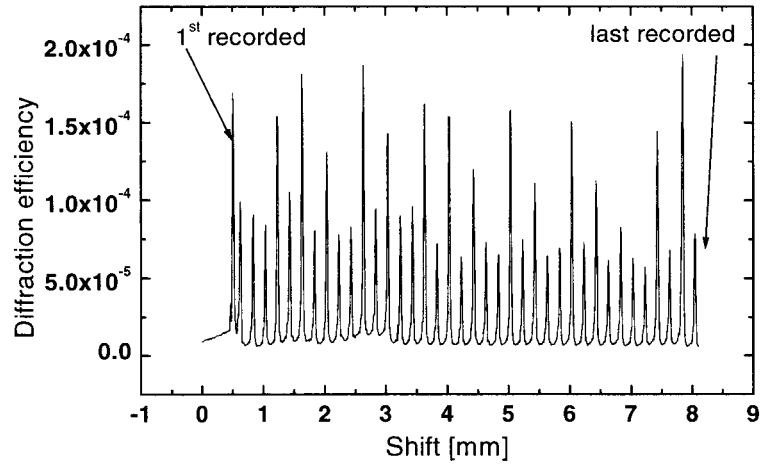


Figure 2.24: Recording of 40 localized holograms. The plot shows the diffraction efficiency versus the spatial shift of the crystal.

Where μ_i and σ_i , $i=(0,1)$ are the mean and variance, respectively, of the fitted Gaussian distribution of ones and zeros. Histograms corresponding to three holographic reconstructions are shown in fig. 2.26 and fig. 2.27. The SNR is computed for holograms located in the front, middle and rear of the crystal.

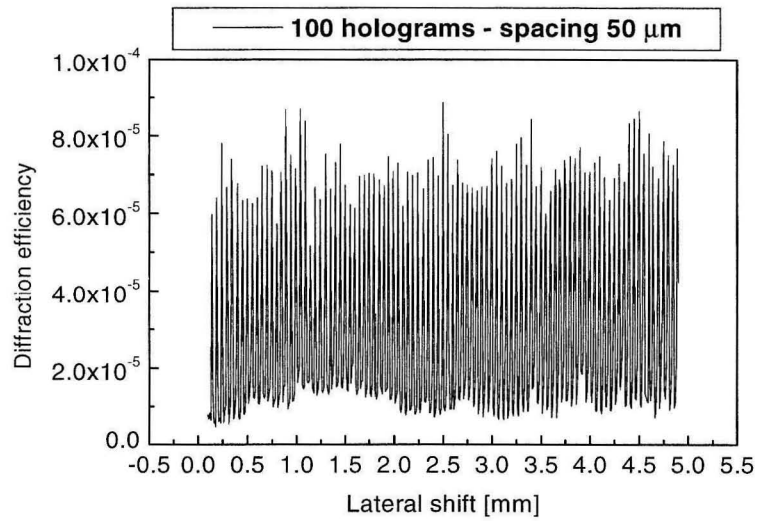


Figure 2.25: Recording of 100 localized holograms. The plot shows the diffraction efficiency versus the spatial shift of the crystal.

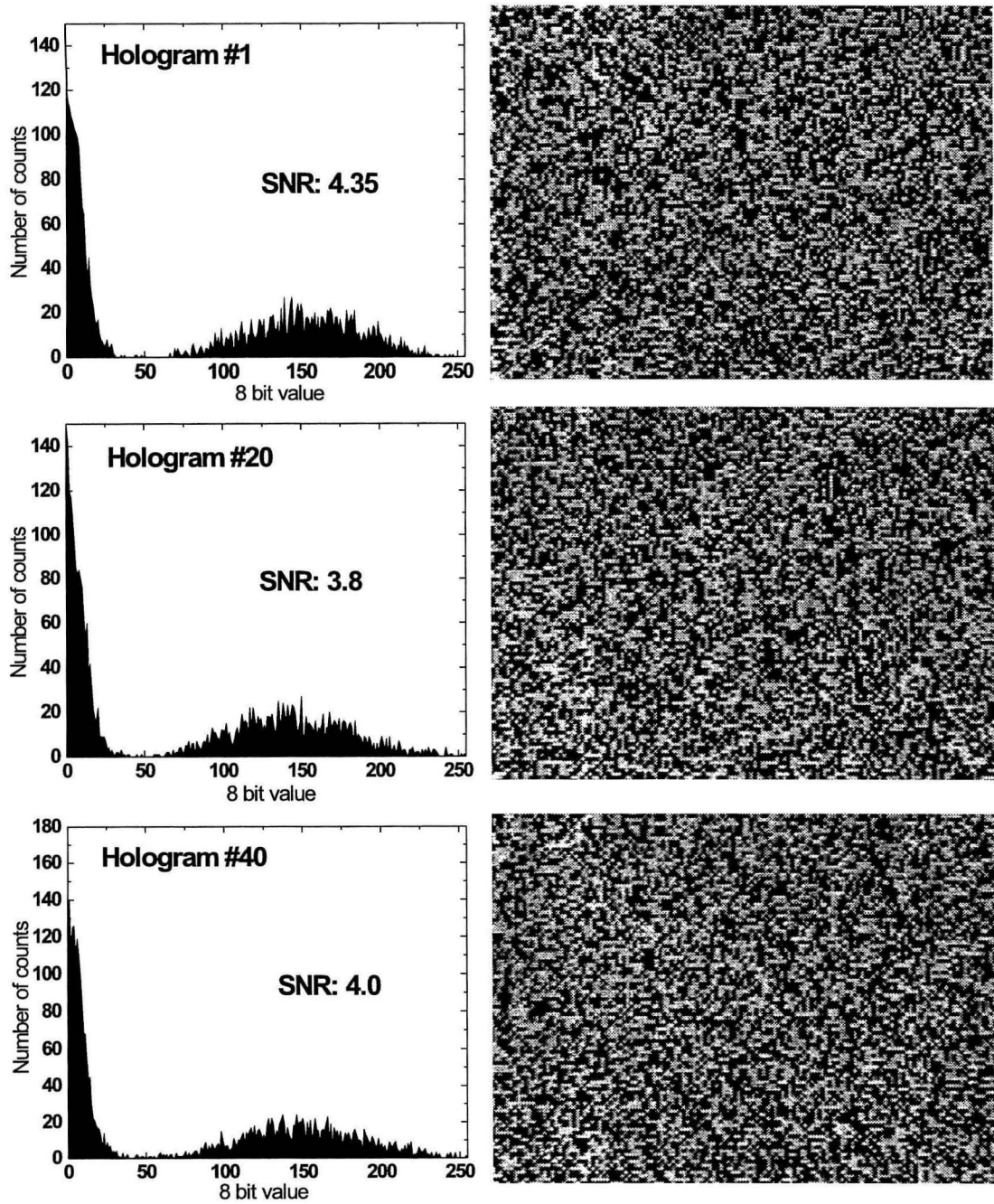


Figure 2.26: Three sample reconstructions and SNR values from the 40 holograms.

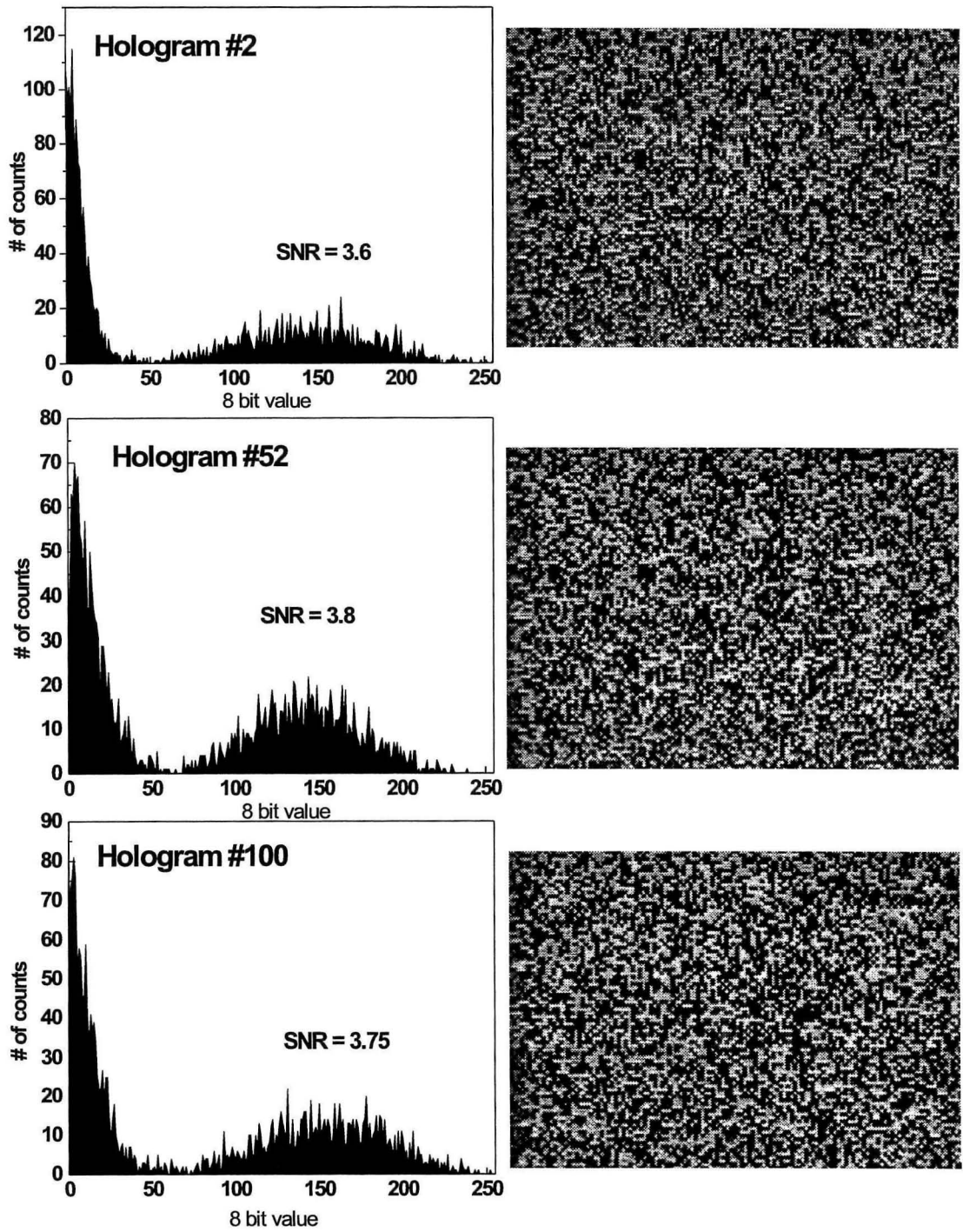


Figure 2.27: Three sample reconstructions and SNR values from the 100 holograms experiment.

The average SNR value is 4.2 for the experiment with a $100\mu\text{m}$ lateral spot size and 3.7 for the experiment with a $25\mu\text{m}$ lateral spot size. In both experiments, the SNR is uniform across the crystal. We attribute the loss in SNR of 0.5, when the lateral spot size decreases from $100\mu\text{m}$ to $25\mu\text{m}$, to the longer exposure of the crystal illuminated by the signal beam during the second experiment of 100 holograms. The remnant electrons in Fe act as absorption centers for the green (532nm) light and produce fanning. The direct imaging of the SLM through the crystal after the storage of 100 hologram in experiment 2 shows a degradation of the SNR by 1 compared to the SNR measured before the full storage. Fig. 2.28 and 2.29 summarize the SNR measurements for both experiments. These results show that the SNR of a single hologram does not decay when the spot size of the reference beam is reduced, which suggests that an even smaller focus could be used; however, fanning of the signal beam becomes the limiting factor when long exposures are needed.

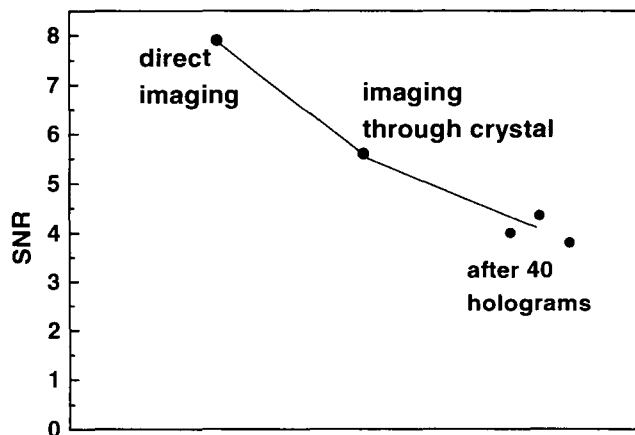


Figure 2.28: SNR comparison: (a) direct imaging; (b) imaging through crystal; (c) after 40 holograms.

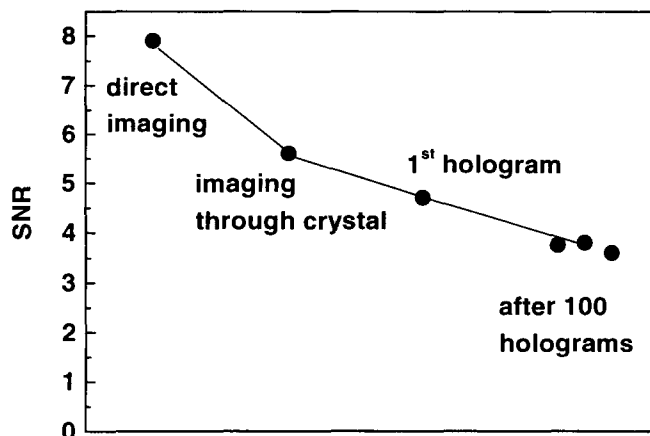


Figure 2.29: SNR comparison: (a) direct imaging; (b) imaging through; crystal(c) first hologram; (d) after 100 holograms

2.5.2 Selective erasure cycles

Localized recording allows selective erasure of a particular page of data without affecting the other pages. In this section, we investigate the effect of multiple erasure-refresh cycles on the SNR for the two reference beam spot sizes ($100\mu\text{m}$ and $25\mu\text{m}$).

Seven holograms are recorded with a reference beam lateral spot size of $100\mu\text{m}$. The center hologram is then erased and refreshed 55 times. The green reference and violet beams are used together to erase the hologram. The hologram is refreshed for 3 min. and erased for 10 min. The beam intensities were the same as in the previous experiments. The experiment lasted 12 hours. Fig. 2.30 shows a plot of the diffraction efficiency versus spatial position before and after the 55 erase-refresh cycles. The bottom plot is a finer measurement of the diffraction efficiency vs position. It illustrates that there is no broadening of the selectivity curve due to the erase-refresh cycles. The immediate adjacent holograms are almost totally erased after the process. This is due to fanning caused by both the green reference and sensitizing beams. The SNR of the recycled holograms before and after the 55 cycles are identical and equal to 4.5 as shown in fig. 2.31.

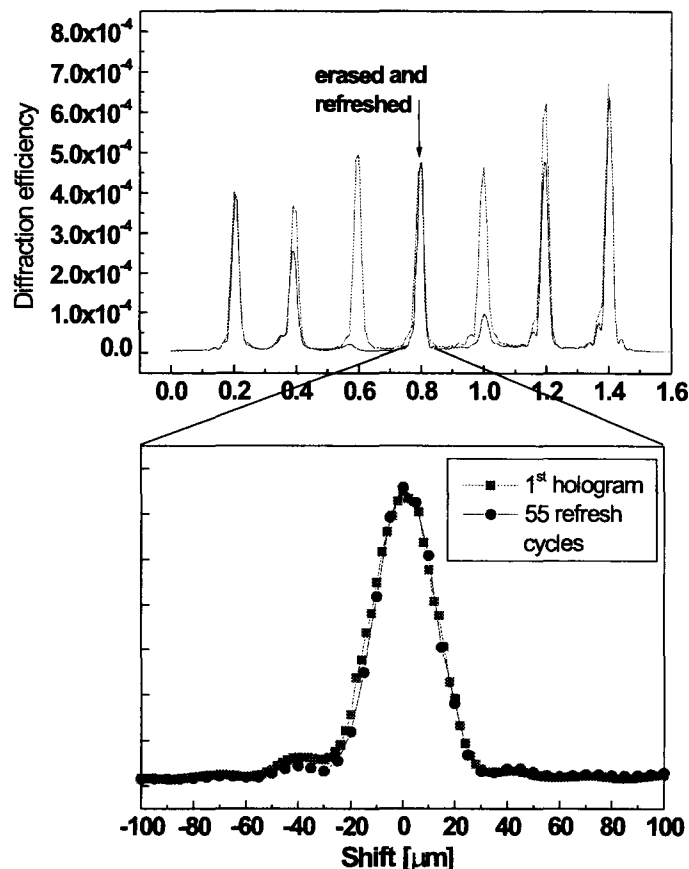


Figure 2.30: Diffraction efficiency vs spatial shift before and after 55 refresh cycles of the central hologram - - $100\mu\text{m}$ reference focus.

An identical experiment is performed with a smaller lateral spot size of the reference beam of $25\mu\text{m}$. After 55 erase-refresh cycles, fig. 2.32 shows that the small focused reference beam does not influence the selectivity of the central hologram. We observe an erasure asymmetry of the adjacent holograms caused by ultra-violet erasure. The two adjacent holograms located on the same side to the left of the central hologram are erased totally whereas the adjacent hologram on the right is erased by half its original value. This erasure is due to the preferential fanning direction to one side. When the reference spot size is reduced, the intensity of the green recording beam and sensitizing beam increases, enhancing the effect of fanning which causes erasure of farther neighbouring holograms. The SNR before and after the erasing-refreshing cycles is unchanged and equal to 4.6 as shown in fig. 2.33.

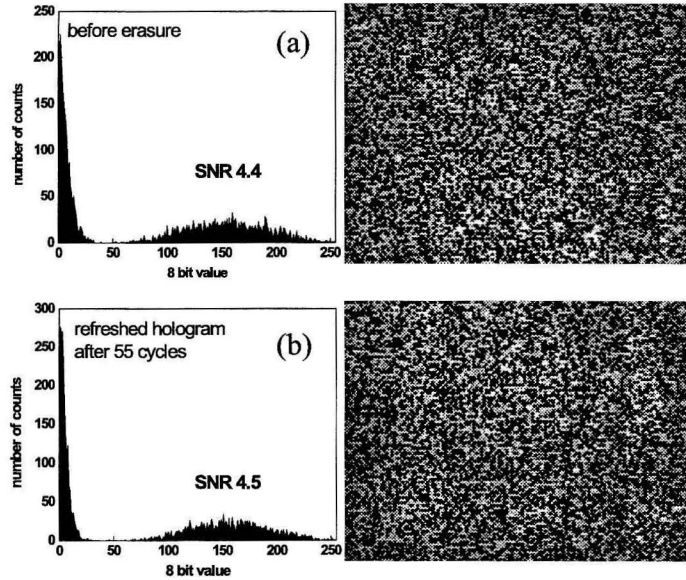


Figure 2.31: Histogram and reconstruction of the central hologram before and after the refresh cycle - $100\mu\text{m}$ focus.

These SNR values are similar to that obtained with distributed volume recording. It demonstrates that localized recording is a promising approach towards a practical selective read-write optical memory. A limitation of the experiment shown above is the memory capacity. In order to increase the capacity, a longer crystal could be used, but practically, the crystal length is limited because the signal beam needs to be coupled in the crystal without bouncing off the walls. Addressing the hologram location is slow in this experiment since the crystal needs to move. We present the following implementation that allows the memory capacity to grow linearly with the crystal length. This implementation also has a fast access time because the reference beam, instead of the crystal, is moved.

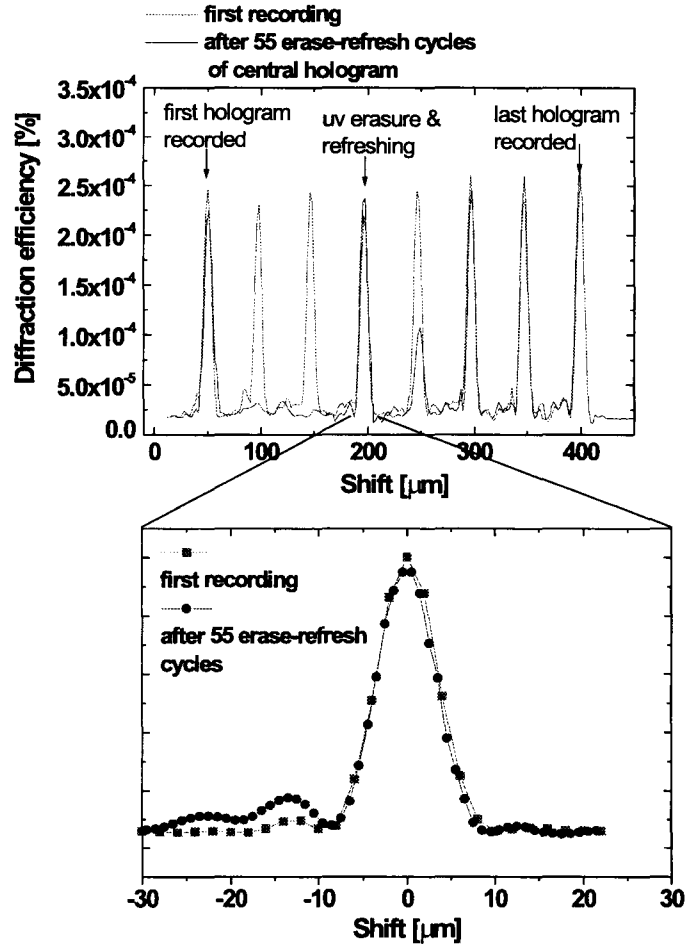


Figure 2.32: Diffraction efficiency vs spatial shift before and after 55 refresh cycles of the central hologram - $25\mu\text{m}$ reference focus.

2.5.3 Phase conjugate implementation

Fig. 2.34 illustrates the geometry implementing phase conjugation. In this architecture, the reference beam focus spot size can be very small and the signal beam diameter is kept constant throughout the crystal by bouncing off the crystal walls. The signal beam picks up information from the SLM and is focused into the crystal, positioned close to the Fourier plane of the lens. The crystal slab acts as a waveguide for the signal beam. The signal lateral dimension is then limited by the crystal thickness. Forward reconstruction would yield a distorted image due to the waveguiding effect. When the conjugate reference beam illuminates the hologram, the waveguiding effect is effectively "un-done" and the image can be recovered by the beam splitter

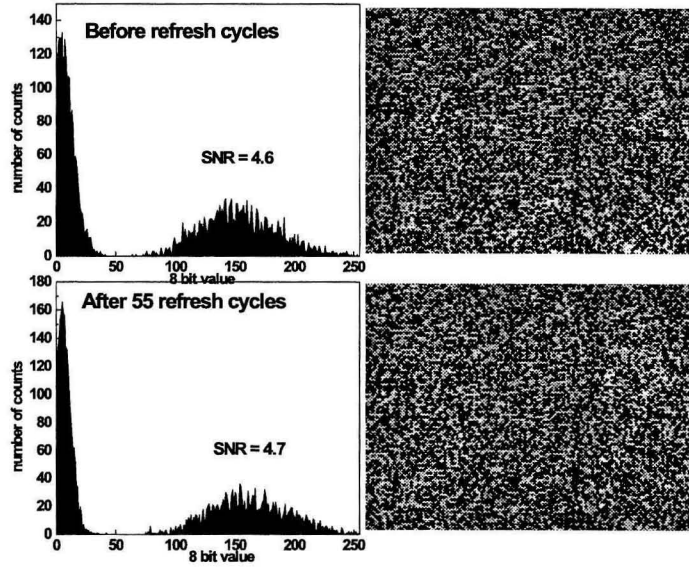


Figure 2.33: Histogram and reconstruction of the central hologram before and after the refresh cycle - $25\mu\text{m}$ focus

placed in front of the crystal. Referring to fig. 2.34, the reference and conjugate beam are produced by the first beam splitter. The second polarizing beam splitter placed in the conjugate reference arm generate the signal beam. The waveplates are placed to create a vertical polarization for the conjugate and signal beam. The conjugate and reference beams are focused by the cylindrical lenses Cl2.($f=20\text{cm}$) and Cl3.($f=20\text{cm}$), respectively. Both focused beam spot sizes are equal to $25\mu\text{m}$. We use a crystal slab of LiNbO_3 doped with 0.1 wt. % Fe_2O_3 with dimensions $1\text{mm} \times 20\text{mm}$ (along the signal beam direction) $\times 10\text{mm}$. The crystal is positioned at the focus of the conjugate and reference beams which are counter-propagating. The reference beam is incident on the crystal near the middle of the crystal. The signal beam is focused by the cylindrical lens Cl1.($f=7.5\text{cm}$) into the crystal. The SLM is implemented by a mask of a random bit pattern of pixel size $80 \times 80\mu\text{m}^2$. The spatial selectivity of the hologram using the forward and conjugate reconstruction is shown in fig. 2.35.

The forward reconstruction shows a clean selectivity curve with $20\mu\text{m}$ selectivity. We observe a broadening of the selectivity curve for the phase conjugate read-out. The broadening is due to the fact that the phase conjugate beam is not a true phase conjugate.

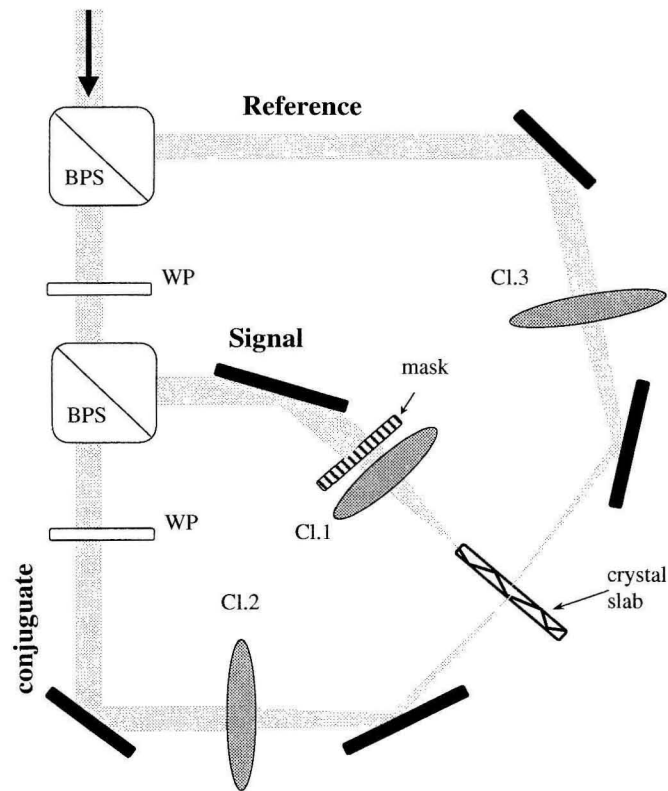


Figure 2.34: Experimental set-up of the phase conjugate memory module. WP= half wave plate. BSP= polarizing beam splitter. Cl= cylindrical lens.

A compact implementation is presented in fig. 2.36.

A planar mirror is placed at the focal plane of the cylindrical lens behind the crystal slab. The c axis of the crystal is oriented in such a way that the recording can occur only after the reference beam is reflected off the mirror. The reference beam incident on the crystal becomes the phase conjugate read-out. A shutter placed between the crystal and the mirror prevent the reflected beam to read-out the forward hologram. The selectivity curve of the phase conjugate read-out is shown in fig. 2.36. We observe again a broadening of the selectivity curve upon phase conjugate read-

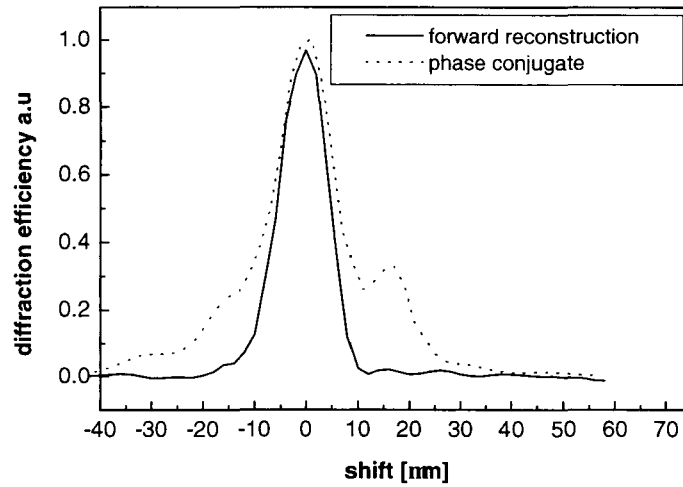


Figure 2.35: Spatial selectivity of the forward and conjugate reconstruction.

out, but to a lesser extent than with the implementation of fig. 2.34. This suggests that the broadening comes from aberrations of the cylindrical lens. The SNR of the reconstruction is measured as explained above. Results are shown in fig. 2.37. The SNR of the conjugate reconstruction is equal to 4 and demonstrate the practicality of the reconstruction by phase conjugation using a small focused beam in a crystal slab.

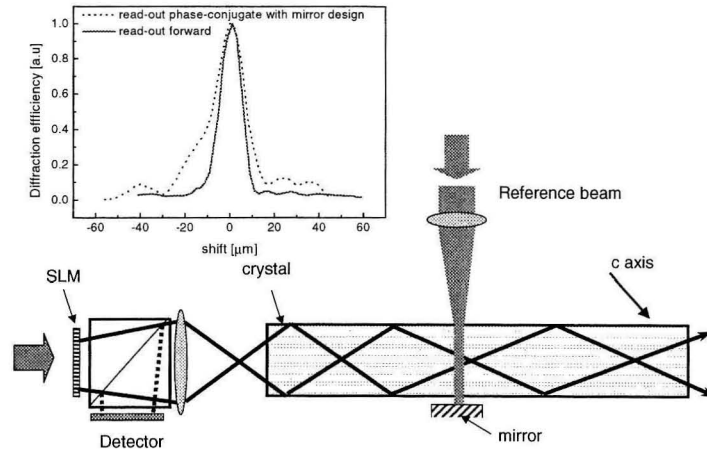


Figure 2.36: Compact module using a mirror for phase conjugation. Also shown is the spatial selectivity of the forward and conjugate reconstruction.

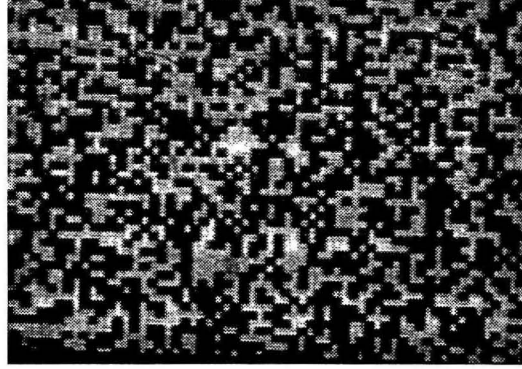
2.5.4 Memory capacity

Using the phase conjugate implementation, and the architecture of fig. 2.38, the memory capacity can be computed as follows. We assume that the crystal has transverse dimension H by D . The pixel size is denoted by b . The SLM has $N_H \times N_D$ pixels and dimensions $H \times D$. The SLM is placed in front of the beam splitter and the detector array is placed below the beam splitter in order to grab the phase conjugate reconstruction. The number of data pages M that can be recorded in a crystal of length L is equal to:

$$M = \frac{L}{2W(H)}. \quad (2.35)$$

where $W(H)$ is the waist of the focused reference beam after propagating a distance H . Given the crystal thickness H , the optimal waist W_o that minimizes diffraction is equal to $\sqrt{\frac{\lambda H}{n}}$, where n is the index of refraction of the crystal. $W(H)$ is then equal to $2W_o$.

The crystal thickness H is equal to the SLM vertical size $N_H b$, where b is the pixel size. Eqn. 2.35 is then equal to:



Phase conjugate reconstruction

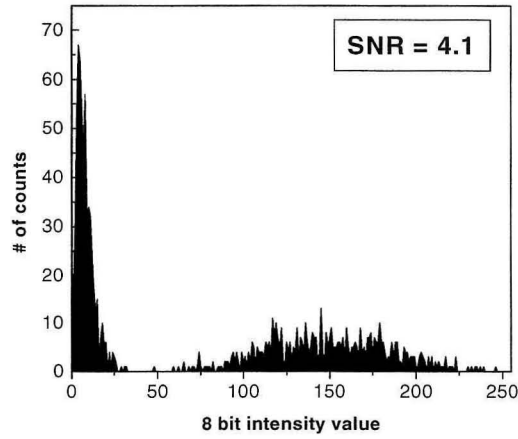


Figure 2.37: Reconstructed hologram by phase conjugation.

$$M = \frac{L\sqrt{n}}{4\sqrt{\lambda N_H b}}. \quad (2.36)$$

Choosing the pixel size $b=2\mu\text{m}$, and crystal dimensions $H=0.2\text{ mm}$, $D=20\text{ mm}$ and $L=50\text{ mm}$ yields $N_H=200$ and $N_D=5000$. The capacity is found by multiplying the result of eqn. 2.36 by the number of pixel per page ($N_H \times N_D=10^6$). The result is a capacity of 1.3 Gbit in a volume of $V=H \times D \times L=2\text{ cm}^3$. In terms of surface density (the depth is only 200 micrometers), the same calculation gives $1.3\text{ bits}/\mu\text{m}^2$. Volume holographic storage can reach surface capacity of hundreds of bits per micrometer

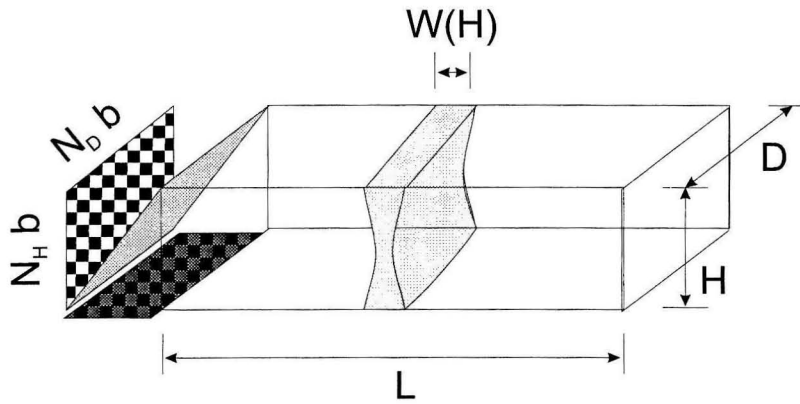


Figure 2.38: Memory capacity of the phase conjugate module.

square by superimposing holograms in the same volume. Here, the method we present is based on spatial multiplexing, i.e., consists of non overlapping holograms. Such a restriction reduces the memory capacity, but offers the nice property of selective erasure/refreshing of data pages and parallelism for high data rate.

In conclusion, we presented the SNR measurements of a novel selective read-write memory based on spatial multiplexing. The good SNR measurements obtained ($\simeq 4$) are encouraging for the practical development of holographic memories. We presented a compact module using phase conjugate reconstruction that allows greater memory capacity.

2.6 Pulse shaping

We have shown that the gating effect in $\text{LiNbO}_3:\text{Fe,Mn}$ enables new holographic storage systems (chap. 2). We show in this section that the gating effect can be used effectively in optical temporal pulse shaping as well. The development of ultra-fast laser sources have generated various methods for shaping the temporal optical field. Among them, Fourier plane filtering [47, 48] and holographic filtering are popular methods.

The idea of using holography for controlling the temporal optical field is not new [67]. The reflection geometry is used because it maximizes the spectral sensitivity and the time-bandwidth product of the diffracted pulse. The incident and diffracted pulse propagate in opposite direction, as shown in fig. 2.39. An optical memory can be constructed in the temporal domain as follows. An incident short pulse is diffracted from the hologram and produces a series of pulses representing bits in the temporal domain. The hologram is a spatial perturbation of the index of refraction which is then transferred as a temporal signal to the diffracted pulse [51].

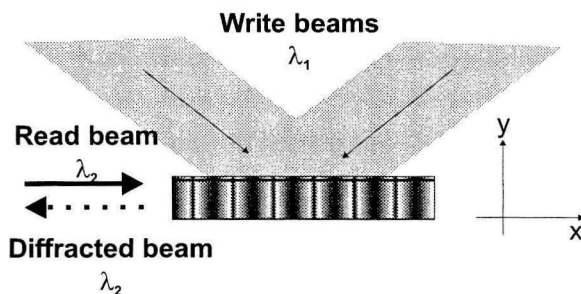


Figure 2.39: Reflection geometry for temporal pulse shaping. The writing beams are plane waves interfering in the medium producing a grating vector in the direction of the read beam propagation.

One recording scheme is to modulate the amplitude of a single grating to create strong reflections where the grating is strong. A single pulse can generate a shaped pulse containing N temporal bits of information when the spatial amplitude modulation of the hologram is written proportionally to the shape of the N bits stream. By varying the spatial intensity of one of the write beams, an amplitude-modulated grating can be formed [50] (fig. 2.39). The refractive index perturbation is expressed

as:

$$\Delta n \propto A(x) e^{j(K_g \cdot x + \phi)} \quad (2.37)$$

where $K_g = 2\pi/\Lambda$ and Λ is the grating period. If multiple scattering is neglected (small index perturbation), the diffracted pulse is equal to $A[(x + ct)/2] e^{j(k \cdot x + \omega t)}$, where k and ω are the pulse carrier propagation constant and carrier frequency, respectively.

The coding scheme of eqn. 2.37 works for weak gratings. For strong gratings, multiple scattering becomes important and degrades the diffracted pulses. In the case of strong gratings, the different bits can be recorded with slightly different grating periods. The light scattered by each bit is not scattered by the other bits, because of Bragg mismatch. This scheme requires as many exposures as the number of bits [51]. By using the gating properties of holographic recording in doubly doped lithium niobate, the amplitude modulation can be separated from the writing beams. The amplitude modulation is encoded onto the sensitizing beam independently. Only regions illuminated by the sensitizing beam enable the recording. The recording of many gratings in a gated medium like doubly doped Lithium niobate is efficient. The recording yields higher diffraction efficiency because subsequent gratings are not erased (due to persistence) by subsequent exposures and the recording is limited to the spatial localization of the appropriate bits (due to gating).

In the experiment described in this section, we demonstrate pulse shaping in $\text{LiNbO}_3:\text{Fe},\text{Mn}$ by using single grating amplitude modulation (eqn. 2.37). A train of 10 pulses of duration 4 ps was generated successfully with good uniformity from a single femtosecond pulse.

The experimental set-up is illustrated in fig. 2.40. An amplitude mask consisting of a series of dark vertical lines is illuminated by a collimated beam from a blue laser diode (Nichia, 401 nm, 1mW) and placed against a 5.0 mm long $\text{LiNbO}_3:\text{Fe}:\text{Mn}$ crystal. The lines are $250 \mu\text{m}$ thick and separated by $250 \mu\text{m}$. In the experiment, the recording beams are provided by the CW cavity of the MIRA femtosecond laser from

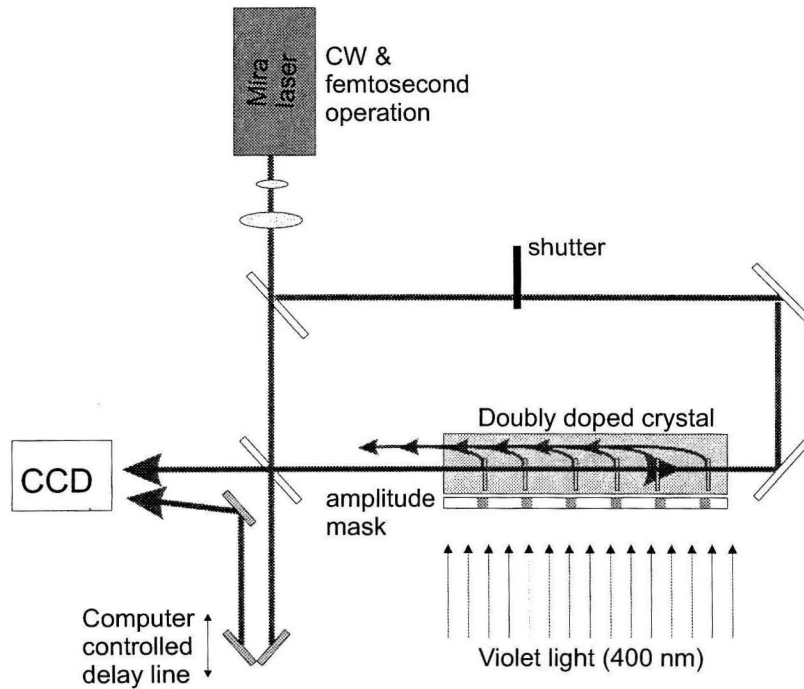


Figure 2.40: Pulse shaping recording set-up.

Coherent. The hologram is written in the reflection geometry with wavelength of 730nm, beam diameter of 3mm and power of 50 mW. After recording, the hologram is read-out in order to erase the grating stored in the iron centers revealing only the non-volatile grating stored in the Mn centers [12]. Upon read-out, the cavity of the MIRA laser is changed to femtosecond operation. The pulse duration is measured by autocorrelation using a non-linear second order correlator. The pulse duration can be extracted from the second order correlation measurement shown in fig. 2.41. Assuming a Gaussian pulse, the pulse duration is equal to 350 fs.

A beam splitter splits the femtosecond beam into a probe reference and a read-out pulse. Because the duration of the diffracted pulses are much longer than the probe pulse duration, the shape of the diffracted pulse can be measured by first order cross correlation with the probe beam ([50]). To perform the first order cross correlation, part of the probe beam is split by a beam splitter and passed through a variable-delay path before recombining with the diffracted beam. The probe and the signal recombine with a small angle between them so that an interference pattern can be detected by a CCD camera (fig. 2.40). The strength of the interference is measured

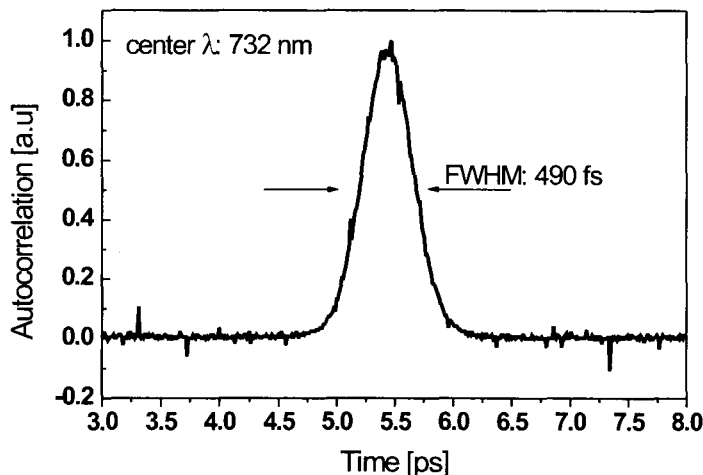


Figure 2.41: Second order autocorrelation of the probe beam in a BBO crystal.

as a function of the variable delay. The variable delay is created with a right angle mirror mounted on a computer controlled translation stage. At each position of the motor, the interference pattern is digitized by an 8 bit frame grabber. A full scan is composed of 300 images covering 110 ps. One of the digitized images showing an interference pattern is displayed on fig. 2.43 (top).

The intensities of the probe (I_{DC1}) and signal beam (I_{DC2}) are recorded for each position of the motor and represent the DC component of the interference pattern. Due to the inhomogeneity of the probe and signal beam, the DC components (I_{DC1}, I_{DC2}) are subtracted from the interference pattern as shown in fig. 2.43. A fast Fourier transform of the resulting DC-removed-interference pattern is performed separately across 20 lines of the image, and the strength of the interference is determined by summing the spectral component corresponding to the interference fringe spacing.

The result shown in fig. 2.42 (a) is a pulse diffracted from a grating with no modulation. The diffracted pulse broadens to 77 ps as expected ($\Delta T = \frac{2nL}{c} = 75.7$ ps using $n=2.27$, $L = 5$ mm). The diffraction efficiency for *cw* light was 1% in the experiment. Fig. 2.42 (b) shows the temporal variation of the diffracted pulse from the

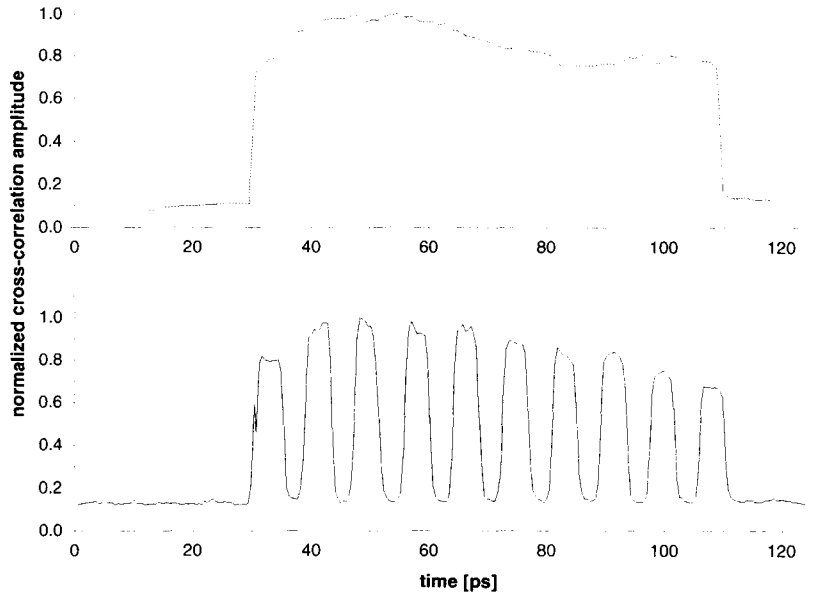


Figure 2.42: Linear cross correlation with the femtosecond source pulse and the diffracted pulse. a) grating with no modulation; b) grating with amplitude modulation.

modulated grating. The set of $250\ \mu\text{m}$ thick lines produced by the mask corresponds to a train of pulses of duration $3.78\ \text{ps}$, which matches the experimental results of $3.8\ \text{ps}$. The pulses show very good uniformity. The diffracted pulse in this experiment carried 20 bits of data.

The sensitizing beam simplifies considerably the recording. In non-gated material, the desired amplitude modulation is first decomposed into its Fourier components and the hologram is constructed by multiple recording of discrete gratings with appropriate phase and carrier frequency. The index modulation Δn decreases proportionally to the number M of required single gratings ($\Delta n = \Delta n_o/M$). In gated materials, such as doubly doped LiNbO_3 , the amplitude modulation is implemented by direct illumination of the sensitizing beam. Although many exposures are necessary with the doubly doped material as well, the recorded gratings are independent. The index modulation can reach its maximum value Δn_o for each localized grating which results in a larger diffraction efficiency.

Stronger holograms can be recorded using green light recording beams in doubly doped LiNbO_3 (section 2.3.1). When the read-out pulse has a longer wavelength, the recording can be performed using the set-up of fig. 2.44. In this set-up, the expanded plane waves record a grating in the transmission geometry through the crystal's face that is orthogonal to the read-out face. By using waveguides instead of bulk crystal, the amplitude modulation can be uniform in depth and produces features with micrometer size by using projection systems similar to those used in photolithography. The quantity of information in a shaped pulse is computed by the time-bandwidth product $TBP = T \frac{1}{\tau}$, where T is the round trip delay in the material and τ is the incident pulse duration. If we assume a 2 cm length crystal and a 15 fs pulse duration, the maximum number of bits encoded could be as high as 1000.

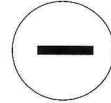
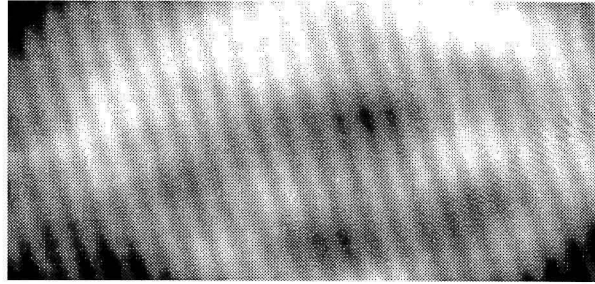
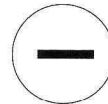
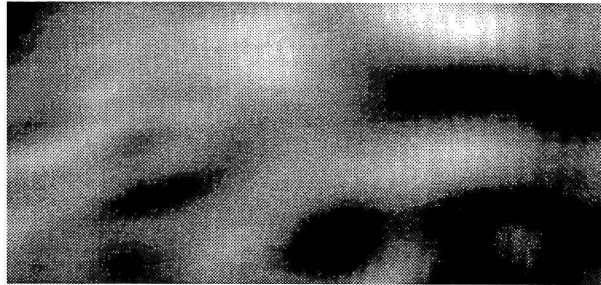
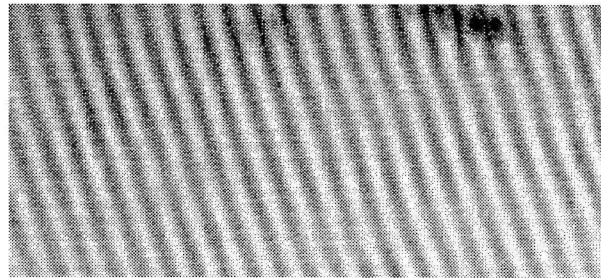
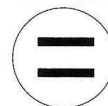
$I(x,y)$

 $I_{dc1}(x,y)$

 $I_{dc2}(x,y)$


Figure 2.43: First order correlation between the probe beam and signal beams. The probe beam and signal beam recombine with a small angle in order to produce a visible fringe pattern on the CCD camera. The DC components are subtracted from the image.

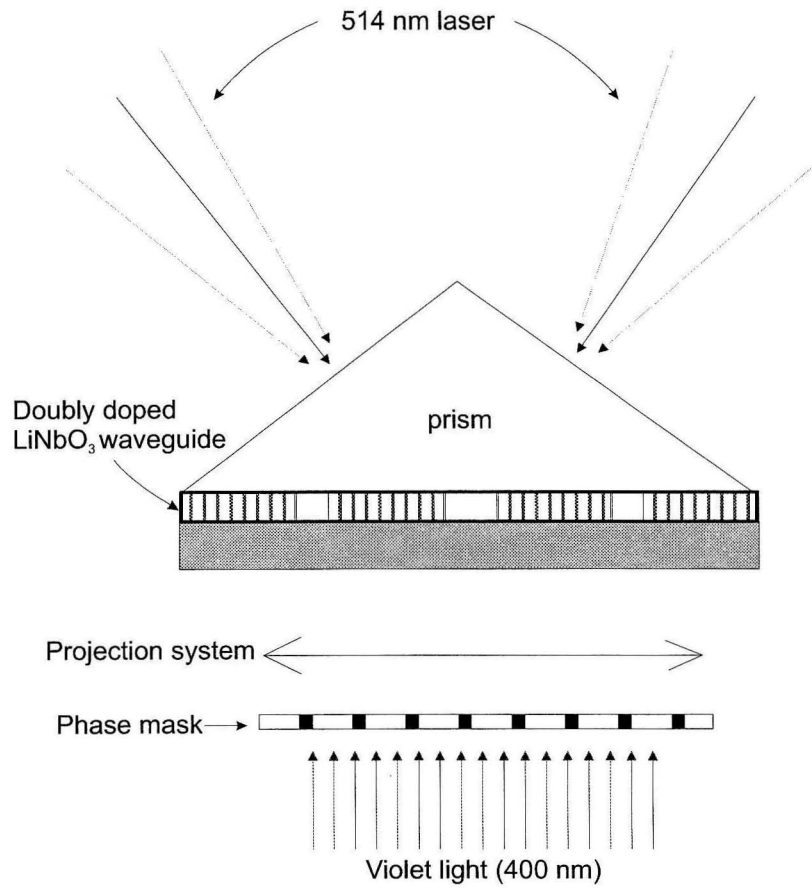


Figure 2.44: Pulse shaping recording system in waveguides. A photolithographic ultra-violet projection system sensitizes the waveguide with sub-micrometer feature size.

Chapter 3 Folded shift multiplexing

3.1 Shift multiplexing

In chapter 2, we used a slab waveguide to confine the signal beam to two dimensions. This allowed us to efficiently utilize the concept of localized recording by minimizing the diffraction effects of the reference beam. In this section, we take the opposite approach: instead of confining the signal beam, a spherical reference beam is confined to two dimensions by the slab waveguide. This implementation leads us to a multiplexing method called folded shift multiplexing that originates from the shift multiplexing method with spherical reference waves in a volume crystal.

We start by reviewing the concept of shift multiplexing [52, 53]. Shift multiplexing is a holographic multiplexing method which uses a spherical reference wave. Holograms are recorded by interfering a spherical reference wave with a signal beam. Multiplexing is achieved by moving the spherical reference beam, or the hologram, with respect to the signal beam. Many holograms can be overlapped tightly, resulting in a high surface density of up to 40 bits/ μm^2 ([2],p.400). Many successful implementations using shift multiplexing in three-dimensional (3-D) disks have been demonstrated in other laboratories [54, 55, 56, 57, 58] and commercially [2]. We extend the shift multiplexing principle to a thin crystal slab. The slab, unlike a volume crystal, acts as a waveguide in one dimension. A spherical wave is coupled to a thin slab, and total internal reflection folds the spherical beam which creates an effective crystal slab thickness that is much larger than the physical slab thickness. As a result, the shift selectivity is that of a volume crystal but with the advantage of a thin physical form factor. However, when multiplexing multiple holograms, the $M_{\#}$ is proportional to the physical slab thickness. We present experimental results to verify the theoretical predictions.

In order to understand the principles of shift multiplexing, we need to describe the

diffraction from volume holograms. A volume hologram is a linear mapping of input plane waves $H_i(\mathbf{k}_i)$ to a set of diffracted plane waves $H_d(\mathbf{k}_d)$. The transfer function of the system $A(\mathbf{k}_i, \mathbf{k}_d)$ determines the strength of the connection between input plane wavevector \mathbf{k}_i and diffracted wavevector \mathbf{k}_d :

$$H_d(\mathbf{k}_d) = \int \int \mathbf{H}_i(\mathbf{k}_i) \mathbf{A}(\mathbf{k}_i, \mathbf{k}_d) d\mathbf{k}_i \quad (3.1)$$

where

$$A(\mathbf{k}_i, \mathbf{k}_d) = \int \int \int \frac{\Delta\epsilon(\mathbf{r}') e^{i(\mathbf{k}_i - \mathbf{k}_d)\mathbf{r}'}}{i2\mathbf{k}_{dz}} d\mathbf{r}' \quad (3.2)$$

$\Delta\epsilon(\mathbf{r}')$ is the perturbation to the dielectric susceptibility of the recording medium. The derivation assumes the Born approximation which requires that the dielectric perturbation be weak, thus only first order terms in $\epsilon(\mathbf{r}')$ are taken into account. Eqn. 3.2 is the three-dimensional Fourier transform of the perturbation (i.e., the hologram). $A(\mathbf{k}_i, \mathbf{k}_d)$ represents the amplitude of the diffracted field propagating in the direction \mathbf{k}_d when the hologram is illuminated by a plane wave incident at direction \mathbf{k}_i . In practice, the integral over $d\mathbf{k}_i$ is simplified greatly by assuming an infinite medium in two dimensions: the direction of the diffracted beam in these two dimensions is then uniquely determined. We illustrate, by an example, how this computation is performed.

A grating is recorded by interfering two plane waves which introduces a perturbation of the dielectric permittivity equal to $\Delta\epsilon(\mathbf{r}') = \Delta\epsilon_0 \text{rect}\left(\frac{z'}{L}\right) e^{jK_g x'}$ (fig. 3.1), where K_g is the inverse of the grating period $K_g = \frac{2\pi}{\Lambda}$. From eqn. 3.2:

$$A(\mathbf{k}_i, \mathbf{k}_d) \propto \int \int \int \text{rect}\left(\frac{z'}{L}\right) e^{jK_g x'} e^{j[(k_{ix} - k_{dx})x' + (k_{iy} - k_{dy})y' + (k_{iz} - k_{dz})z']} dx' dy' dz' \quad (3.3)$$

The integral over x' and y' is taken from $-\infty$ to $+\infty$ and the limit of the integral over z is taken from $-L/2$ to $L/2$. The result of the integration yields:

$$A(\mathbf{k}_i, \mathbf{k}_d) \propto \delta(\mathbf{k}_{ix} - \mathbf{k}_{dx} + \mathbf{K}_g) \delta(\mathbf{k}_{iy} - \mathbf{k}_{dy}) L \text{sinc}\left[\frac{L}{2\pi}(\mathbf{k}_{iz} - \mathbf{k}_{dz})\right] \quad (3.4)$$

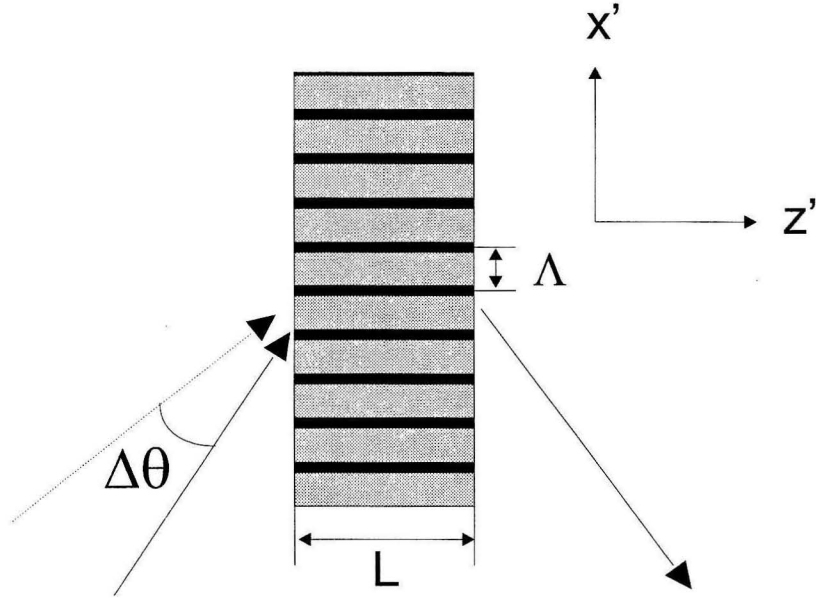


Figure 3.1: Angle multiplexing.

The two delta functions physically mean that the directions of the diffracted field k_{dx} and k_{dy} in the coordinates x' and y' are precisely equal to $k_{ix} + K_g$ and k_{iy} , respectively. The infinite medium in x' and y' allows no other direction of propagation for the diffracted field. However, the medium is limited in the z direction. This creates a continuous range of allowed directions of propagation for the diffracted field in the z coordinate. The span of allowed directions of propagation is expressed as a *sinc* function. Finally, the diffracted field is computed using eqn. 3.1:

$$E_{dx} \propto \text{sinc} \left[\frac{L}{2\pi} (k_{iz} - k_{dz}) \right] \quad (3.5)$$

Angle multiplexing is performed by changing the incident angle of the reference beam in the plane defined by the direction of propagation of the signal and reference beam. The amount of angle change for which the reconstruction of the hologram vanishes defines the angle selectivity. By using the K-sphere diagram illustrated in

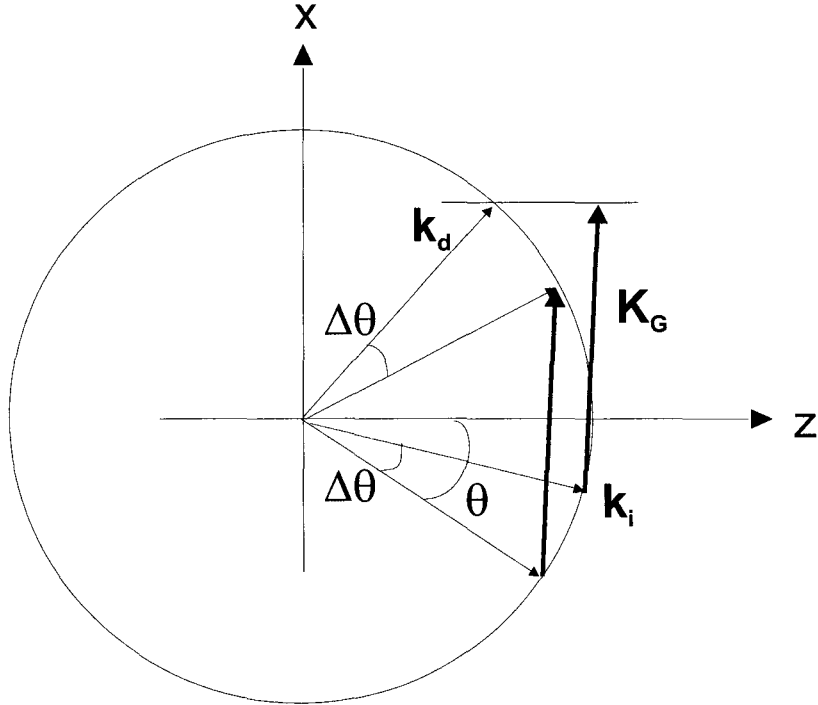


Figure 3.2: K-sphere representation.

fig. 3.2, the angle selectivity can be computed easily:

$$\begin{aligned}
 k_{iz} &= k \cos(\theta - \Delta\theta) \simeq k \cos\theta + k \sin\theta \Delta\theta. \\
 k_{dz} &= k \cos(\theta + \Delta\theta) \simeq k \cos\theta - k \sin\theta \Delta\theta. \\
 k_{iz} - k_{dz} &= 2k \sin\theta \Delta\theta.
 \end{aligned} \tag{3.6}$$

Therefore, the diffracted field depends on the angle of the incident beam as:

$$E_{dx} \propto \text{sinc} \left[\frac{2L}{\lambda} \sin\theta \Delta\theta \right] \tag{3.7}$$

The angle selectivity computed from eqn. 3.7 is shown in fig. 3.3. Up to 5000 holograms have been stored in one location using angle multiplexing [59].

For shift multiplexing, the plane wave reference beam is replaced with a spherical reference wave. Figure 3.4 (a) illustrates the 90-degree geometry shift multiplexing.

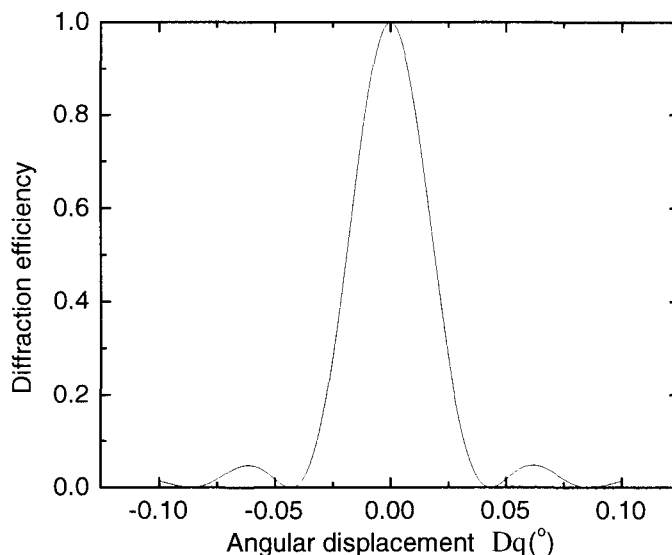


Figure 3.3: Numerical computation of the diffraction efficiency as a function of the incident beam angle.

The spherical wave is generated from a point source on the left side of the crystal and interferes with a plane wave signal beam coming from the top of the crystal. When the reference spherical beam is shifted along the y direction, the reconstruction vanishes after some shift distance called the shift selectivity. A simple geometrical explanation that yields the correct shift selectivity uses the concept of light rays and angle selectivity. A spherical wave reaches the far field condition after a very short distance: the condition for far field approximation requires that $z > x^2/\lambda$, where x is the transverse dimension of the field at the input plane. For a tightly focused beam x is on the order of a few micrometers; therefore, the far field condition is reached after only a few tens of micrometers. The far field of an input distribution can be represented as a Fourier integral. This means that a point in space is the result of the contribution of one unique infinite plane wave. For a spherical wave, this means that the direction of an optical ray emanating from the focus can be thought of as an infinite plane wave propagating in the same direction which has a constructive

contribution only along the ray. When the spherical reference wave is shifted by δ in the y direction, the hologram becomes angle-Bragg-mismatched locally. The angle selectivity in the 90-degree geometry is equal to:

$$\Delta\theta = \frac{\lambda}{L} \quad (3.8)$$

If z_o is the distance from the spherical wave focus and the hologram location, the angle change at the hologram location is:

$$\Delta\theta = \frac{\delta}{z_o} \quad (3.9)$$

Combining eqn. 3.8 and 3.9, the shift selectivity is given by:

$$\delta = \lambda \frac{z_o}{L} \quad (3.10)$$

This result assumes that the angle selectivity does not vary across the length L of the crystal. A more rigorous approach includes a 3-D analytical integration using the paraxial approximation for the spherical wave. The shift selectivity obtained is the same as in eqn. 3.10 . The derivation is described in [60].

3.2 Folded shift multiplexing

In this section, we present the derivation of the shift selectivity with a slab waveguide and present experimental results to support the theory.

The thick crystal of fig. 3.4 (a) is replaced by a thin crystal slab (fig. 3.4 (b)). The spherical wave is trapped in the y dimension inside the crystal by total internal reflection. A cylindrical lens can be used to confine the beam in the x direction.

We assume that the thickness D of the slab is much larger than the wavelength of light so that the assumption of a continuum of modes is valid. Under this assumption, the wave inside the slab is still cylindrical but folded. A point P in the crystal slab (fig. 3.5) is at the intersection of many rays, each having a different phase due to their

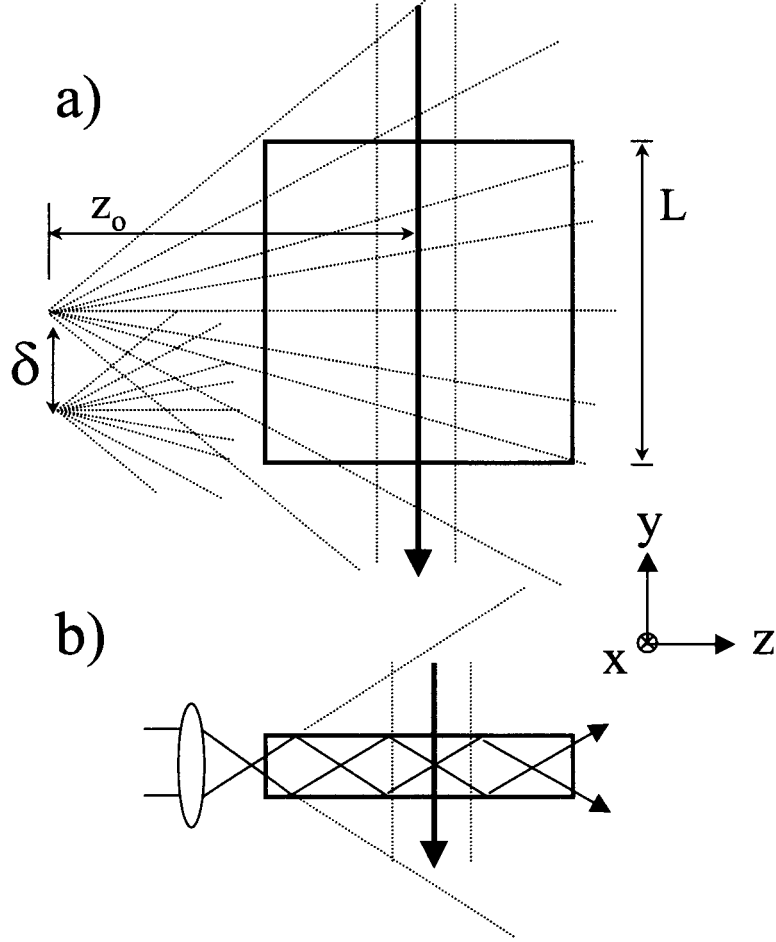


Figure 3.4: (a) Shift multiplexing in the 90-degree geometry; (b) Shift multiplexing by total internal reflection in a crystal slab.

respective different paths. The multiple rays intersecting at point P due to folding is equivalent to an unfolded wave extended beyond the crystal thickness as shown in figure 3.4 (b). The reference wave inside the slab can thus be described by:

$$R(x, z) = \frac{1}{j\lambda z} \exp\left(j 2\pi \frac{z}{\lambda}\right) \exp\left(j\pi \frac{y^2}{\lambda z}\right) \quad (3.11)$$

Another term needs to be added to eqn. 3.11 which takes into account the phase shift ϕ caused by total internal reflection of the rays in the dielectric material. The phase shift ϕ is angle dependent and given by [62, 63]:

$$\tan\left(\frac{\phi}{2}\right) = \left(\frac{\sin^2 \theta_c}{\sin^2 \theta} - 1\right)^{\frac{1}{2}} \quad (3.12)$$

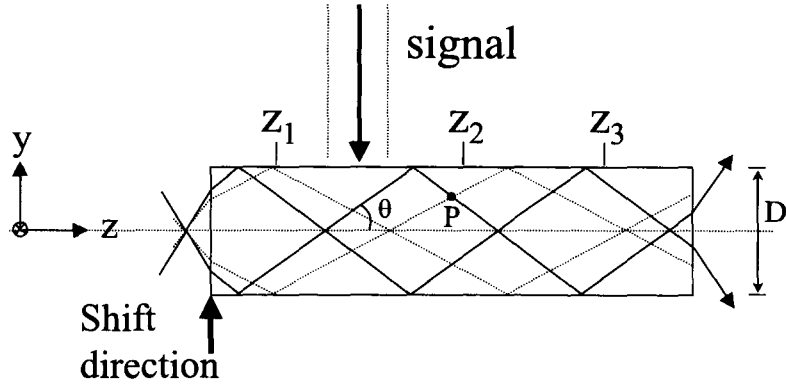


Figure 3.5: Recording geometry and notation.

where θ_c is the critical angle equal to $asin\sqrt{1 - \left(\frac{n_1}{n_2}\right)^2}$ with n_2 and n_1 being refractive indices inside and outside the slab, respectively. For small divergence angles θ , the distance between total internal reflection in the z direction is equal to $\frac{D}{\theta}$. After a propagation distance z , the total phase accumulated becomes:

$$\Phi(\theta) = \frac{z}{\frac{D}{\theta}} \phi(\theta) \quad (3.13)$$

Using eqns. 3.12 and 3.13, the reference wave 3.11 can be written, using the paraxial approximation and neglecting third orders in $\theta = \frac{y}{z}$, as:

$$R(x, z) = \frac{1}{j\lambda z} \exp\left(j2\pi\frac{z}{\lambda}\right) \exp\left(j\pi\frac{y^2}{\lambda z} \left[1 - \frac{2\lambda}{\pi D \sin\theta_c}\right]\right) \exp\left(j\pi\frac{y}{D}\right) \quad (3.14)$$

The wavelength λ is much smaller than the thickness D of the slab so that the term in the bracket of eqn. 3.14 approaches unity. The effective difference between the cylindrical wave propagating in the slab and the cylindrical wave propagating in a thick crystal is the phase term $(\pi y/D)$. The latter phase term does not contribute to the shift selectivity.

The unfolded wavefront can be visualized numerically by propagating a cylindrical wave inside a crystal slab. The phase shift to be added upon reflection is computed using eqn. 3.12. In the simulation, we chose a numerical aperture equal to $N.A = 0.5$, a crystal slab thickness of 1mm and length of 20 mm. The propagating medium is

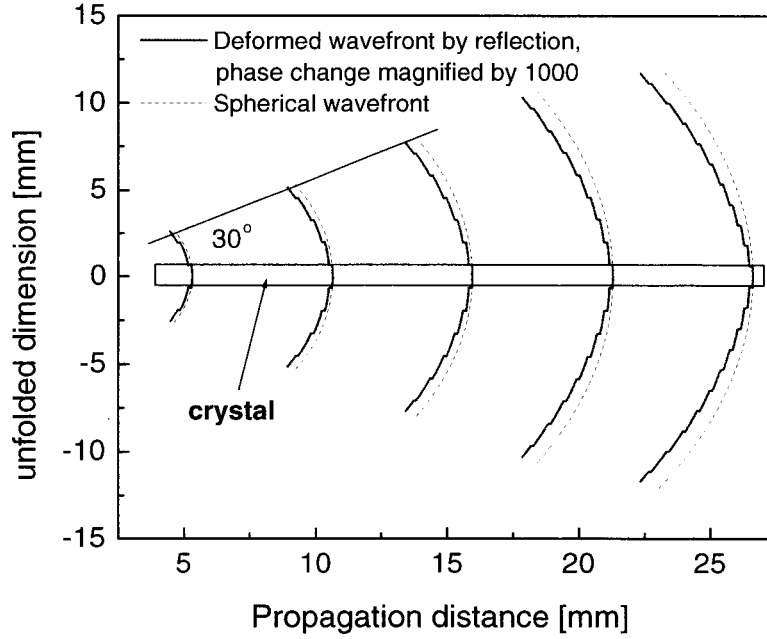


Figure 3.6: Wavefront versus propagation distance in the slab. The dashed curve represents a perfect spherical wavefront and the plain curve represent the wavefront unfolded from total internal reflection in the slab. The phase change after reflection is magnified by 1000 to note the deformation.

LiNbO₃ and the wavelength of light is 532 nm. There is no noticeable difference between a cylindrical wavefront and the unfolded wavefront propagating in the slab. When the phase shift is artificially magnified by 1000, the effects of phase shift upon reflection can be seen in fig. 3.6. The phase shift's effects due to total internal reflection are thus negligible; therefore, the shift selectivity for a cylindrical beam coupled in a crystal slab is equal to:

$$\delta = \frac{\lambda}{2N.A}, \quad (3.15)$$

where $N.A$ is the numerical aperture of the spherical beam (z_o/L) and λ is the wavelength of light in vacuum.

A particularly interesting result from the shift selectivity is that it does not depend

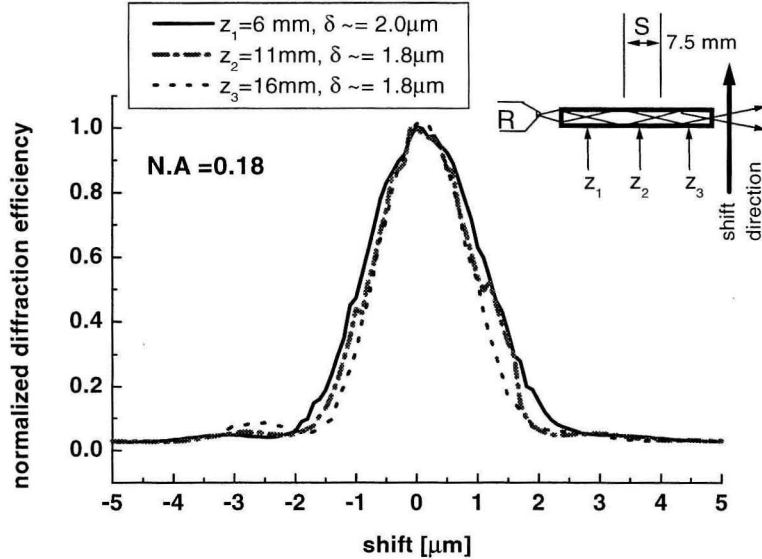


Figure 3.7: Shift selectivity for different locations z_i ($i=1,2,3$) along the slab. Numerical aperture (N.A) of the reference wave is 0.18.

on the location z of the hologram inside the slab or on the slab thickness D . We performed experiments in a LiNbO_3 crystal doped with 0.1% FeO_2 . The crystal dimensions are $1 \times 20 \times 15$ mm³; it is cut for 90 degree geometry. The reference beam is generated by focusing light from a green cw laser (wavelength 532nm, ordinary polarization) with a microscope objective onto the crystal's 1 mm facet. The signal beam is a plane wave perpendicular to the (y, z) plane with diameter 7.5 mm, as illustrated in fig. 3.5. Fig. 3.7 shows the selectivity curves for different locations z_i ($i=1,2,3$) of the holograms along the slab. The shift selectivity is independent of the location z_i as predicted from eqn. 3.15. With $\text{N.A}=0.18$ outside the crystal and $\lambda = 0.532 \mu\text{m}$, eqn. 3.15 gives $\delta = 1.5 \mu\text{m}$ which is close to the experimental value of $1.8 \mu\text{m}$. Fig. 3.8 shows the results for a numerical aperture of 0.65. Again, shift selectivity is independent of the hologram location and slab thickness. Theoretical and experimental values agree very well ($0.41 \mu\text{m}$ vs. $0.5 \mu\text{m}$, respectively).

Focusing the reference wave close to the slab's entrance facet allows us to store multiple holograms by shifting the reference wave in a direction parallel to the slab facet. We performed an experiment where 50 images of random bit patterns are

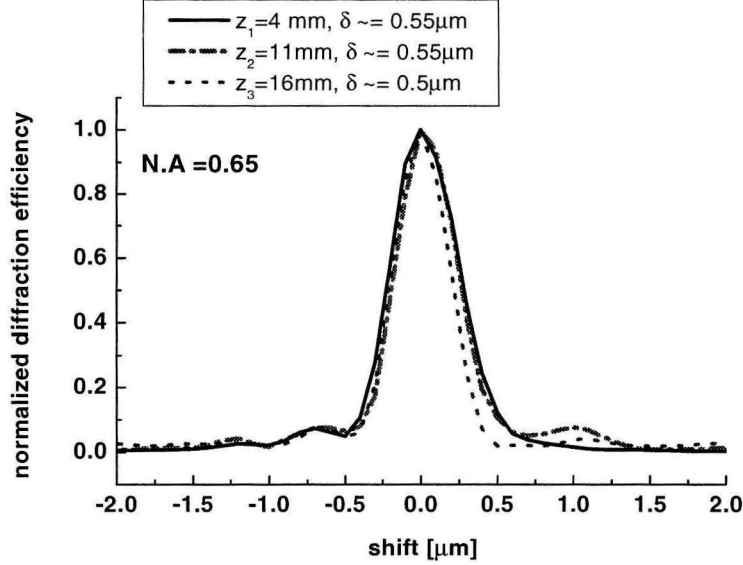


Figure 3.8: Shift selectivity for different locations z_i ($i=1,2,3$) along the slab. Numerical aperture (N.A) of the reference wave is 0.65.

multiplexed by shifting the spherical wave in the y direction. Fig. 3.9 illustrates the experimental set-up. An objective lens with N.A=0.65 generates the spherical wave, which is coupled into the slab crystal as shown in fig. 3.5. The SLM is imaged with a 4-f system onto the camera. The crystal is placed in the Fresnel region of the first imaging lens. The diameter of the signal beam at the crystal was 3mm. The result of the 50 holograms experiment is shown in fig. 3.10. Each hologram is recorded by shifting the crystal in the y direction by $5\mu\text{m}$. Fig. 3.10 shows the diffraction efficiency versus the crystal shift in the y direction. Figs. 3.11 (a) and 3.11 (b) show the random bit pattern imaged through the crystal slab and a holographic reconstruction of image #20, respectively. SNR of 3.5 is measured for the reconstruction. Because the crystal slab is not coated, multiple reflections of the signal beam off the crystal facets yield a non-uniform image intensity.

The diffraction efficiency of fig. 3.10 is computed using the ratio between diffracted power and incident power. Because the ratio of the reference area to the signal area at the overlap is equal to $1/3$, the diffraction efficiency computed as a ratio of intensities is simply found by dividing the values of fig. 3.10 by 3. This allows us to compare

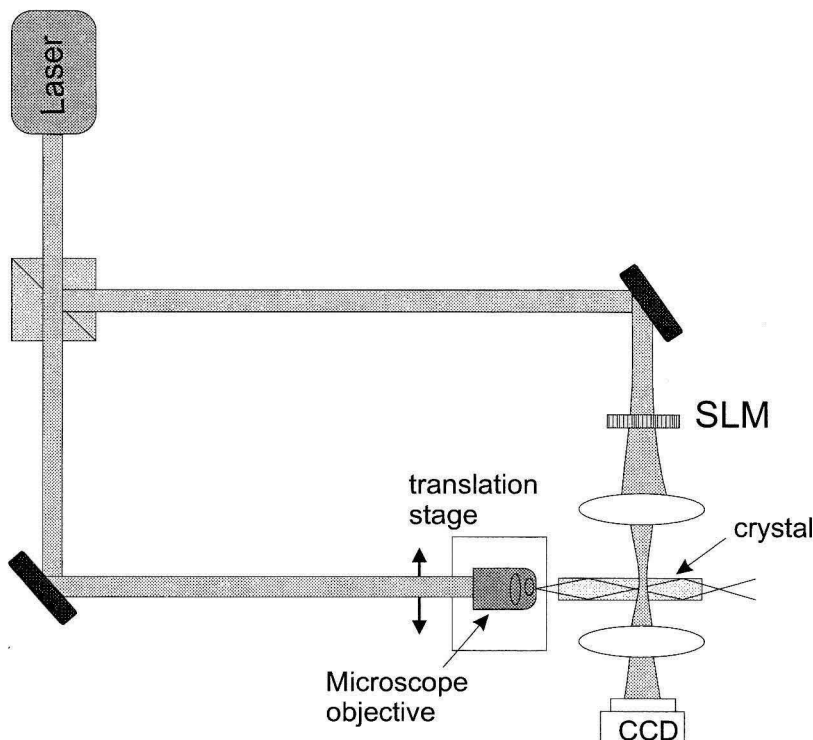


Figure 3.9: Set-up for the shift multiplexed 50 holograms.

the $M_{\#}$ obtained in this experiment with the $M_{\#}$ obtained by others in the literature. We find that the $M_{\#}$ is equal to 0.96 for a thickness of 1 mm, which means that for a 1 cm crystal thickness the $M_{\#}$ would be equal to $\simeq 10$. These values of $M_{\#}$ are unusually high for LiNbO_3 . We attribute this effect to the good uniformity of the reference beam trapped inside the slab. The reference beam uniformity produces a homogeneous optimal modulation depth which is otherwise hard to achieve with an expanded spherical wave in a thick crystal. Memory capacity can be increased by introducing wavelength multiplexing [23, 61] and spatial multiplexing by recording non-overlapping holograms along the length of the crystal: the latter is a unique property of the folded shift multiplexing approach, because the beam remains trapped in the slab. We can extrapolate the number of holograms that can be recorded using the set-up of fig. 3.9: the number of spatially non-overlapping sites in the crystal is approximately equal to 10 in a 30 mm long crystal. Assuming 50 shift multiplexed holograms per location multiplied by a factor of 10 using wavelength multiplexing, a total number of 5000 holograms can be recorded in a $30 \times 5 \times 1\text{mm}^3$ slab. If a diffuser

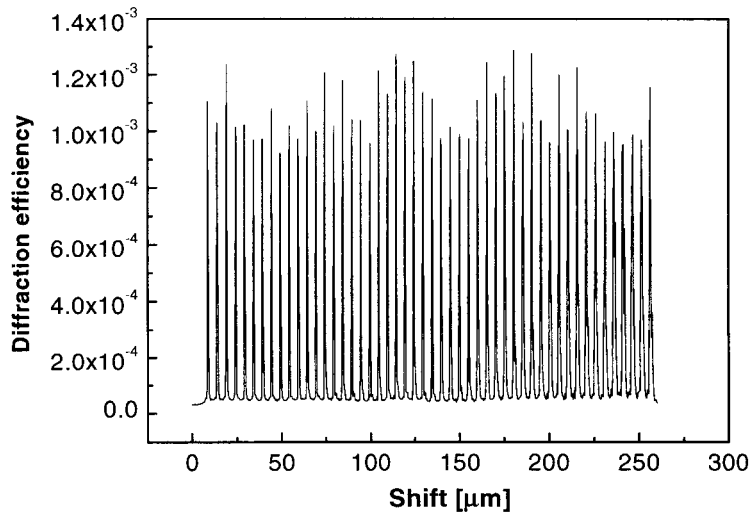


Figure 3.10: Read-out of 50 shift multiplexed holograms in the slab crystal.

is placed in front of the crystal facet, the selectivity in the degenerate x direction becomes much smaller than if no diffuser was present. This is due to the speckle effect [64, 65, 66]. The shift selectivity in the degenerate direction is equal to the size of a speckle grain which is on the order of a few micrometers.

A read-only memory can be implemented with no moving parts by placing an array of VCSELs (Vertical Cavity Surface Emitting Laser) or edge emitting semi-conductor lasers close to the crystal surface. A diffuser is placed in front of the recording material for two reasons. The first reason is that the light emitted from the VCSEL array has low divergence; and thus, the diffuser increases the emission angle. The second reason for using a diffuser is to increase the shift selectivity in the degenerate direction. Referring to fig. 3.12, the divergence angle inside the material is set to $\alpha = 47^\circ$. This angle corresponds to an external numerical aperture of $N.A = 0.6$, computed with an index of refraction of 1.5 (a polymer for example). The VCSEL array contains 1000 lasers laid out on a grid of 50×10 . The two VCSEL arrays are facing each other. The center to center spacing between the lasers is typically $100 \mu\text{m}$. The size of the laser array is then $H_{vc} = 5 \text{ mm}$, $D_{vc} = 1 \text{ mm}$. The detector arrays each contain 1000×1000 pixels of size $5 \times 5 \mu\text{m}^2$. The detector size becomes $5 \times 5 \text{ mm}$

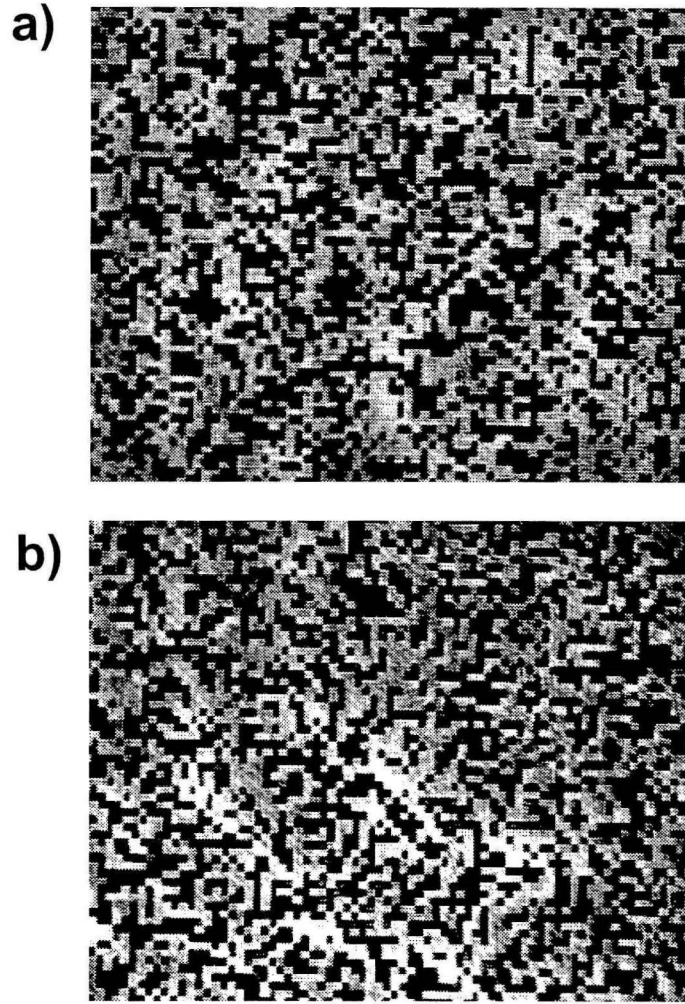


Figure 3.11: a) Pattern imaged through the crystal slab. b) Sample reconstruction of hologram #20.

assuming a 100% fill factor. The thickness of the recording medium is $T_y = 1.5$ mm. The hologram area in the material has roughly the same area as the detector because the detector array is placed against the bottom surface of the medium. The minimum distance L_b , between the laser array and the first detector array, necessary to obtain coverage of the hologram by each laser is equal to:

$$L_b = \frac{H_{vc}/2 + b/2}{\tan 20^\circ} = 11.5 \text{ mm}. \quad (3.16)$$

The lateral dimension T_x can be on the order of VCSEL array's size H_{vc} . In this case, the light is confined in both dimensions which yields a uniform intensity along

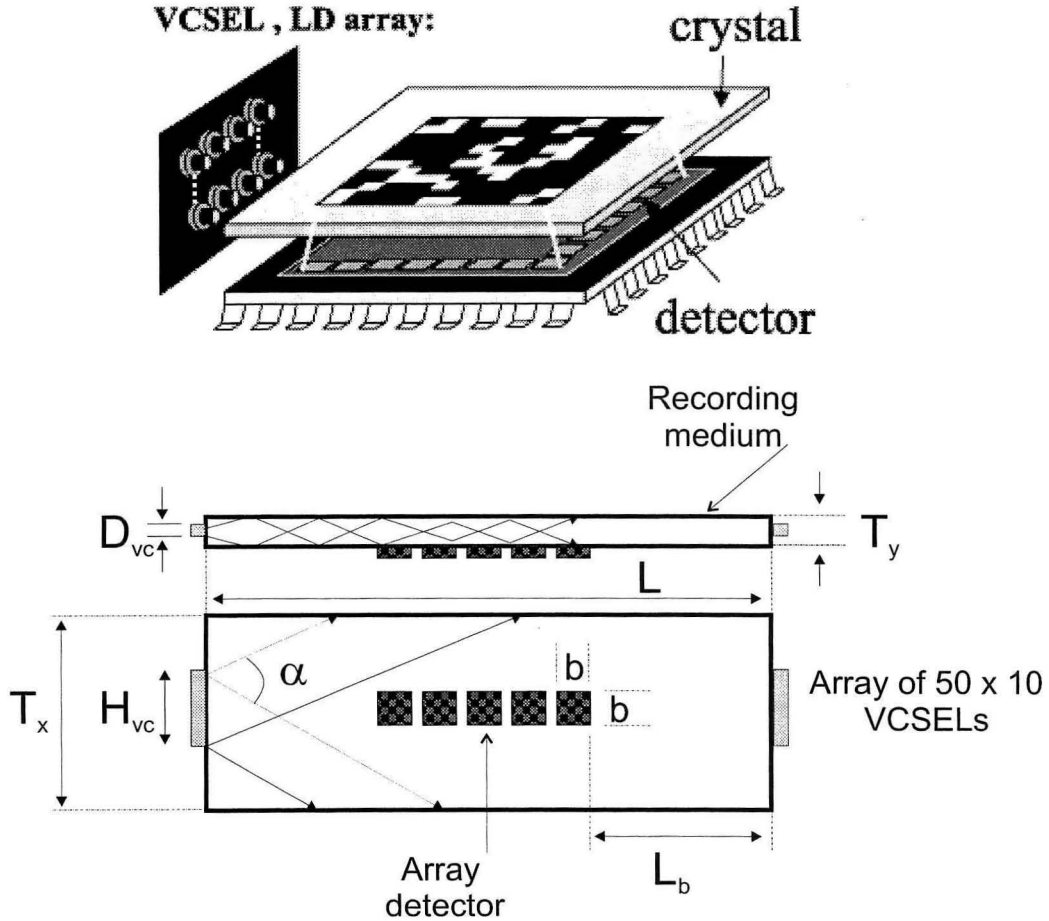


Figure 3.12: Implementation of a read-only memory based on folded shift multiplexing in thin slabs.

the medium length L . Five array detectors are placed against the recording medium to increase capacity and read-out rate. The total length of the recording material L is then equal to 53 mm. Each laser reconstructs only one hologram so that the total number of holograms stored in the memory is equal to the number of lasers (1000). Each page contains 10^6 bits which results in a total capacity of 1 Gbit. The read-out rate is computed as follows: we assume that $N = 1000$ photons are required to achieve an acceptable Signal to Noise Ratio (SNR). The diffraction efficiency of the hologram is equal to $\eta = (M/\# / M)^2$, where M is the number of holograms, and $M/\#$ is the M-number of the medium. In the implementation of fig. 3.12, the number of holograms corresponding to each detector array is equal to $1000/5 = 200$. From the

measurement of $M/\#$ in the experiment described above, we choose $M/\#=1/\text{mm}$. Assuming the read-out light is monochromatic of frequency ν , the number of photons received per pixel N_p per unit time is equal to:

$$N_p = \frac{\left(\frac{M/\#}{M}\right)^2 I_{read} A_{pixel}}{h \nu} \quad (3.17)$$

where h is Planck's constant. If we further assume that the detector converts one photon to one electron, the integration time t_{int} required to obtain N_e electrons per pixel at the detector is:

$$t_{int} = \frac{N_e}{N_p} = \frac{M^2 N h \nu N^2}{M^2/\# I_{read} A} \quad (3.18)$$

where N is the number of bits per hologram (10^6), and A is the detector size (b^2). The read-out rate B_r is equal to the number of pages that can be read-out per second:

$$B_r = \frac{N}{t_{int}} = \frac{M^2/\# I_{read} A}{M^2 h \nu} \quad (3.19)$$

The power available from laser in a VCSEL array is in the 1 mW range. The absorption of the material at the read-out wavelength is assumed to be $\alpha=0.5/\text{cm}$. The power decays exponentially inside the medium as:

$$P_L = P_{in} e^{-\alpha \cdot L} \quad (3.20)$$

where P_{L_b} is the power after a propagation distance L when the input power is equal to P_{in} . Taking $L = 20$ mm, the power decreases by a factor of 2.7. The read-out intensity is thus equal to $P_L/H_{vc} \cdot b = 370\mu\text{W}/(5\text{ mm} \cdot 5\text{ mm})=1.5$ mW/cm². The read-out rate per detector computed from eqn. 3.19 is equal to 0.5 Gbit/s. With the parallelism of five detectors, the total read-out rate of the memory is $B_r = 2.5$ Gbit/s. The turn on-off time of a VCSEL is on the order of 1-2 nanoseconds, much smaller than the integration time of 2 ms. This memory is a powerful read-only thin flash

card that could be used for example in Optical Field Programmable Arrays as a mean for optically reconfiguring the processing hardware.

Chapter 4 Spectral hole-burning in naphthalocyanine derivatives in the 800 nm region for holographic storage applications

4.1 Introduction

In conventional holographic memories, many holograms are superimposed in the volume of the material using Bragg mismatching effects. Here, we use a radically different concept for multiplexing holograms. Spectral Hole Burning (SHB) in spectrally sensitive materials is a method that is wavelength selective. Unlike wavelength multiplexing which relies on Bragg mismatching effects, SHB is based on frequency selective absorption of molecules or ions embedded in an amorphous or solid matrix. The attractive feature of SHB is the outstanding frequency selectivity of the hologram which is many orders of magnitude smaller than the wavelength-Bragg selectivity. The number of frequency channels can be up to 10^8 and is determined by the properties of the material. By combining this very large frequency multiplicity and holography, the storage density could achieve ultra high densities up to $100 \text{ kbits}/\mu\text{m}^2$.

To illustrate the extreme wavelength sensitivity in SHB materials, we compare it to the conventional wavelength selectivity that is based on Bragg mismatching effects. Let us consider a hologram written with two monochromatic beams interfering in a material. The amount of wavelength shift necessary to Bragg mismatch the hologram is equal to:

$$(\Delta\lambda)_B = \frac{\lambda^2 \cos \theta_s}{2L \sin \frac{\theta_r + \theta_s}{2}} \quad (4.1)$$

where θ_r and θ_s are the angles of the reference and signal beams with respect to the normal of the material. L is the thickness of the medium and λ is the wavelength of light. For a material thickness of $L = 0.5$ mm, wavelength of 532 nm and angles $\theta_r = \theta_s = 20$ degrees, the wavelength selectivity computed from eqn. 4.1 is equal to $\Delta\lambda = 2.28$ nm or $\Delta\nu = 2,416$ GHz in frequency. Given that the maximum tuning range of commercial tunable laser sources is approximately 20 nm, the number of independent wavelength channels is very few. The typical wavelength selectivity of spectral hole burning organic materials is on the order of hundreds of MHz, which is four orders of magnitude smaller than conventional wavelength-bragg selectivity.

Spectral hole burning relies on the extremely narrow spectral lines occurring in many optical transitions of chromophores embedded in solid matrices and cooled down to a few degrees Kelvin. The width of these transitions called zero phonon lines are very narrow. For ions in inorganic crystals, the linewidth can be a few kilohertz, while for organic chromophores embedded in a polymer host matrix, the linewidth is hundreds of MHz. Such optical transitions are extremely sensitive to all types of perturbations and a spread of the transition frequencies reflects the fluctuations in the local environments of the individual molecules and leads to inhomogeneously broadened lines. The homogeneous and inhomogeneous broadening is illustrated in fig. 4.1. The number of frequency channels available is determined by the ratio of the inhomogeneous and homogeneous linewidths. At low temperatures (<4 degrees Kelvin) this ratio can be as high as 10^8 . At higher temperatures (20 degrees Kelvin), this ratio decreases to only a few channels because the homogeneous linewidth is strongly dependent on temperature. Recently, the recording of 12,000 holograms in one spatial location using frequency multiplexing around 634 nm has been demonstrated in chlorine doped polyvinyl butyral films [71]. To access holograms stored in the medium, the laser source is tuned to the corresponding wavelength used to record the hologram. The laser frequency tunability has to match the inhomogeneous linewidth of the material, which is typically 10 THz (corresponding to 21 nm at a wavelength of 800 nm) for polymer-based materials. The accuracy and repeatability of the laser source must be less than the homogeneous linewidth: for polymers at

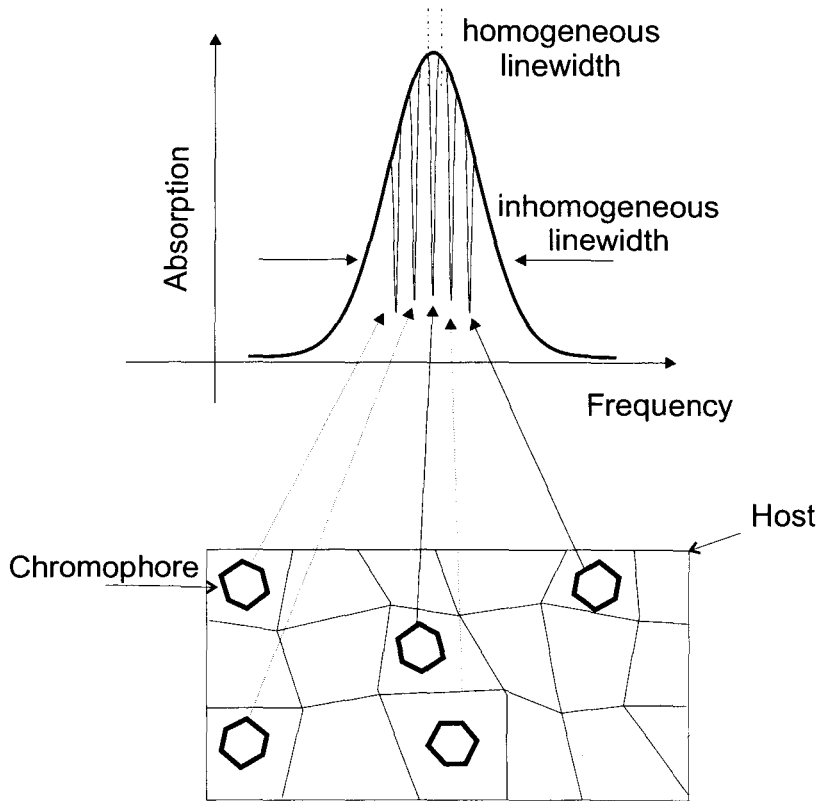


Figure 4.1: Wavelength selective absorption by chromophores embedded in a polymer host. The optical transition of the chromophores depends on the local surrounding environment.

4.2 K the homogeneous linewidth is less than or approximately 1 GHz. Fast tuning between frequency channels is required for fast access time.

The hologram recording mechanism, in wavelength selective materials, is based on absorption differences generated after exposure between bright and dark regions of the interference pattern. In bright regions of the interference pattern, chromophores, tuned to the light frequency, absorb light and undergo a photochemical or photophysical transformation. The chromophores that result from the transformation do not absorb the same light frequency and therefore become transparent. The interference pattern between a reference and a signal beam is imprinted as a modulation of the absorption coefficient rather than a modulation of the index of refraction. By using the formalism of coupled-wave equations, the diffraction efficiency of pure absorption

holograms is given by:

$$(\eta(\nu))_{abs} = \exp\left(-\frac{2\alpha_o(\nu)d}{\cos\theta}\right) \left(\frac{\alpha_1(\nu)d}{2\cos\theta}\right)^2 \quad (4.2)$$

where d is the thickness of the material, α_o is the absorption coefficient and α_1 is the absorption modulation of the hologram. The maximum diffraction efficiency is realized when the absorption modulation is maximal $\alpha_1 = \alpha_o$ and when the quantity $\alpha_o \cdot d/2 \cos\theta = 0.55$. With these values, the maximum diffraction efficiency of a pure absorption hologram in the transmission geometry is equal to 3.7%.

A modulation of the absorption coefficient $\alpha_1(\nu)$ induces a modulation of the refractive index modulation $n_1(\nu)$. The absorption and index modulations are proportional to the real and imaginary parts of the absorption coefficient, respectively. The optical field is thus diffracted by both an absorption grating and an index grating as shown in fig. 4.2.

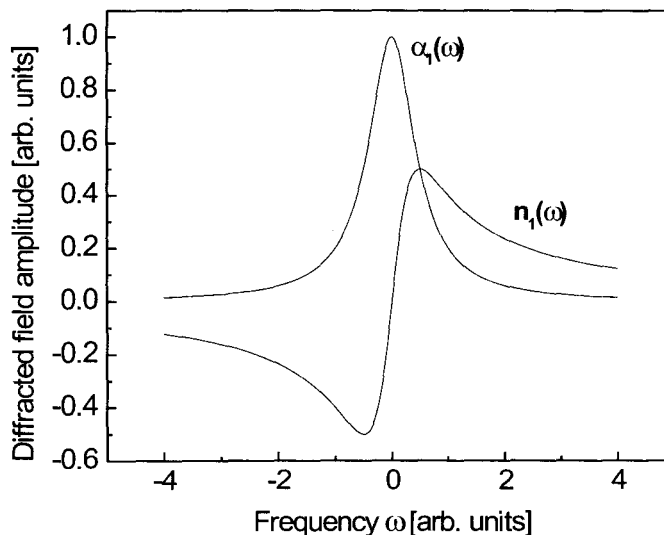


Figure 4.2: Diffracted field from an absorption grating $\alpha_1(\omega)$ and the corresponding index of refraction $n_1(\omega)$ grating obtained from the Krmaers-Kronig relation.

An absorption hologram can be transformed into a pure index hologram by uti-

lizing the properties of diffraction illustrated in fig. 4.2 [83, 84]. By transforming an absorption modulation to an index modulation, the diffraction efficiency can be increased from the maximum theoretical value of a pure absorption grating (3.7%). A diffraction efficiency of 4.8% has been reported for induced refractive index holograms [84].

In section 4.2, we report on an investigation of the spectral and hole burning properties of five commercially available free-based metallo-naphthalocyanines in two polymer hosts and their application for high fidelity holography. These materials exhibit a strong 0-0 absorption band in the 800 nm region. In the infrared region (IR), laser sources such as distributed feedback lasers are commercially available. These laser diodes are excellent sources for polymers sensitive in the IR, because they provide good stability and repeatability ($\ll 1$ GHz) and fast tuning speed (5 ns for current tuning). The IR region matches the tuning range of Ti-Sapphire lasers as well.

Metallo-naphthalocyanines demonstrate a non-photochemical hole-burning mechanism that is likely related to rotations of small molecular groups attached to a relatively rigid molecular ring. Free-base molecules exhibit the regular proton phototautomerisation mechanism of hole burning. Spectral and hole burning parameters were determined for eight materials. In particular, the hole burning kinetics were analyzed and the quantum efficiencies were determined to be between 0.1% and 1%. Holograms (data pages) in the transmission geometry were successfully recorded in the materials studied using single frequency laser diodes.

In section 4.3, we theoretically investigate the multiplexing of many absorption holograms at a single frequency and location. We analyze the inter-play between absorption and index grating and their influence on the diffraction efficiency of many superimposed holograms. The major result is that the $M/\#$ is on the order of 0.05 and that the transformation to an index grating does not increase significantly the $M/\#$.

4.2 Material preparation

Porphyrin and phthalocyanine derivatives in polymer hosts have been extensively studied as potential materials for frequency- and time-domain spectral hole-burning optical storage. These materials exhibit S_0-S_1 0-0 absorption bands in the red wavelength region (610 -700 nm), large inhomogeneous broadening and relatively narrow holes at low temperatures, and a built-in proton phototransformation mechanism between different tautomers in free-base compounds. More complex alternatives to porphyrins and phthalocyanines are naphthalocyanines. Due to the increase in size of their skeleton and p-electron system, these molecules have 0-0 absorption patterns shifted towards the infrared.

The samples under investigation were five naphthalocyanines derivatives: 2,11,20,29-tetra-tert-butyl-2,3-naphthalocyanine (H_2 -TBNP), 1,4,8,11,15,18,22,25- octabutoxy-2,3-naphthalocyanine (H_2 -OBNP), zinc 2,11,20,29-tetra-tert-butyl-2,3-naphthalocyanine (Zn-TBNP), nickel 2,11,20,29-tetra-tert-butyl-2,3-naphthalocyanine (Ni-TBNP), and silicon 2,3- naphthalocyanine dioctyloxide (Si-NPDO). The chemical structures of these chromophores are represented in fig. 4.3

To prepare the samples we used two types of host matrices: polyvinyl butyral (PVB) to produce samples with thicknesses in the range of 100 to 400 μm , and polystyrene (PS) to produce samples with thickness larger than 1 mm. The doping concentration was between 10^{-3} mol/l and 10^{-5} mol/l. Samples with good optical quality were prepared as follows. The dopants were purchased in powder form from Sigma-Aldrich [79] and without further purification diluted in acetone. After evaporation, the PVB powder was mixed with the diluted dopant in dichloromethane. The mixture was left to evaporate for 2 days in a Petri dish. The resulting thin films were then pressed against a polished metal plate at 75 degrees Celsius to achieve good optical quality. To prepare polystyrene samples, the dopant powder was mixed with purified styrene in a Pyrex container. The container was then cooled in liquid nitrogen and vacuum pumped to remove the oxygen. The container is then heated in hot water. The cycle is repeated four times. The Pyrex container is then sealed and

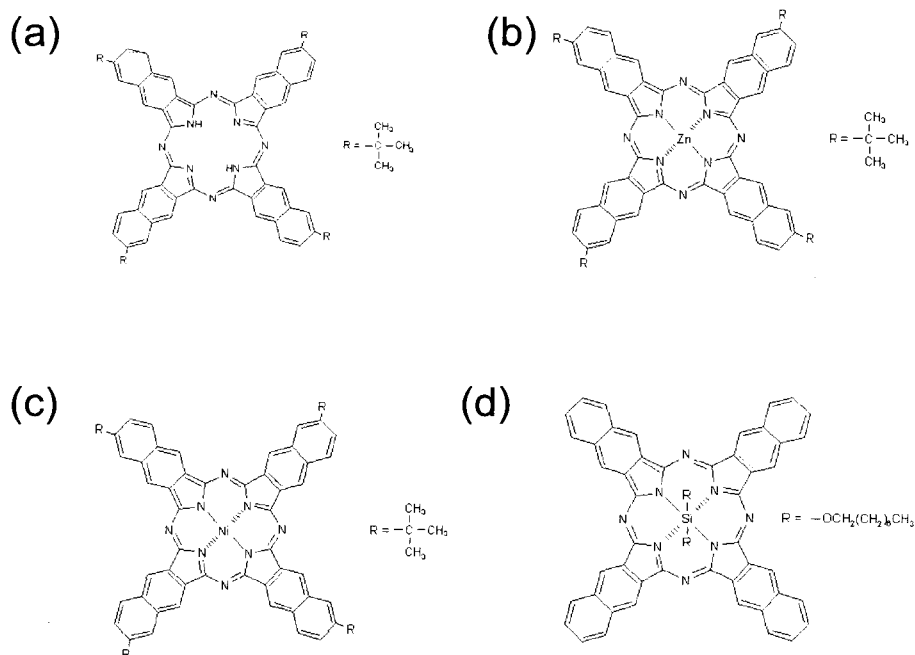


Figure 4.3: Chemical structures of four chromophores. (a) 2,11,20,29-tetra-tert-butyl-2,3-naphthalocyanine (H₂-TBNP). (b) zinc 2,11,20,29-tetra-tert-butyl-2,3-naphthalocyanine (Zn-TBNP). (c) nickel 2,11,20,29-tetra-tert-butyl-2,3-naphthalocyanine (Ni-TBNP). (d) silicon 2,3-naphthalocyanine dioctyloxy (Si-NPDO).

left at 100 degrees Celsius for two days for polymerization.

4.2.1 Hole burning properties

Absorption spectra of the several representative materials at 8 K in the region of the S₁-S₀ transition are shown in fig. 4.4. All materials studied have the intense 0-0 band located around 790 nm. Some impurities, particularly H₂-TBNP, display strong signs of aggregation at concentrations higher than 10⁻⁴ mol/l as can be seen by comparing figs. 4.4 (a) and (b). Spectral holes were burned in the 0-0 absorption band and detected in transmission by a single frequency tunable Ti: Sapphire laser with a linewidth less than 1 MHz at a temperature of 1.5 K. To avoid power saturation, low burning intensities between 10 and 200 mW/cm² were selected. Additionally, for hole detection the intensity was reduced by two orders of magnitude. To compare

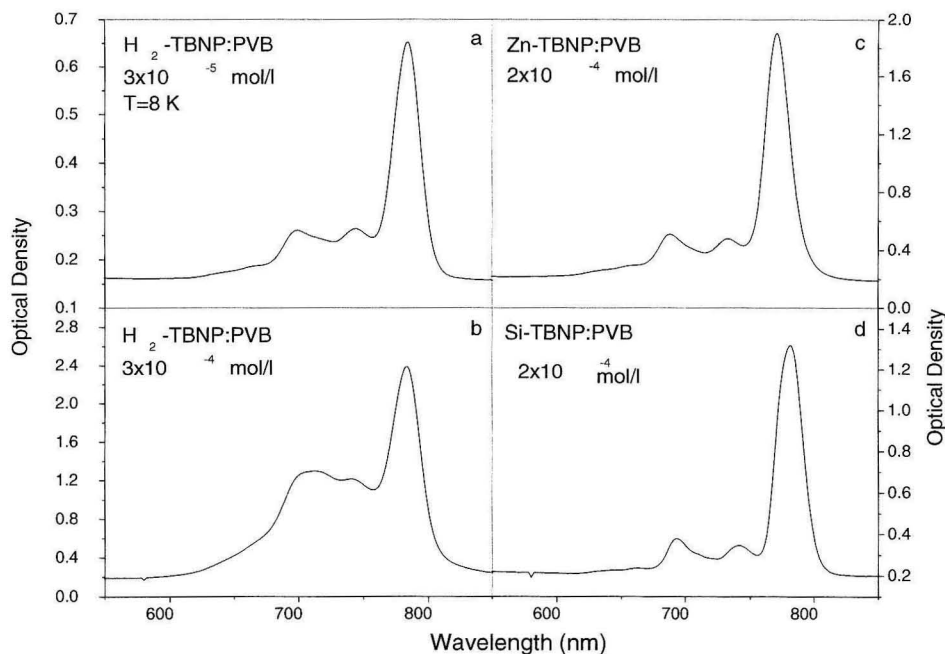


Figure 4.4: Absorption spectra of several naphthalocyanines at 8 K.

different samples, the burning wavelength was chosen to have an initial optical density in all cases of about 0.7. The normalized hole spectra at different exposures for Zn-TBNP/PVB are shown in fig. 4.5.

Hole broadening due to the exposure saturation is clearly seen. The minimal holewidth tabulated in Table 4.2.1 was found by extrapolation of the holewidth dependence on burning intensity and on burning time to the zero-intensity zero-exposure limit. The measured kinetics were analyzed according to the approach presented in [72] in order to determine the quantum efficiency of PSHB. The following is a brief review of the method for determination of this important parameter. We express the quantum efficiency, i.e., the ratio of molecules participating in hole burning to the total number of photoexcited molecules, in the parameterized form of $j = \exp(-a)$. Following the reasoning in [73, 74, 75], we assume that the parameter a is subject to a Gaussian distribution. Taking into account the dispersion for hole burning kinetics due to the difference in absorption at the laser frequency for centers within the in-

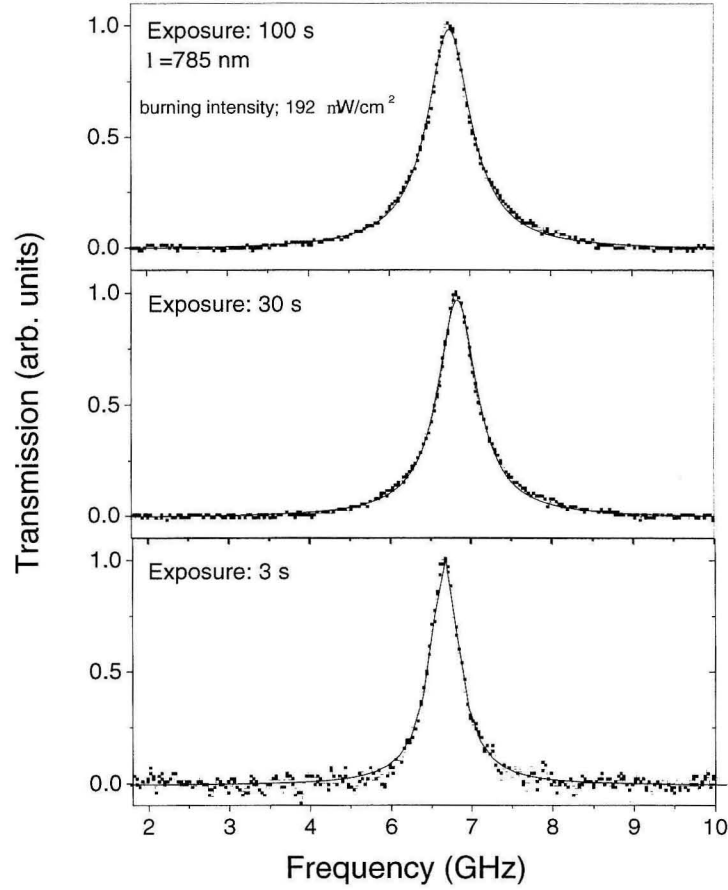


Figure 4.5: Normalized spectral hole profiles for Zn-TBNP at 1.5 K at different exposure with burning intensity of 192 mW/cm².

homogeneous band, the random orientation of the absorbing centers with respect to the polarization of the burning light and the distribution of quantum efficiency and the time dependence $H(t)$ of the sample absorption at the peak of the hole can be calculated as:

$$\begin{aligned}
 H(t) = B + \frac{3D}{2w} \sqrt{\frac{4\ln(2)}{\pi}} \int_0^\infty \int_0^\infty \exp\left(-\frac{I \exp(-a)\alpha\sigma \cos^2 \Theta}{2} t\right) \\
 I_o\left(\frac{I \exp(-a)\alpha\sigma \cos^2 \Theta}{2} t\right) \cos^2 \Theta \sin \Theta d\Theta \exp\left(-4\ln(2)\frac{(a-a_c)^2}{w^2}\right) da. \quad (4.3)
 \end{aligned}$$

where a_c and w are the center and width of the distribution of parameter a , $I_o(x)$ is a

modified Bessel function of zero-order, I is the photon flux of the burning irradiation, σ is the peak homogeneous absorption cross section, and α is the Debye-Waller factor. Eqn. 4.3 assumes hole burning through the Lorentzian shaped zero-phonon lines. D is the maximum relative hole depth ($0 < D < 1$), and $B = 1 - D$ represents the fraction of non-burnable background. Two material parameters, α and σ , required for the fitting procedure, were obtained in the following way. The Debye-Waller factor a was estimated for H₂-TBNP/PVB and Zn-TBNP/PVB to be 0.8 and 0.9, respectively. For simplicity we set $\alpha = 1$ for the other materials. The σ was calculated using the integral absorption cross section σ_{int} , which was determined from the absorption and concentration data as $\sigma = (\Gamma_{inh}/\Gamma_h) \sigma_{int}$. The inhomogeneous broadening Γ_{inh} , was determined from the width of the 0-0 electronic transition in the decomposition fit. We suggest that the homogeneous linewidth Γ_h is half of the determined minimal holewidth since no spectral diffusion was observed in the time range of 10 - 10⁵ seconds. To avoid error due to the hole burning through the phonon sidebands, we fit the experimental kinetics at the initial stages of the hole growth using eqn. 4.3 with two free parameters, a_c and w . The parameter D was fixed by the independent measurement of the maximal saturated hole depth at the highest experimentally achievable exposures. Another way to find D was to record the kinetics at two reduced burning intensities. Then, fitting was performed simultaneously for the initial segments of these kinetics with fitting parameters a_c , w and D shared for both datasets. Due to the additional dataset, a single set of parameters a_c , w and D can be found. With the distribution parameters a_c and w obtained, we calculated the average quantum efficiency $\langle \phi \rangle$ of PSHB.

Fig. 4.6 (a) shows the representative PSHB kinetics for H₂-TBNP in PVB. The experimental kinetics (curve a.1) are satisfactorily described by eqn. 4.3 with a single value of quantum efficiency (smooth curve) and do not require the introduction of a distribution of ϕ . This result is a clear sign that the photochemical reaction is most likely caused by proton phototautomerization with a constant (non-distributed) value for the quantum efficiency [76]. For illustration purposes, curve a.3 does not fit the experimental data well when the polarization of the laser light is not taken into

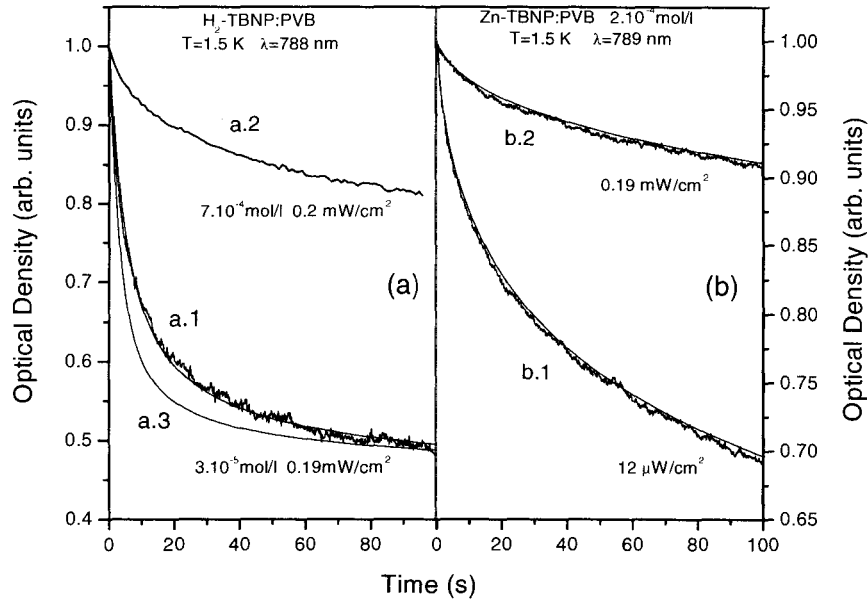


Figure 4.6: Hole burning kinetics for H₂-TBNP (a) and Zn-TBNP (b) at 1.5 K. (a.1). Experimental kinetics recorded using a laser diode with intensity 0.2 mW/cm² for the sample with concentration 7·10⁻⁴ mol/l. (a.2) Experimental kinetics recorded with intensity of 192 mW/cm². (a.3) All fitting curves used $a = 0.9$ and $s = 2.6 \cdot 10^{-11}$ cm². Experimental kinetics recorded with intensities (b.1) 192 mW/cm² and (b.2) 10 mW/cm². The corresponding fitting curves were obtained by fitting simultaneously both experimental datasets with the same values of a_c , w , and D , and the proper burning intensity for each dataset. Both fitting curves used $a = 0.9$ and $s = 1.7 \cdot 10^{-11}$ cm².

account. The quantum efficiency and maximal relative hole depth were found from the fitting procedure to be $(8.9 \pm 1.2) \cdot 10^{-3}$ and 0.58 ± 0.05 , respectively. The observed quantum efficiency for H₂-TBNP/PVB is about one order of magnitude higher than that found for H₂-phthalocyanine in polymer matrices [77], and two to three orders of magnitude higher than that found for several nonporphyrin photochemical systems [78]. The experimental hole burning kinetics in Zn-TBNP measured with two substantially different intensities are presented in fig. 3b (curves b.1 and b.2). Both datasets were fitted simultaneously by eqn. 4.3 (smooth curves). Parameters a_c , w , and D were found to be 9.15, 6.0 and 0.72, respectively. The value obtained for D is in good agreement with the limit for hole depth of $D = 0.74$ obtained from long 10⁵ s

kinetics. The average quantum efficiency was calculated to be $(1.1 \pm 0.2) \cdot 10^{-3}$. The observed distribution of the quantum yields suggests that Zn-TBNP possesses a non-photochemical mechanism [73] that is likely related to the rotation of side molecular groups attached to either a relatively rigid phthalocyanine ring or the host structure. A relatively low yield of $7 \cdot 10^{-6}$ was estimated for nonphotochemical PSHB in Zn-tetraphenylporphine in PMMA [80]. Our result in Zn-TBNP is two orders of magnitude higher and only about ten times less than the yield for photochemical hole burning in H₂-TBNP. The fairly large size of the naphthalocyanine skeleton and the large number of side groups participating in the nonphotochemical PSHB can qualitatively explain this effect. It should be noted that an efficiency as high as 0.11 was reported for nonphotochemical hole burning for Al-phthalocyanine -tetrasulfonate in hyperquenched water [81]. Results for all samples studied are shown in Table 4.2.1. Because the detection noise is about 1% for the observed kinetics, the accuracy of the obtained results was mostly determined by the accuracy of the experimental values of σ and was estimated to be $\pm 15\%$. Hole burning in all but one free-base system can be described by a single value of the quantum efficiency. Surprisingly, H₂-TBNP at higher concentrations shows a distribution of efficiencies, which is likely related to the overlapping of single molecule and aggregate absorption bands at the laser frequency. Three out of four studied metallo-based systems reveal the broad distribution of the hole burning efficiency characteristic of a nonphotochemical hole burning. Only Ni-TBNP/PVB displays a single-valued efficiency of about 0.7%. Thus, the mechanism is likely to be photochemical and should be a subject of future investigation. Another interesting result is the very low non-burnable background observed for Si-NPDO which makes this system useful for holographic applications.

4.2.2 Holographic storage

Using the prepared samples of Si-NPDO and H₂-TBNP in PVB and PS, we demonstrated the holographic recording of pages of information at low temperature with high fidelity. The recording set-up is shown in fig. 4.7. The light source was

Sample	Concentration [mole/liter]	Holewidth [MHz]	Inhomog Linewidth [MHz]	σ_h [cm^2]	Efficiency of PSHB [ϕ]	center	width	B
H ₂ - TBNP/PVB	$3 \cdot 10^{-5}$	150	$1 \cdot 10^7$	$8.7 \cdot 10^{-11}$	$8.9 \cdot 10^{-3}$	5.88	0	0.42
H ₂ - TBNP/PVB	$7 \cdot 10^{-4}$	100	$1.5 \cdot 10^7$	$6.2 \cdot 10^{-11}$	$1.3 \cdot 10^{-3}$	6.92	3.5	0.58
H ₂ - TBNP/PS	$5 \cdot 10^{-5}$	1150	$0.9 \cdot 10^7$	$3.2 \cdot 10^{-12}$	$3.2 \cdot 10^{-2}$	3.44	0	0.43
H ₂ - OBP/PVB	$3 \cdot 10^{-4}$	200	$1.6 \cdot 10^7$	$4.5 \cdot 10^{-12}$	$1.1 \cdot 10^{-2}$	4.51	0	0.57
Zn- TBNP/PVB	$2 \cdot 10^{-4}$	380	$1.0 \cdot 10^7$	$1.7 \cdot 10^{-11}$	$1.2 \cdot 10^{-3}$	9.55	6.0	0.28
Zn- TBNP/PS	$1.8 \cdot 10^{-4}$	1000	$1.2 \cdot 10^7$	$4.6 \cdot 10^{-12}$	$1.4 \cdot 10^{-3}$	9.16	6.7	0.48
Ni- TBNP/PVB	$6.4 \cdot 10^{-4}$	100	$1.5 \cdot 10^7$	$2.1 \cdot 10^{-11}$	$6.7 \cdot 10^{-3}$	5.0	0	0.67
Si- NPDO/PVB	$2.0 \cdot 10^{-4}$	400	$2.0 \cdot 10^7$	$8.7 \cdot 10^{-11}$	$8.1 \cdot 10^{-4}$	10.06	4.7	0

Table 4.1: Spectroscopic and hole burning parameters for naphthalocyanines doped polymers at 1.5 K.

a Hitachi 50 mW, Fabry-Perrot temperature controlled laser diode with wavelength centered at 785nm (@25 C). The wavelength can be coarsely tuned by temperature variation (0.2nm/degree Celsius) and fine tuned by varying the laser diode current at a rate of 2.3 GHz/mA. A computer controlled current source from ILX Lightwave with 0.1 mA resolution (0.23 GHz) was used to drive the laser diode. An intensity mask consisting of random binary bit patterns with a pixel size of $100 \times 100 \mu\text{m}$ is imaged with a $4f$ system onto the polymer sample placed inside the cryostat. The dimensions of the polymer sample are $1 \times 1 \text{ cm}^2$. A $4f$ imaging system images the mask back onto a *STAR cam* CCD camera. An iris placed at the Fourier plane of the imaging lens filters the signal for unwanted reflections from the cryostat windows and scattering from the sample. The reference and signal beams make an angle of 20 degrees outside the sample. The reference beam consists of a plane wave of intensity 0.2 mW/cm^2 equal to the intensity of the signal beam. At this intensity, we observed a homogeneous line broadening of 1 GHz for the samples mentioned above. The pathlength difference between the reference and signal arm is equal to $\Delta L = 14 \text{ cm}$.

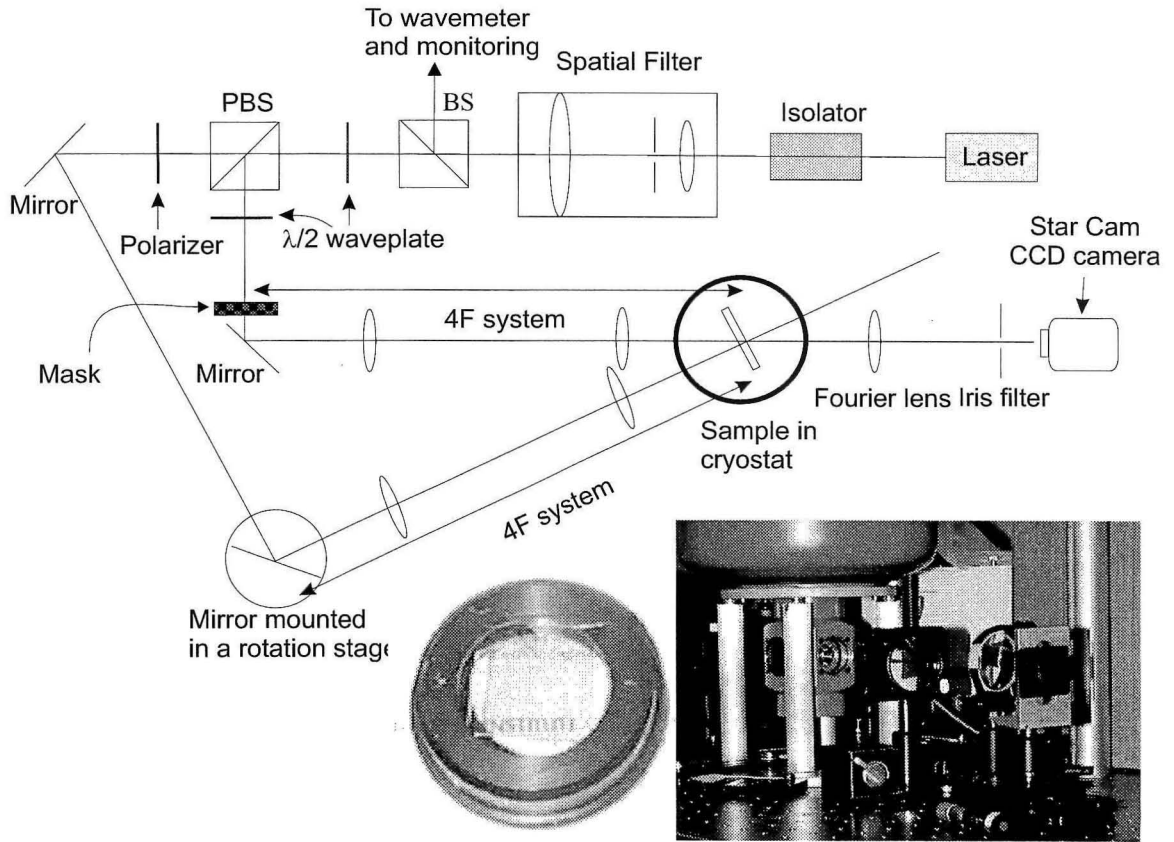


Figure 4.7: Experimental set-up for the hologram recording. The mask, composed of random binary pixels, is imaged onto the sample inside the cryostat by a 4f system and is recorded with a plane wave reference.

The phase shift $\Delta\phi$ of the interference pattern depends on the frequency shift $\Delta\nu$:

$$\Delta\phi = \frac{2\pi \Delta L}{c} \Delta\nu. \quad (4.4)$$

When the laser frequency is shifted by 1 GHz, the phase shift $\Delta\phi$ is equal to π . This phase shift is used to cancel the absorption grating and reveals only an index grating in the center of the burning frequency through the Kramers-Kronig relations [83, 84]. Holograms were recorded for 4 sec. The reconstruction of holograms in 400 μm thick H_2 -TBNP/PVB at 788 nm, 400 μm thick Si-NPDO/PVB at 787nm and 1.5 mm thick H_2 -TBNP/PS at 788 nm are shown in fig. 4.8 (a)-(c), respectively.

The reconstruction from the thick sample shows defects due to non-uniformity. Better optical quality was obtained for the H_2 -TBNP in PVB than in the Polystyrene

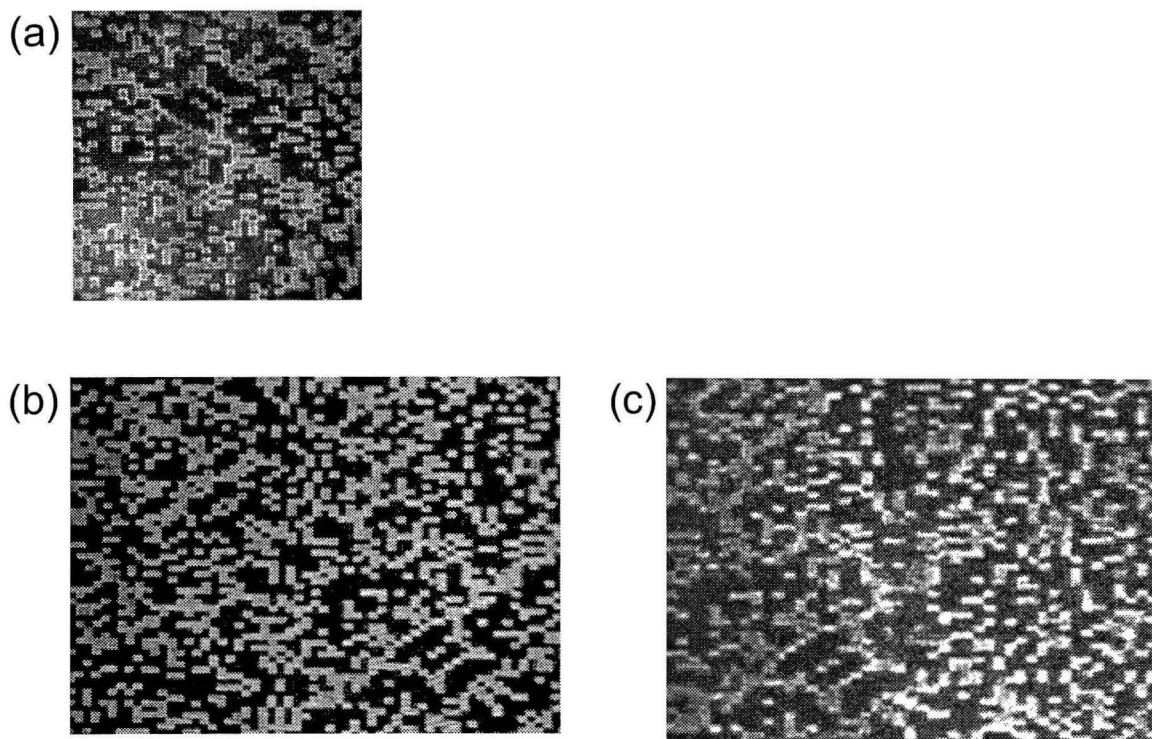


Figure 4.8: Holograms of random bit patterns $100 \times 100 \mu\text{m}$ recorded in three polymer films at 1.9 K: a) $400 \mu\text{m}$ TBN in PVB matrix (788 nm). b) $400 \mu\text{m}$ SiNDO in PVB matrix (777 nm). c) 1.5 mm TBN in polystyrene (788nm).

matrix. The sample optical densities were 2.0, 2.3, and 7.2, and the absolute diffraction efficiencies were $5 \cdot 10^{-5}$, $7 \cdot 10^{-5}$, and $1.8 \cdot 10^{-6}$, respectively. The low absolute diffraction efficiency is due to lower hole depth and higher absorption. Especially in the case of H_2 -TBNP/PVB, the sample with the large concentration of $7 \cdot 10^{-4}$ mol/l showed reduced hole depth, probably due to aggregation. The kinetics obtained with the laser diode for that sample are shown in fig. 4.6(a.2). We measured a hole depth of 4% with the exposure energy used in the holographic recording. By calculating the diffraction efficiency using the coupled wave analysis and the measured value of the hole depth, we obtained a diffraction efficiency in agreement with the experimental value. If instead, the lower concentration sample from fig. 4.6(a.1) had been used, the diffraction efficiency could be as high as 0.8% (computed for a pure absorption grating with 50% hole depth and optical density 0.7). This preliminary holographic experiment shows that random bit patterns can be recorded in these materials with good

fidelity. The relationship between the intensity line broadening and the hole depth at various hole burning frequencies has to be studied further for these materials in order to address the recording rate and storage capacity.

Spectral hole burning properties of several free-based and metallo-naphthalocyanine compounds in two polymer hosts were studied for storage applications with diode lasers. Metallo-naphthalocyanines displayed a nonphotochemical hole-burning mechanism, while free-base molecules exhibited the photochemical proton tautomerization mechanism. The minimal holewidth was found to be between 100 MHz and 1200 MHz at 1.5 K. The inhomogeneous linewidth was found to be approximately 107 MHz which makes these compounds suitable for storing multiple holograms at different frequencies, and for terahertz bandwidth storage and communications applications. The hole-burning kinetics were analyzed, and the quantum efficiencies of hole burning were determined for all materials to be between 0.1% and 1%. High fidelity holograms (data pages) in the transmission geometry were successfully recorded and reconstructed in the materials studied using single frequency laser diodes.

4.3 $M/\#$ of absorption and index holograms in SHB media

In section 4.2, we presented a set of wavelength selective polymer materials that have a large frequency multiplicity (table 4.2.1). The storage capacity can be further increased by adding Bragg multiplexing (angle, peristrophic or shift) at each frequency channel. A system measure for the hologram diffraction efficiency obtainable by superimposing M holograms at a single location and frequency is given by the $M/\#$ [43]. The $M/\#$ is usually used for materials exhibiting a refractive index modulation and is defined as:

$$\eta = \left(\frac{M/\#}{M} \right)^2. \quad (4.5)$$

where η is the equalized diffraction efficiency of the M holograms.

An absorption modulation is created by interfering two beams in a spectral hole burning material. An index modulation is also induced from an absorption modulation as explained in section 4.2. In this section, we show that the system measure given by the M-number is also applicable to absorption gratings. We derive the $M/\#$ of pure absorption gratings as well as of index gratings generated from absorption gratings. We compute the $M/\#$ using experimental absorption kinetics from the polymer samples described in the previous section.

4.3.1 Absorption kinetics

We start by describing the absorption kinetics $\alpha(t)$ of a spectrally selective material under exposure of coherent monochromatic light. We model the absorption kinetics as:

$$\alpha(t) = B + Ae^{(-KI(\mathbf{r},t)t)} \quad (4.6)$$

$$\alpha_o = A + B, \quad (4.7)$$

where $I(\mathbf{r}, t)$ is the light intensity pattern and K is a kinetic parameter that depends on the material. B is the non-burnable absorption and represents an absorption background that persists after large bleaching energy (fig. 4.6). α_o is the absorption of the material before illumination. This model is a simplification of a more rigorous model described by eqn. 4.3, which takes into account the distribution of quantum efficiency, polarization dependence and the random orientation of absorbing centers. Experimentally, the absorption kinetics do not follow a mono-exponential decay. However, a bi-exponential decay accurately models the kinetics. The addition of a second exponential decay does not change the overall result of the analysis but complicates it unnecessarily; therefore, a bi-exponential decay will be used only to obtain quantitative results from experiments. For the remainder of the analysis, we assume that the absorption kinetics follow a mono-exponential behavior described by eqn. 4.7.

The intensity pattern of the i^{th} hologram produced by the interference of the

reference and signal beam, R_i and S_i is written as:

$$I(\mathbf{r}, t) = |R_i|^2 + |S_i|^2 + R_i S_i^* \exp(-j \mathbf{k}_i \mathbf{r}) + R_i^* S_i \exp(j \mathbf{k}_i \mathbf{r}) \quad (4.8)$$

Eqn. 4.8 assumes that the grating is uniform throughout the medium. For low optical density, this approximation is valid. For large optical density, one has to consider the depletion of the beams inside the medium. The absorption after the recording of the M^{th} hologram is computed by substituting eqn. 4.8 into eqn. 4.7:

$$\alpha_M = B + A \exp\left(-KI_o \sum_{i=1}^M (1 + V_i \cos(\mathbf{k}_i \mathbf{r})) t_i\right) \quad (4.9)$$

$$= B + A \exp\left(-KI_o \sum_{i=1}^M t_i\right) \exp\left(-KI_o \sum_{i=1}^M V_i t_i \cos(\mathbf{k}_i \mathbf{r})\right) \quad (4.10)$$

where V_i is the modulation depth of the i^{th} hologram ($V_i = \frac{2|R_i|^*|S_i|}{|R_i|^2 + |S_i|^2}$). We choose the recording time of each hologram t_i to be identical and equal to τ and the modulation depth equal to $V_i = 1$. We assume also that the recording time of each hologram $\tau \ll KI_o$, which is a condition satisfied when multiple holograms are written. Eqn. 4.10 is then equal to:

$$\alpha_M = B + A \exp(-KI_o M \tau) \left(1 - KI_o \tau \sum_{i=1}^M \cos(\mathbf{k}_i \mathbf{r})\right) \quad (4.11)$$

$$= \overline{\alpha}_o - \alpha_1 \sum_{i=1}^M \cos(\mathbf{k}_i \mathbf{r}) \quad (4.12)$$

From eqn. 4.12, the resulting DC absorption $\overline{\alpha}_o$, obtained after the recording of M holograms, is equal to:

$$\overline{\alpha}_o = B + A \exp(-KI_o M \tau). \quad (4.13)$$

and the grating strength α_1 of each hologram is identical and equal to:

$$\alpha_1 = A \exp(-KI_oM\tau) KI_o\tau. \quad (4.14)$$

4.3.2 M/# of pure absorption holograms

Here we assume that recording and read-out occurs at the same optical frequency. An absorption and index grating are created (fig. 4.2). However, at the read-out frequency, the index grating does not contribute to the diffraction and therefore the hologram can be considered a pure absorption hologram. We studied different recording geometries such as transmission, reflection, and 90-degree. Similar results are obtained in each case. In the following, we treat the symmetric transmission geometry for simplicity. The diffraction efficiency is obtained using Kogelnick's expression [82]:

$$\eta = \exp\left(-\frac{2\bar{\alpha}_o d}{\cos\theta}\right) \left(\frac{\alpha_1 d}{2\cos\theta}\right)^2, \quad (4.15)$$

where d is the thickness of the recording medium, and θ is the angle between the reference and signal beam inside the material. The dc component of the absorption $\bar{\alpha}_o$ and the absorption modulation α_1 after the recording of M holograms are computed from eqn. 4.13 and eqn. 4.14.

The diffraction efficiency η versus the normalized recording time t/KI_o is shown in fig. 4.9. The graph consists of four plots that correspond to four values of optical densities OD ($OD = 2\alpha_0 d$). The number of recorded holograms M is 10. The non-burnable absorption parameter B is set to 0 in this calculation. The diffraction efficiency reaches a maximum for a given normalized recording time. The maximal diffraction efficiency is obtained from eqns. 4.13, 4.14 and 4.15:

$$\eta_{max} = \left(\frac{M\#}{M}\right)^2 \quad (4.16)$$

$$M\# = \exp\left(-\frac{Bd}{\cos\theta}\right) \frac{Ad}{2\cos\theta} C_{max}(Ad/\cos\theta) \quad (4.17)$$

$$C_{max}(Ad/\cos\theta) = \max_{\beta} \left(\beta \exp(-\beta) \exp\left(-\frac{Ad}{\cos\theta} \exp(-\beta)\right) \right), \quad (4.18)$$

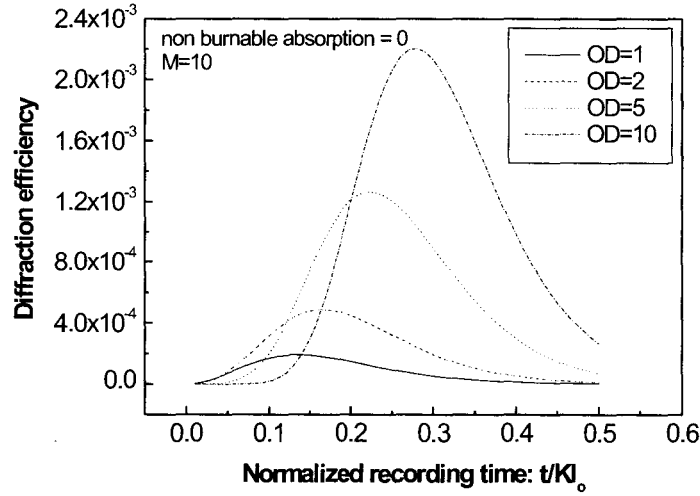


Figure 4.9: Diffraction efficiency η versus normalized recording time t/KI_o for M multiplexed holograms. The recording time t is constant for all exposures.

where $\beta = KI_oM\tau$. The parameter β is proportional to the total exposure time $I_oM\tau$. According to eqn. 4.17, the $M/\#$ is independent of the number of recorded holograms M . However, the maximum $M/\#$ obtainable is subject to an optimization of the recording time. Because diffraction efficiency η_{max} is inversely proportional to the square of the number of holograms M , the system measure described by $M/\#$ can be applied. The result of the $M/\#$ calculation is plotted in fig. 4.10. The graph shows the $M/\#$ vs. optical density ($\alpha_o \cdot d$) of the material. The three curves are plotted for three values of the non-burnable absorption B . The quantity B is computed as a fraction of the optical density. When $B = 50\%$ of the optical density, the $M/\#$ reaches its maximum value of 0.05 for an optical density $\alpha_o d = 1.8$. The $M/\#$ increases when B decreases (the medium becomes more transparent). In the limit when $B=0$, the theory predicts that the $M/\#$ increases logarithmically with the optical density. When the optical density becomes too large, these results are not valid because the grating strength of each hologram ceases to be uniform throughout the thickness, and eqn. 4.15 cannot be used to compute the diffraction efficiency.

For comparison, the $M/\#$ for a pure index grating in the transmission geometry

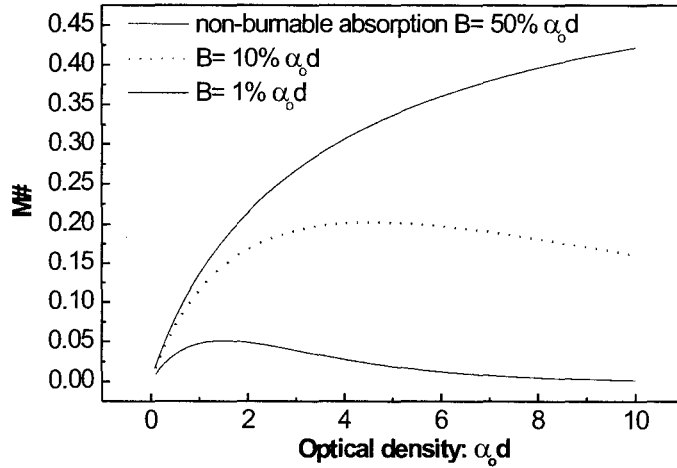


Figure 4.10: $M/\#$ for absorption holograms. The wavelength of the writing and reading beam is unchanged ($\lambda_{write} = \lambda_{read}$).

is given by:

$$M/\# = \exp\left(-\frac{Bd}{\cos\theta}\right) \frac{\pi\Delta n_o d}{\lambda \cos\theta}. \quad (4.19)$$

This expression is similar to eqn. 4.17. The $M/\#$ is proportional to the maximum index modulation Δn_o while in eqn. 4.17, the $M/\#$ is proportional to the absorption modulation A attenuated by a factor $C_{max}(Ad/\cos\theta)$.

4.3.3 $M/\#$ of pure index holograms

An interesting property of wavelength selective materials is that light can be diffracted by both an absorption modulation and the induced index modulation. The advantage of index gratings is that the diffraction efficiency can reach 100% if the absorption at the read-out frequency is equal to zero. Here, we analyze the $M/\#$ when absorption modulation is transformed to index modulation. A pure index grating can be created by using two holographic exposures at two optical frequencies with a π phase shift between the two exposures. The hologram generated is the so-called

Π -hologram. We assume that the absorption modulation α_1 has a Lorentzian shape:

$$\alpha_1 = (B - \alpha_o) \exp(-KI_oM\tau) KI_o\tau \frac{\gamma^2}{(\omega_b - \omega)^2 + \gamma^2}. \quad (4.20)$$

where γ is the homogeneous linewidth and ω_b the writing (burning) optical frequency. The index grating strength β_1 induced by the absorption grating is equal to:

$$\beta_1 = \alpha_1 \frac{\omega_p - \omega}{\gamma}. \quad (4.21)$$

where ω_p is the read (probe) frequency. A Π -hologram is recorded with a first exposure at frequency ω_{b_1} and a second exposure (same exposure energy) at frequency ω_{b_2} . The diffracted field E_d of the Π -hologram is equal to:

$$E_d = -E_r \exp\left(-\frac{\overline{\alpha}_o d}{\cos\theta}\right) \left[\left(\frac{\alpha_1(\omega_{b_1})d}{2\cos\theta} + j \frac{\beta_1(\omega_{b_1})d}{2\cos\theta} \right) e^{j\phi_1} + \left(\frac{\alpha_1(\omega_{b_2})d}{2\cos\theta} + j \frac{\beta_1(\omega_{b_2})d}{2\cos\theta} \right) e^{j\phi_2} \right] \quad (4.22)$$

where ϕ_1 and ϕ_2 are the phases of the grating in exposures 1 and 2 respectively. If we choose $\phi_2 - \phi_1 = \pi$, the diffraction efficiency computed from eqn. 4.22 becomes:

$$\eta = \exp\left(-\frac{2\overline{\alpha}_o d}{\cos\theta}\right) \frac{d^2}{4\cos^2\theta} [(\alpha_1(\omega_{b_2}) - \alpha_1(\omega_{b_1}))^2 + (\beta_1(\omega_{b_2}) - \beta_1(\omega_{b_1}))^2]. \quad (4.23)$$

If the Π hologram is read-out at frequency $\omega_p = \frac{\omega_{b_1} + \omega_{b_2}}{2}$, the absorption grating cancels and only the index grating prevails:

$$\eta = \exp\left(-\frac{2\overline{\alpha}_o d}{\cos\theta}\right) \frac{d^2}{4\cos^2\theta} 4\alpha_1^2 \left[\left(\frac{\Delta\omega}{2\gamma} \right)^2 \frac{\gamma^2}{(\omega_b - \omega)^2 + \gamma^2} \right]^2. \quad (4.24)$$

where $\Delta\omega = \omega_{b_2} - \omega_{b_1}$. The function in brackets has a maximum for $\Delta\omega = 2\gamma$. When read-out for a long time at frequency $\frac{\omega_{b_1} + \omega_{b_2}}{2}$, the index grating is not erased and the remaining absorption is equal to the non burnable absorption parameter B . Therefore, in the exponential we replace $\overline{\alpha}_o$ with B . Thus, the diffraction efficiency

of a Π hologram becomes:

$$\eta = \exp\left(-\frac{2Bd}{\cos\theta}\right) \left(\frac{\alpha_1(\omega_{b_1})d}{2\cos\theta}\right)^2. \quad (4.25)$$

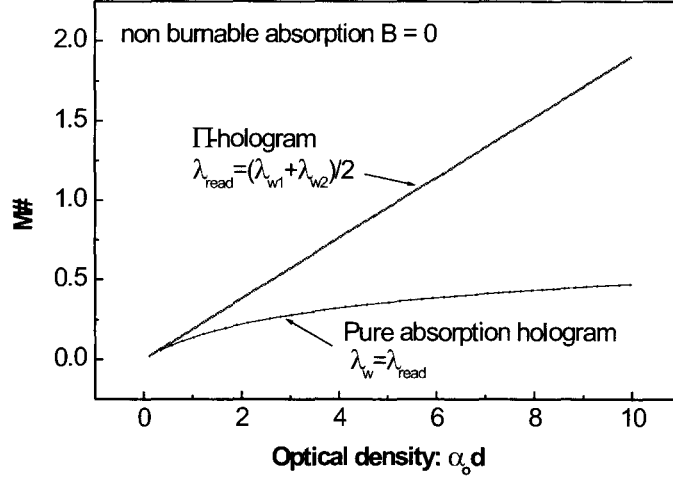


Figure 4.11: $M/\#$ comparison between pure absorption holograms and Π -holograms when the non-burnable background absorption is equal to zero ($B=0$).

The assumption that the index grating is not erased during read-out at frequency $\frac{\omega_{b_1} + \omega_{b_2}}{2}$ is not an accurate description. The tail of the Lorentzian absorption curve affects the absorption holograms recorded at frequencies ω_{b_1} and ω_{b_2} . A decay of the absorption hologram's strength induces a proportional decay of the induced index hologram's strength. When the two absorption holograms are recorded many homogeneous linewidths away, the decay of the index grating is much slower than the decay of the remaining absorption at the read-out frequency $\omega_{b_1} + \omega_{b_2}/2$; therefore, the assumption is valid. However, the maximum induced index modulation is achieved when $\Delta\omega = 2\gamma$ and the assumption ceases to be valid. Nevertheless, this assumption provides an insight for the upper bound of the $M/\#$ achievable using Π -holograms for multiplexing.

Eqn. 4.25 is similar to the expression found for a pure absorption hologram, except for the absorption term in the exponential. When the non-burnable background B is

equal to 0, the medium is transparent at the read-out wavelength and the diffraction efficiency is proportional to the optical density. Fig. 4.11 shows a comparison between the $M/\#$ obtained with Π -holograms and pure absorption holograms. The result of fig. 4.11 suggests that Π -holograms yields larger $M/\#$ than for pure absorption holograms. When the optical density is larger than approximately 3, the holograms become non-uniform inside the medium. In fact, the dynamic range is peeled off at the front of the material and the hologram is built up towards the back. These non-uniformities decrease the value of the $M/\#$ plotted in fig. 4.11 when $\alpha_o d > 3$. Fig. 4.12 plots the $M/\#$ for different values of the non-burnable background.

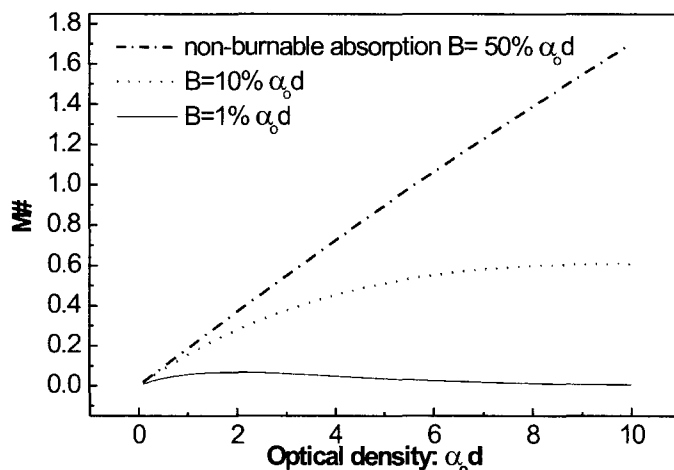


Figure 4.12: $M/\#$ versus optical density when multiplexing Π -holograms. The parameter B is the non-burnable background absorption.

The $M/\#$ obtainable in SHB polymer material can be estimated by fitting the absorption kinetics with a bi-exponential function and computing the resulting grating strength α_1 and DC absorption $\bar{\alpha}_o$. The absorption is measured at 1.9 Kelvin in a $400\mu\text{m}$ thick sample of H_2TBN in polyvinyl butyral (PVB) with a bleaching intensity of $10\mu\text{W}/\text{cm}^2$ (inset of fig. 4.13) and concentration of $5 \cdot 10^{-5}$ mol/l. Fig 4.13 illustrates the $M/\#$ that can be obtained using the above material as a function of the sample thickness. An $M/\#$ of 0.04 can be reached with that particular sample.

M number computed from experimental
absorption curve

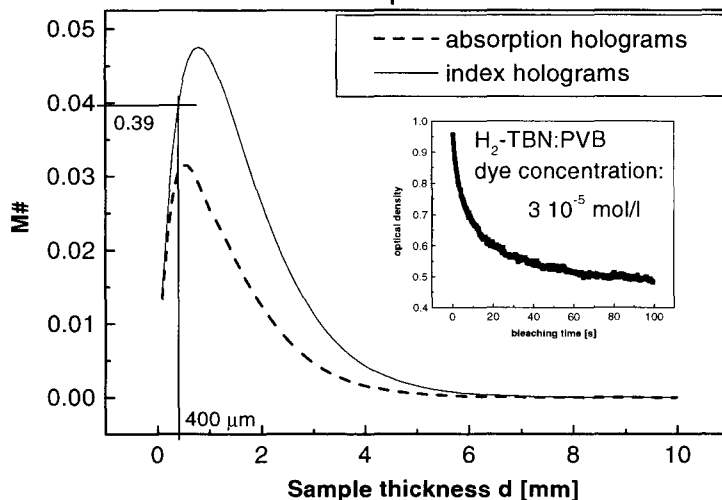


Figure 4.13: $M/\#$ versus optical density derived from the experimental absorption kinetics shown in the inset of the plot.

The remaining absorption B is the dominant factor in the $M/\#$ equations for absorption and index holograms. The computed values for the $M/\#$ of index and absorption holograms are close. However, it is advantageous to use Π -holograms instead of pure absorption holograms because the frequency dependence of Π -holograms fall off as the square of the frequency while absorption holograms fall off proportionally to the frequency. We have shown that multiplexing holograms in a wavelength selective material yields an $M/\#$ of 0.05 using the polymer materials presented above. Potentially, an $M/\#$ of 0.5 can be achieved by recording Π -holograms and using a material with low non-burnable background. Experimentally, the number of multiplexed holograms at a single frequency and location is limited to about 10. With an $M/\#$ of 0.05 and $M=10$ holograms, the maximum diffraction efficiency is equal to $2.5 \cdot 10^{-5}$, which is enough to obtain good SNR values.

4.4 Ultra fast all-optical logic

The large inhomogeneous bandwidth ($>10\text{THz}$) of the SHB polymer materials (section 4.2.1) can be used for spatio-temporal optical processing and storage of femtosecond pulses (a 100 fs pulse has a bandwidth of 10 THz) [85, 86]. Optical processing of pulses requires that digital logic operations be performed. Electronic detectors have response times on the order of $\simeq 100$ ps, too slow to process femto and picosecond pulses. An all-optical method is needed to build the logic. We show in this section an implementation of ultra-fast all-optical logic that is compatible with the spectral hole memory developed in this chapter.

For optical communication, bitwise logic can be used for address recognition in time division multiplexing systems. Time division demultiplexing can be performed optically at a much faster rate than what is currently achieved electronically [87]. Optical gates using four wave mixing in semiconductors have been proposed, and a spectacular AND gate working at 100 Gbit/s has been demonstrated [88]. In this paper, we propose and demonstrate a set of optical logic gates (AND, OR, XOR) with 140 fs resolution based on SHG (second harmonic generation). Non-resonant effects such as the Kerr effect and wave mixing (e.g. second harmonic generation) occur at subfemtosecond timescales and are therefore candidates for realization of ultra-fast computing machines.

An experimental demonstration of a set of optical logic gates (OR, XOR, AND) is shown using non-linear mixing in a BBO crystal. We use femtosecond laser pulses from a modelocked Ti:sapphire laser and non-linear mixing in a BBO crystal to demonstrate the gates. The output of the gate has twice the optical frequency of the input which makes it difficult to cascade gates. We propose a solution to this problem and discuss the requirements for femtosecond computing machines. A 2 bit full adder is described as an example using the proposed optical gates.

4.4.1 Principle

In this section, we describe the working principle of the logic gate. Input data are encoded spatially as streams $X_1(t) \dots X_{2N}(t)$ of femtosecond pulses (encoded from a single pulse with the pulse shaper presented in section 2.6). The N input streams are incident at different spatial positions on a diffractive optical element (DOE). The DOE acts as a position dependent focal length lens as shown in fig. 4.14. All inputs are assumed to be produced by the same laser so that they remain coherent with each other. Data streams are incident symmetrically with respect to the optical axis of the DOE. Inputs at the edge of the DOE (e.g., X_1, X_2) are brought to a focus Y_1 that is further away than the focus spot Y_2 generated by inputs close to the optical axis (e.g., X_3, X_4). Each pair of inputs needs to satisfy the non collinear second harmonic phase matching condition. For moderate group velocity mismatch (short interaction length), the system impulse response function is very narrow and the second harmonic field can be considered to be proportional to the product of the two input fields [89]:

$$Y_j = \kappa X_k X_l, \quad k \neq l = 1 \dots 2N, \quad (4.26)$$

where κ accounts for the conversion efficiency of the SHG process.

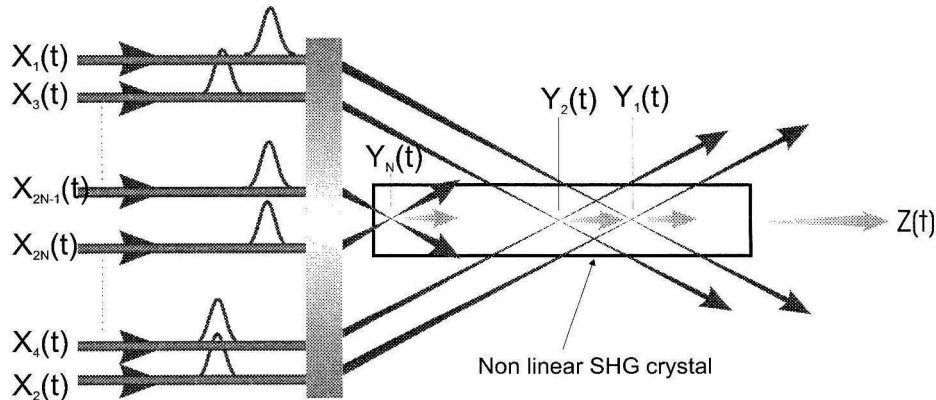


Figure 4.14: Principle of the all-optical gate by second harmonic generation.

The logic state values ("1") and ("0") are produced by amplitude modulation.

Whenever a pulse from the stream $X_1(t)$ collides simultaneously with a pulse of stream $X_2(t)$ in the non-linear crystal, a photon is created at twice the optical

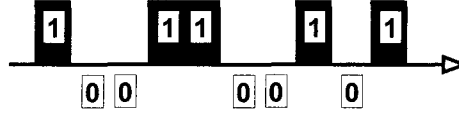


Figure 4.15: Amplitude coding.

frequency which propagates in the direction of the optical axis (fig. 4.14). The non-collinear SHG process is an AND gate, since a logic state "1" is produced only when two pulses ("1" and "1") are present simultaneously ($Y_1 = X_1 X_2$). Interference occurs between the frequency doubled sources generated at the different locations along the crystal: $Y_i, i=1..N$. We consider for simplicity that the SHG sources, generated at $Y_i, i=1..N$, are point sources. Interference between short pulses of bandwidth $\Delta\nu$ (typ. 10THz) is similar to interference between two broad light sources of short coherence length equal to $c/\Delta\nu$ (typ. $30\mu\text{m}$). Therefore, for interference to occur, the path length difference between the two beams has to be shorter than the coherence length or, equivalently, the two pulses need to overlap in time. Constructive or destructive interference takes place depending of the phase difference of the pulse carrier frequency. The phase difference between the generated point sources can be adjusted by time delaying appropriately the inputs. Fig. 4.16 shows the boolean representation of the optical gate described in fig. 4.14. The function $F(Y_1..Y_N)$ can perform a set of boolean functions. The function F can be modified by delaying the inputs. In other words, this optical gate can be reconfigured to perform another function by acting on the time delay of the input. The function F computes the coherent sum:

$$F(Y_1..Y_N) = \sum_{i=1}^N Y_i e^{i\Delta\phi_i} \quad (4.27)$$

where $\Delta\phi_i$ is the phase difference between each point source Y_i . If $\Delta\phi_i$ is a multiple of 2π , constructive interference occurs. In this case, the function F produces an OR function and the output of the device is a sum of products (OR of AND's of two variables).

The principle of operation of this logic device is similar to interfering $2N$ stream of

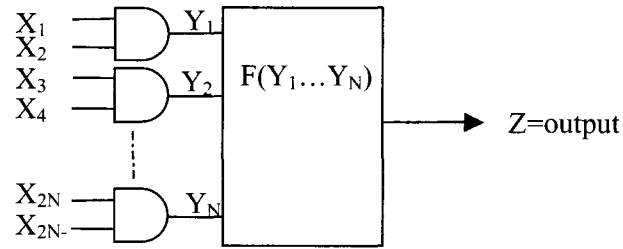


Figure 4.16: Boolean representation of the system shown in fig. 4.14.

pulses using mirrors and beam splitters (without frequency doubling light). However, the SHG based logic gate does not require beam-splitters, waveplates or mirrors allowing therefore a gain in size reduction of the gate, robustness to vibration because interference is produced within the short distance of the crystal length. The inputs are not destroyed during the process of computation. This effect can be useful in decoding the address of a packet of pulses and re-routing it according to its address downstream.

4.4.2 Experimental gates

Based on the logic device presented in section 4.4.1, an AND, OR and XOR gate have been implemented experimentally. The experimental set-up is illustrated in fig. 4.17 and a picture of the set-up is shown in fig. 4.18. The pulse source is a 76 MHz repetition rate modelocked train of pulses from a Ti:sapphire laser (Coherent MIRA) centered at 800 nm with 140 fs duration and average power 300 mW. The raw beam of 1.5 mm diameter is used throughout the experiment. The incoming beam is split by the non-polarizing beam-splitter BS_1 to produce beams A and B. Beam B is split again by the non-polarizing beam-splitter BS_3 , yielding beams B_1 and B_2 . The path length of beams B_1 and B_2 can be adjusted via the delay lines D_3 and D_4 , respectively. Beams B_1 and B_2 are separated by 3mm and propagate collinearly towards a lens. A similar arrangement for beam A produces two collinear beams separated by 3 mm propagating towards the lens. A total of four beams are incident onto a singlet lens of focal length $f = 9$ cm. Each of the four beams can

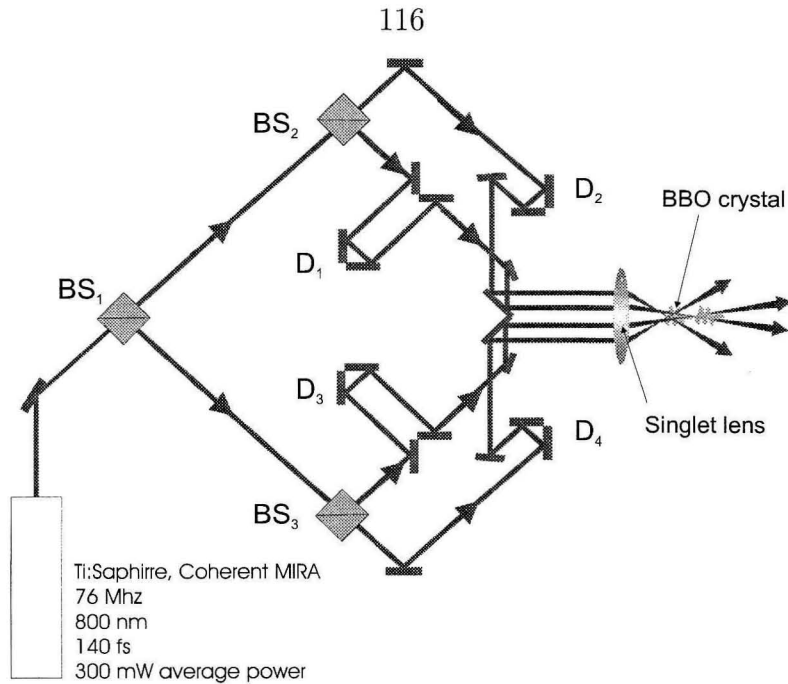


Figure 4.17: Experimental set-up describing the implementation of the optical gates. The beam splitters BS_1, \dots, BS_3 and delay lines $D_1 \dots D_4$ are used to generate the set of inputs. The singlet lens is used as a position dependent focal length. The frequency-doubled light generated by pairs of inputs interfere and serve as the basis for the optical gates.

be delayed with respect to each other by delay lines controlled by micrometer stages. The purpose of the singlet lens is to implement the DOE discussed in section 4.4.1. Here, spherical aberration of the lens is used to obtain a position dependent focal length. The two beams incident on the edge of the lens are brought into a focus that is closer than the focus formed by the two beams close to the optical axis. The lens focuses the four incident beams onto a non-linear 0.5 mm thick BBO crystal. Type I phase matching is used (extraordinary polarization = ordinary + ordinary). We show next that gates of two inputs AND, OR or XOR can be constructed from the optical device described in fig. 4.14. We first demonstrate the AND gate.

4.4.3 AND gate

The AND gate is constructed naturally from the property of non-collinear second harmonic generation. When the two inputs are simultaneously incident on the lens (corresponding to a logic "1" and "1"), the SHG process generates frequency doubled

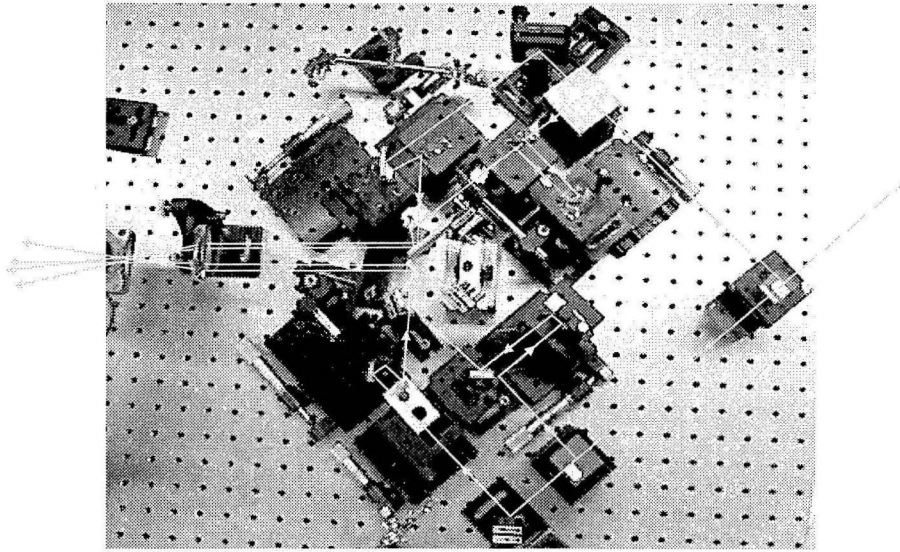


Figure 4.18: Picture of the experimental set-up shown in fig. 4.17.

light. A camera detects the intensity of the pulse at the output. When only one of the beams is present at the input, no frequency doubled light is generated resulting in a logic "0." Fig 4.19 shows the response of the CCD camera. The camera integrates 2.5 millions pulses from the modelocked laser. The SNR is large for this gate because a logic "0" is given by the detector noise and logic "1" is related to the intensity of the second harmonic beam.

4.4.4 OR gate

The two inputs X_1 and X_2 are duplicated by splitting each input into two beams. The resulting four beams are incident on the singlet lens as shown below in fig. 4.20 a). The relative delay between X_1 and X_2 is adjusted (see section 4.4.1) such as to produce a constructive interference between the two SHG sources. The boolean equivalent of this optical gate is shown in fig. 4.20 b).

Constructive interference increases the detected intensity as can be seen from the result in fig. 4.21 (bottom right pulse in the truth table). The logic "1" represented by the SHG pulse intensity is not constant. Although this is irrelevant for a single gate, it becomes important for successive cascaded gates. An optical power limiter placed at the output can equalize the intensity of the second harmonic pulses. SNR

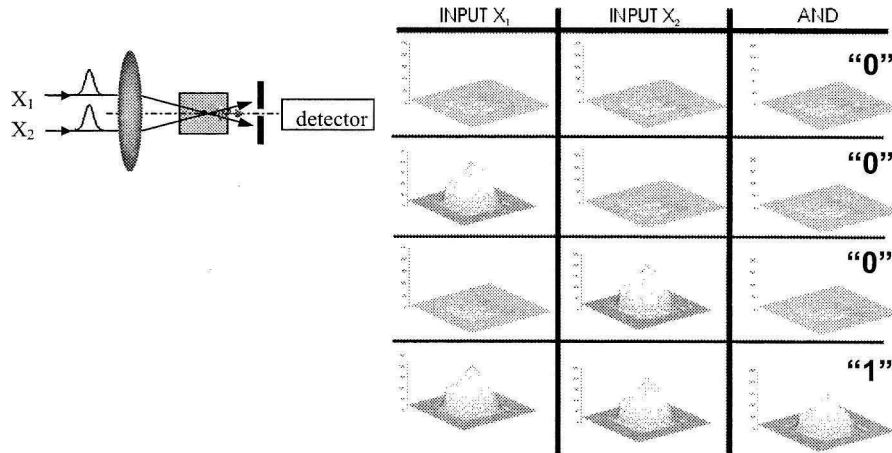


Figure 4.19: Experimental truth table of the optical AND gate.

for this gate is the same as for an AND gate.

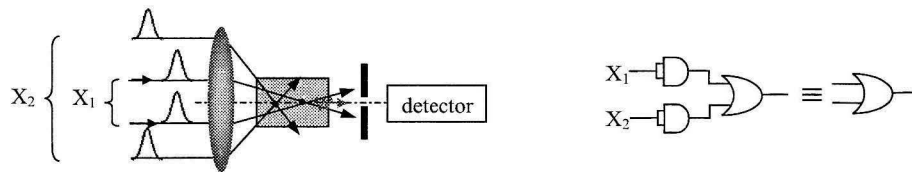


Figure 4.20: OR gate.

4.4.5 XOR gate

The XOR gate works very similarly to the OR gate. The only difference is that the delay is adjusted such as to produce destructive interference. For this gate, the logic state "0" at the output is determined by destructive interference. Any intensity variation between the two interfering beams causes the level of the "0" to go up, reducing the SNR. Fig. 4.22 shows the results. SNR is measured to be 7.8. This is due to non-equal intensity of the interfering beam as can be seen from the result of the "1" + "0" and "0" + "1."

Although, the experiment was done with single pulses, it can be generalized to a stream of pulses, because the mechanism underlying these gates (second harmonic generation, interference) has subfemtosecond resolution. An inverter gate cannot be realized with these gates because of the nature of the logic state chosen (light or no

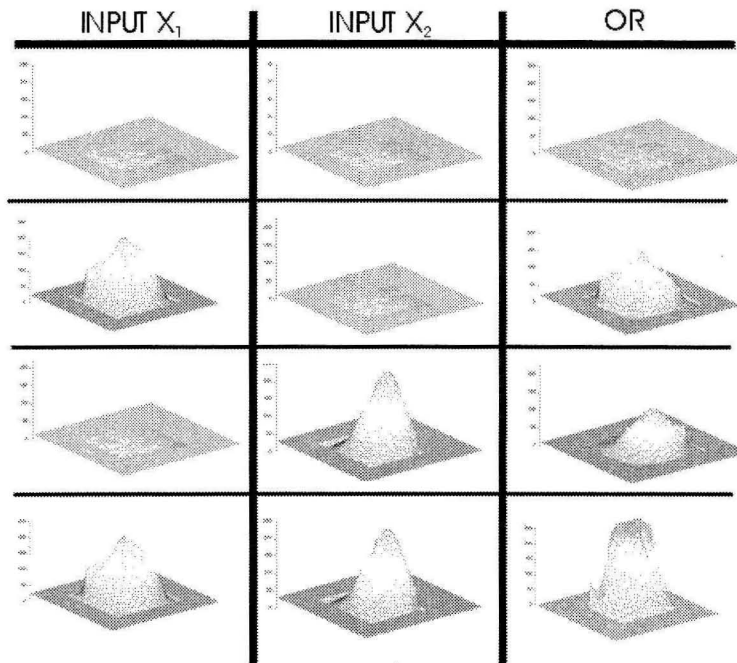


Figure 4.21: Experimental truth table of the optical OR gate.

light). Interestingly, another type of element needed to cascade gates can produce the NOT gate as we will show next.

4.4.6 Cascading gates

This section discusses the problem of gate cascading and presents a possible solution. The wavelength of the output from the gate is half the wavelength of the input signal. For cascading gates, we need to transform the blue wavelength back into IR with fidelity. Essentially, we need to perform a wavelength conversion. Frequency down conversion requires 4 wave mixing and looks prohibitively bulky and complicated. Another approach is to use the non-linear property of polymers. Polyacetylene and its substitutes have been studied extensively for their high non-linear susceptibility and ultra fast decay time [90]. For example, poly[(4-tert-butyl-2,6-dimethylphenyl)acetylene] (PMBPA) has a fairly broad absorption spectrum in the visible range (350-600 nm) and negligible absorption in the infrared (800 nm). When illuminated with pulses of blue-green light, photoexcitation takes place almost instantaneously (within 10 fs), creating electron-hole (fig. 4.24). Ultra short lifetime

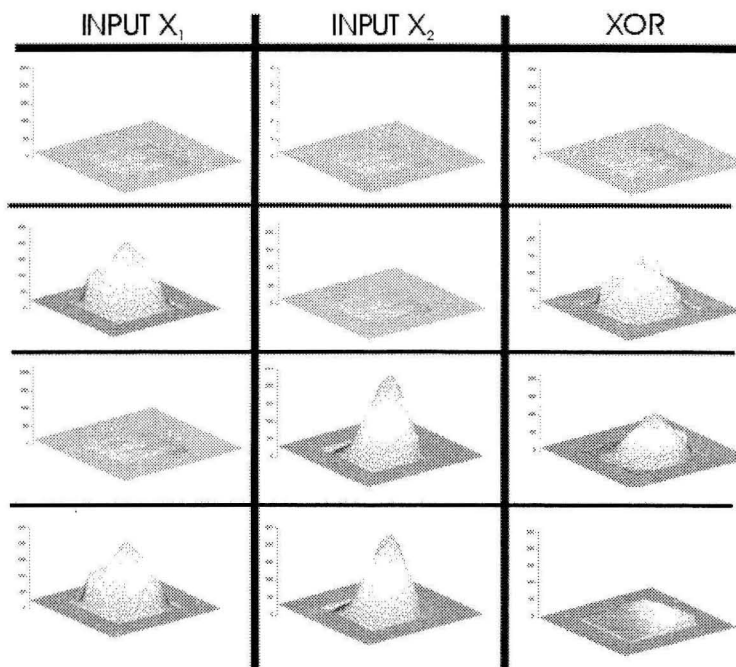


Figure 4.22: Experimental truth table of the optical XOR gate.

(130 fs) photoinduced exciton levels are generated close to the conduction band. As a result, photoinduced infrared absorption occurs from the exciton level. In experiments, researchers reported, at room temperature, 15% absorption increase within 10 fs and an absorption time decay equal to 130 fs [90]. This material is of interest for converting signals at a wavelength of 400 nm to 800 nm with fidelity. Assume that a long IR pulse is incident on the polymer at the same time as a blue stream of pulses (fig. 4.23). The visible pulses modulate the transmission of IR beam with ultra fast speed (< 600 fs), causing the IR pulse to be amplitude modulated. The result is an inverted stream of IR pulses with respect to the visible pulse stream (if the extinction is perfect). A NOT gate inverting an IR pulse back in the IR range requires a 2 stage process: first the IR is frequency doubled with collinear phase matching and then inverted by photoinduced absorption, as described above. An important parameter of the polymer is the magnitude of the photoinduced absorption. High photoinduced absorption is required to produce a NOT gate. Currently, 15% photoinduced absorption has been measured on PMBPA samples. The energy needed to produce the photoinduced absorption was reported to be $1000 \text{ photons/cm}^2$. With

a SHG conversion efficiency of 0.1% and 0.1 mJ/IR pulse, the beam area needed to produce 15% of photoinduced absorption is equal to 1.4 mm². This figure has to be improved both energetically and in the magnitude of the photoinduced absorption to be of practical use.

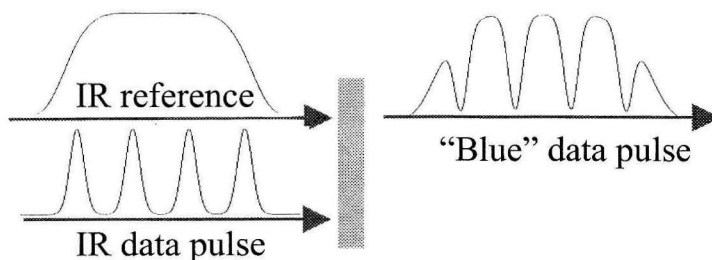


Figure 4.23: Amplitude modulation by photoinduced absorption.

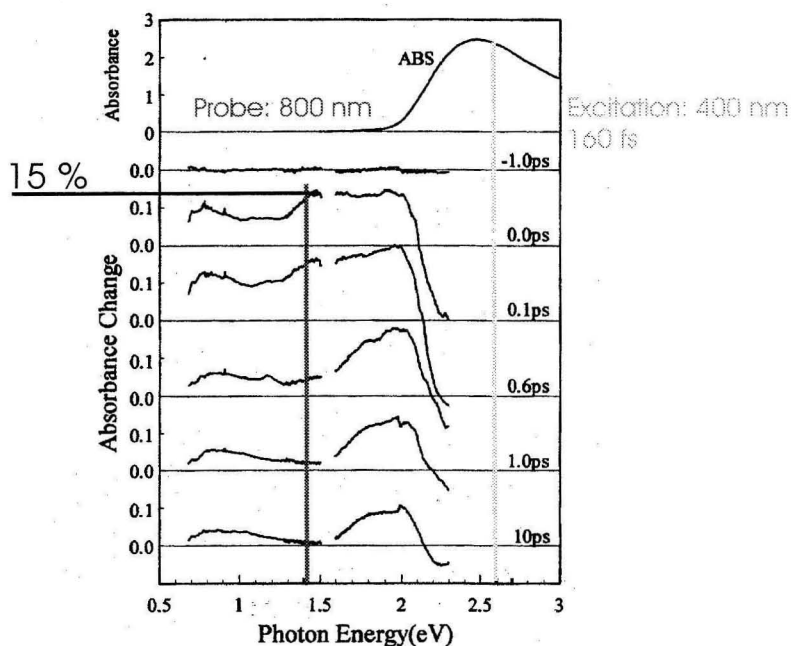


Figure 4.24: Relaxation time of photoinduced excitation in PMBPA polymers.

4.4.7 Optical computation

In semiconductors, each elementary gate needs a power supply in the form of a voltage source. For those optical gates, the reference power supply is a clocked stream

of pulses. The reference pulse stream is modulated by the frequency doubled output of previous stages through photoinduced absorption (see section 4) and becomes the input of the next gate. As an example of computing with this set of optical gates, an implementation of a 2 bits adder is presented.

We denote the two bit numbers to be added (A_0, A_1) and (B_0, B_1) . The bits are encoded spatially; therefore, we need four beams that encode the two numbers. The

$$\begin{array}{r} \text{Carry} \\ \text{Sum} \end{array} \begin{array}{|c} \hline C_2 C_1 \\ A_1 A_0 \\ B_1 B_0 \\ \hline S_2 S_1 S_0 \\ \hline \end{array} +$$

LSB S_0 is just an XOR between A_0 and B_0 . We use a single optical gate to compute the XOR of two inputs (see section 4.4.2) and the first carry C_1 is an AND between the inputs. This block is sketched in fig. 4.25 A).

The second carry C_2 (and the following carries if the number contains more than 2 bits) can be implemented with one gate as an OR of AND's: $C_2 = A_1 C_1 + A_1 B_1 + B_1 C_1$. This block is shown in fig. 4.25 B).

The block illustrated in fig. 4.25 computing XOR of 3 variables is needed to compute S_1 . Two XOR and inverting gates are needed:

$$\text{XOR}(A_1, B_1, C_1) = \text{XOR}(A_1, B_1) \overline{C_1} + C_1 \overline{\text{XOR}(A_1, B_1)}$$

The full adder is implemented in fig. 4.25 D) using the building blocks A), B) and C).

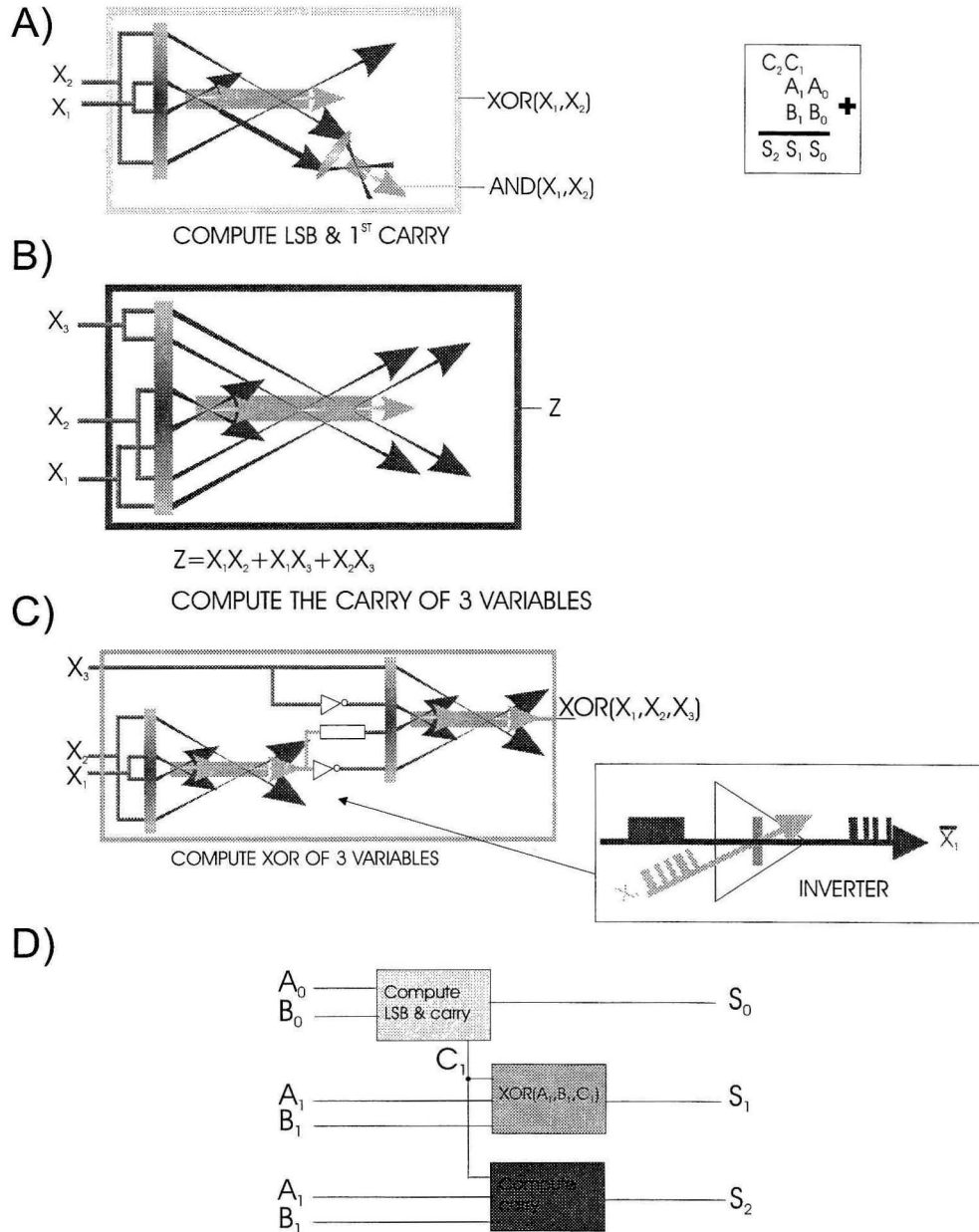


Figure 4.25: Implementation of a 2 bit adder using the optical gates developed in this section.

Chapter 5 Three-dimensional measurement using conoscopic patterns

5.1 Introduction

Many industries are constantly challenged with increasingly demanding requirements for the design, production and process control of surfaces and components. Measurement and control of the 3-D topography is critical in many applications to assure that components perform as intended. Optical metrology instruments are important in many fields where non-contact, high accuracy and short processing time are needed. Depending on the reflectance characteristic of the object to measure and/or the a-priori knowledge of its shape, several optical systems have been investigated. In holography, an interference pattern is formed between an object beam and a reference beam using a coherent light source. The interference pattern can be stored in the medium for further processing. A system based on matched filtering by a volume hologram acts as a modified confocal microscope without the need of a pinhole filter [91]. Instead of using the diffraction properties of holograms, we propose to process digitally the interference pattern generated by the propagation of light in a bi-refringtont crystal. These patterns are the so-called conoscopic patterns and contain information about the optical wavefront.

In this chapter, we start by developing the theory of the formation of conoscopic patterns. Two implementations of optical measuring sensors are described. They are both based on conoscopic patterns. The first sensor is a high accuracy non-contact profilometer. The profilometer measures the depth of a single point on a surface. The 3-D topography can be extracted by scanning the surface. A second sensor based on the same principle measures the wavefront of a field reflected from the surface under inspection. By knowing a-priori the surface shape, the 3-D topography can be

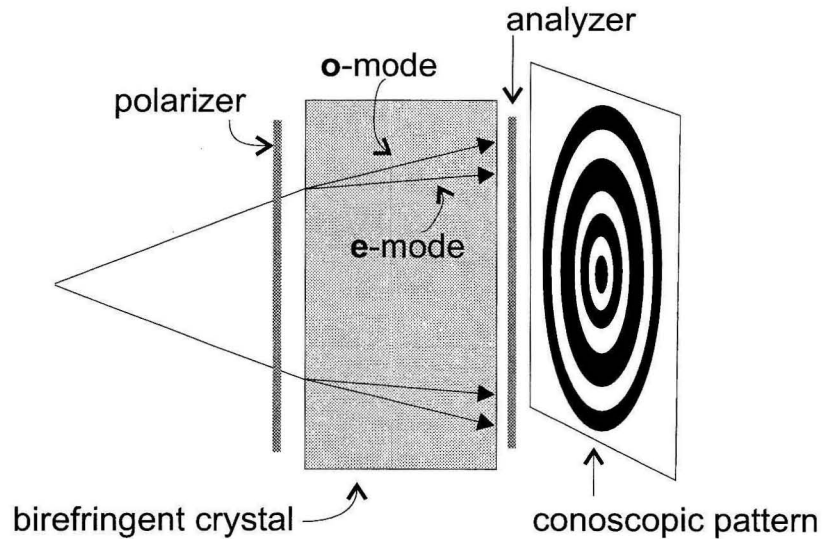


Figure 5.1: Interference between the ordinary and extraordinary rays in a birefringent crystal. The incident light is polarized. After the analyzer is placed at the output, the so-called conoscopic pattern is produced. The pattern consists of concentric disks of alternating low and high intensities.

extracted with sub-micrometer accuracy.

5.2 Theory

Conoscopic holograms [92, 93, 94, 95] are formed by the interference of the ordinary and extraordinary waves propagating in birefringent crystals. The birefringent crystal is illuminated by a linearly-polarized point source. Each ray entering the crystal is refracted into two rays, called the ordinary ray (**o**-ray) and the extraordinary ray (**e**-ray). This phenomenon can be understood by decomposing the incident electric field into the eigenmodes **o** and **e** of the crystal. The velocity of the **o**-mode is constant, determined by the ordinary index of refraction n_o . The velocity of the **e**-mode is dependent on the angle of propagation, because $n_e(\alpha)$, the extra-ordinary index of refraction, depends on the propagation angle α of the ray. As an example, the trajectories of two rays are drawn separately in Fig. 5.1.

Each one of rays 1 and 2 divide into their **o**- and **e**- modes. If the spatial separation

of rays 1 and 2 (measured on the entrance face of the calcite) is correct, the **o**-mode coming from ray 1 combines with the **e**-mode from ray 2. The two modes are mixed using an analyzer, and an interference pattern forms. The conoscopic figure of a point source looks like a Fresnel zone plate with a superimposed cross (bright or dark, depending on the analyzer orientation) parallel to the eigenaxes. The cross is eliminated using circularly polarized light.

Let $G(x)$ be the path difference between the interfering beams and x be the radial distance from the optical axis. The intensity after the polarizer is given by:

$$I(x) = \frac{I(0)}{2} \left[1 + \cos \left(\frac{2\pi G(x)}{\lambda} \right) \right] \quad (5.1)$$

To calculate the interference pattern, one needs to calculate $G(x)$, which is determined by the geometry. The calculation for normal incidence geometry is given in [92] and will not be repeated here.

Of particular interest for applications is the slope of $G(x)$, because it determines the fringe size. The slope depends on the parameters f and Δf (among others). If all other parameters are fixed, the defocus Δf can be determined by counting the number of fringes that fit in a fixed aperture. One way to increase the depth resolution is to tilt the crystal, because this increases the pathlength difference inside the birefringent material. In the following section, we derive $G(x)$ in the general tilted crystal geometry.

5.2.1 Path difference in the tilted crystal geometry

In the modified configuration shown in fig. 5.2, a lens is placed between the point source and a tilted crystal at an angle ψ . When the point source is located one focal length f behind the lens, the beam is collimated and the path difference $G(x)$ is constant everywhere, so the interference pattern $I(x)$ contains just one big fringe. A defocus Δf of the point source decollimates the beam and causes the path difference to vary with the location of the observation point x in the detection plane. Because of the variable path difference, a linear fringe pattern appears after the polarizer.

energy propagation (defined by the Poynting vector) is perpendicular to the electric field \mathbf{E} . Because of the tensorial nature of $\overleftrightarrow{\epsilon}$, the fields \mathbf{D} and \mathbf{E} for the \mathbf{e} -mode are not parallel, and hence energy and phase are not collinear. Snell's law determines the direction ϕ_e of phase propagation, but the direction of energy propagation ϕ_E needs a correction according to the law:

$$\tan \phi_E = \frac{n_o^2}{n_e^2} \tan \phi_e. \quad (5.5)$$

(iv) The wave illuminating the crystal after going through the collimating lens is described by a quadratic phase:

$$E(x, y, z) = \hat{e}_0 \exp \{ikz\} \exp \left\{ ik \frac{x^2 + y^2}{2} \left(\frac{1}{z} - \frac{1}{f} \right) \right\}. \quad (5.6)$$

The path difference is calculated as follows: First, a point x is chosen on the output face of the calcite. Then, the incident angles of propagation, θ_e and θ_o , of the two rays converging at x are calculated by numerically solving the equations:

$$\theta_o = \frac{\left(x - L \frac{\sin(\psi - \theta_o)}{\sqrt{n_o^2 - \sin^2(\psi - \theta_o)}} \right) \cos \psi}{f \left(1 + \frac{f}{\Delta f} \right) - a - \left(x - L \frac{\sin(\psi - \theta_o)}{\sqrt{n_o^2 - \sin^2(\psi - \theta_o)}} \right) \sin \psi}, \quad (5.7)$$

$$\theta_e = \frac{\left(x - L \frac{n_o}{n_e} \frac{\sin(\psi - \theta_e)}{\sqrt{n_e^2 - \sin^2(\psi - \theta_e)}} \right) \cos \psi}{f \left(1 + \frac{f}{\Delta f} \right) - a - \left(x - L \frac{n_o}{n_e} \frac{\sin(\psi - \theta_e)}{\sqrt{n_e^2 - \sin^2(\psi - \theta_e)}} \right) \sin \psi}. \quad (5.8)$$

The parameter a denotes the distance between the lens and the front face of the crystal (fig. 5.2). Let x'_e and x'_o denote the input points of the two rays (from the geometry it follows that $x'_o > x'_e$). The spherical wavefront passing through x'_e (point

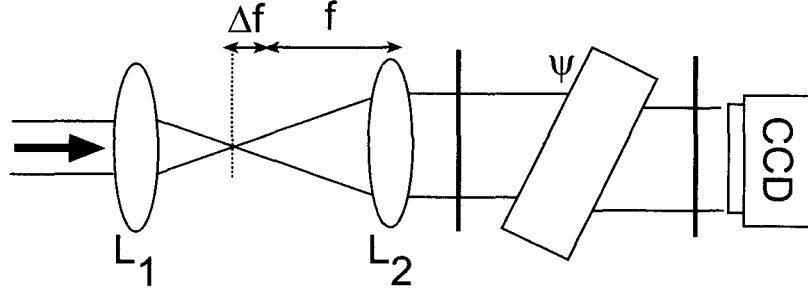


Figure 5.3: Experimental measurement set-up of the path difference $G(x)$ described by eqn. 5.10.

B) determines the surface of equal phase. The path difference $G(x)$ (fig. 5.2) is the difference between the length of segment (BD) and the sum of segments (CD) and (AC)= Δl . Expressed in optical path units, this is

$$G(x) = L \left(\frac{n_e(\phi_e) \cos(\phi_e - \phi_E)}{\cos \phi_E} - \frac{n_o}{\cos \phi_o} \right) - \Delta l. \quad (5.9)$$

The final result for the path difference is

$$G(x) = Ln_o \left(\frac{n_e}{\sqrt{n_e^2 - \sin^2(\psi - \theta_e(x))}} - \frac{n_o}{\sqrt{n_o^2 - \sin^2(\psi - \theta_o(x))}} \right) - L \left(\frac{n_o \sin(\psi - \theta_e(x))}{n_e \sqrt{n_e^2 - \sin^2(\psi - \theta_e(x))}} - \frac{\sin(\psi - \theta_o(x))}{\sqrt{n_o^2 - \sin^2(\psi - \theta_o(x))}} \right) \times \left\{ \sin \psi + \frac{\Delta f \cos^2 \psi}{2f(f + \Delta f)} \left[L \left(\frac{n_o \sin(\psi - \theta_e(x))}{n_e \sqrt{n_e^2 - \sin^2(\psi - \theta_e(x))}} + \frac{\sin(\psi - \theta_o(x))}{\sqrt{n_o^2 - \sin^2(\psi - \theta_o(x))}} \right) - 2x \right] \right\}. \quad (5.10)$$

The theoretical path difference expressed by eqn. 5.10 is tested with the following experiments. The point source is generated by focusing a parallel beam of light using lens L_1 as shown in fig. 5.3. The lens L_2 collimates the point source. A CCD camera

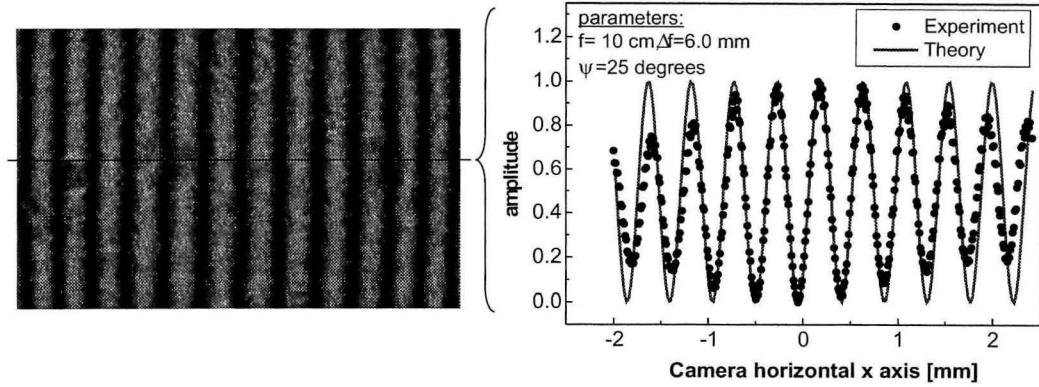


Figure 5.4: Conoscopic pattern produced by the set-up of fig. 5.3. A cross section of the conoscopic pattern is shown to fit with theory.

with 760×494 pixels ($8.4 \times 9.8 \mu\text{m}$ pixel size) is placed after a calcite crystal of length 3.7 cm sandwiched between two crossed-polarizers. The defocus Δf is produced by translating the first lens L_1 using a micrometer stage. The c-axis of the crystal is perpendicular to the facets (i.e., along the z-axis). In this experiment, the following parameters are used:

- a) wavelength = 532 nm, collimating lens L_2 of focal length $f=10\text{cm}$, crystal tilt angle $\psi = 25^\circ$, defocus $\Delta f = 6.02$ mm.
- b) $\lambda = 532$ nm, $f = 10$ cm, $\psi = 13^\circ$, $\Delta f = 4.0$ mm.

The image is digitized by a frame grabber and produces a sinusoidal pattern. A one-dimensional sinusoidal pattern is generated by averaging 50 rows in the image as shown in figs. 5.4 and 5.5. The experimental data agrees very well with theory.

5.2.2 Analytical expression of the path difference

In this section, we linearize eqn. 5.10 describing the path difference. The simplified expression for the path difference allows us to determine analytically the influence of several parameters on the depth resolution. Under the approximation $\Theta_o, \Theta_e \ll \Psi$

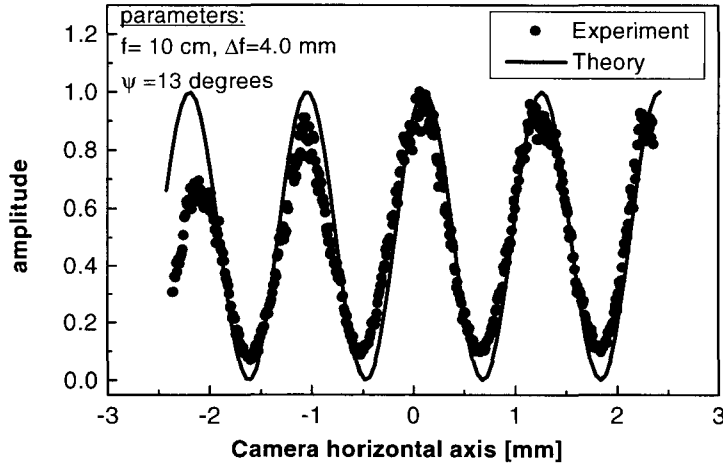


Figure 5.5: A cross section of the conoscopic pattern is shown to fit with theory.

and $\frac{\Delta f}{f} \ll 1$, the first-order development of eqn. 5.7 and 5.8 yields:

$$\theta_o \simeq \frac{\Delta f \cos \Psi}{f^2} \left(x - \frac{L \sin \Psi}{\sqrt{n_o^2 - \sin^2 \Psi}} \right). \quad (5.11)$$

$$\theta_e \simeq \frac{\Delta f \cos \Psi}{f^2} \left(x - \frac{L n_o \sin \Psi}{n_e \sqrt{n_e^2 - \sin^2 \Psi}} \right). \quad (5.12)$$

The path difference $G(x)$ takes on a particularly simple form:

$$G(x) = x \frac{\Delta f L}{f^2} C(\Psi) \quad (5.13)$$

where $C(\Psi) = \sin \Psi \cos^2 \Psi \left(\frac{n_o}{n_e \sqrt{n_e^2 - \sin^2 \Psi}} - \frac{1}{\sqrt{n_o^2 - \sin^2 \Psi}} \right)$

The path difference approximation computed from eqn. 5.13 and the exact solution computed from eqn. 5.10 are plotted in figs. 5.6 and 5.7. Theory shows very good agreement with experimental measurements for small defocus (typ. $\Delta f/f < 2$ percent).

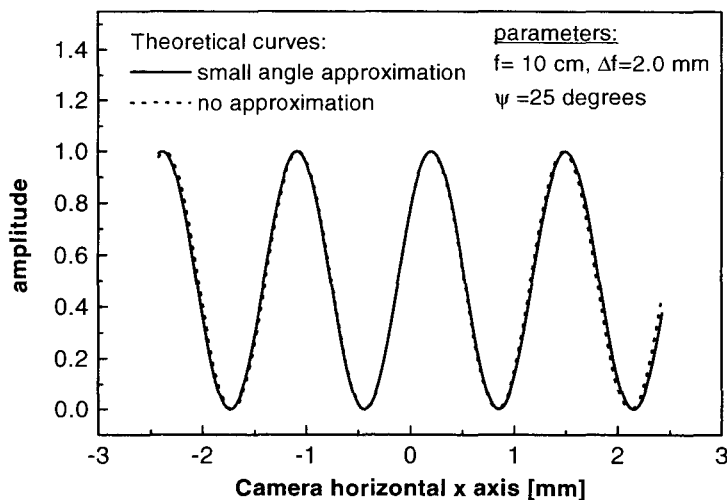


Figure 5.6: Plots of the path difference using the approximation (eqn. 5.13) and the exact expression (eqn. 5.10) for a crystal tilt angle of 25 degrees .

5.3 Profilometer

The results of section 5.2 suggest that depth information can be inferred from the conoscopic pattern. An optical non-contact profilometer is an instrument that extracts the 3-D shape of an object, point by point, by scanning a spot of light on the object [97, 98]. The simple system illustrated in fig. 5.3 serves as an absolute non-contact profilometer. In this section, we determine analytically and verify experimentally the performance of a profilometer. From eqn. 5.13, the amount of path difference $G(x)$ is proportional to the amount of defocus Δf . Thus by counting the number of fringes in the conoscopic pattern, the amount of defocus Δf , i.e., the depth, can be inferred. This method gives an absolute distance measurement.

We are interested in determining the depth accuracy of the profilometer. At the exit of the crystal and analyzer, the distance Δx between consecutive fringes is solved

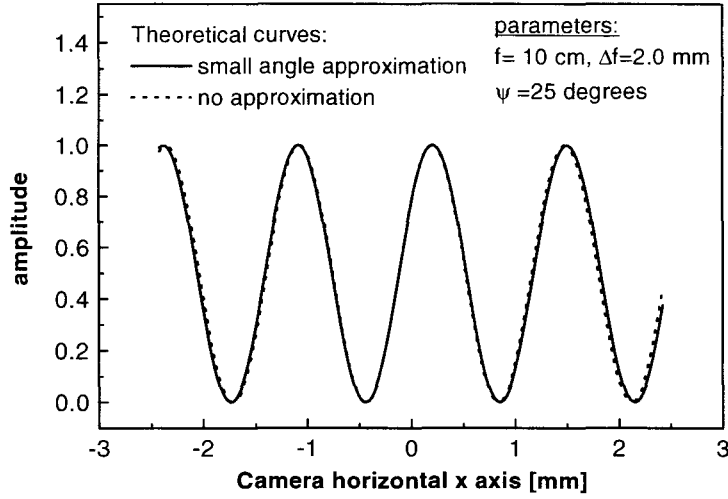


Figure 5.7: Plots of the path difference using the approximation (eqn. 5.13) and the exact expression (eqn. 5.10) for a crystal tilt angle of 35 degrees.

by setting the path difference $G(x)$ equal to λ :

$$\Delta x = \frac{\lambda f^2}{\Delta f LC(\Psi)}. \quad (5.14)$$

The total number of fringes N , in the conoscopic pattern grabbed by the camera, is equal to $N = \frac{q}{\Delta x}$, where q is the aperture of the conoscopic pattern. q can be computed using eqns. 5.11 and 5.12:

$$q = \frac{f}{f_{\#} \cos \Psi} - L \sin \Psi \left(\frac{n_o}{n_e \sqrt{n_e^2 - \sin^2 \Psi}} - \frac{1}{\sqrt{n_o^2 - \sin^2 \Psi}} \right) \quad (5.15)$$

where $f_{\#}$ is the f-number of the collimating lens. The aperture q is greater than zero, which gives a condition to the parameters L , f , $F_{\#}$, ψ :

$$L < \frac{f \cos(\psi)}{F_{\#} C(\psi)} \quad (5.16)$$

We set the depth resolution δz to be the distance that causes the number of fringes

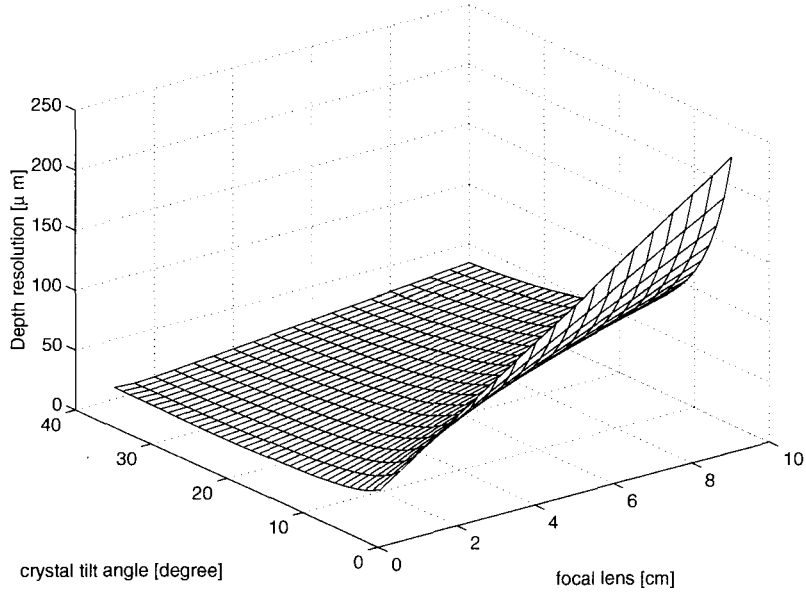


Figure 5.8: Depth resolution of the scanning conoscopic system as a function of the crystal tilt angle and the focal length of the collimated lens.

in the conoscopic pattern to increase by 1:

$$\delta z = \frac{\lambda f^2}{\left(\frac{f}{f_{\#}} - L \frac{C(\Psi)}{\cos \Psi}\right) L \frac{C(\Psi)}{\cos \Psi}} \quad (5.17)$$

For example, a system with $f = 5$ cm, $f_{\#} = 2.0$, $L = 3.7$ cm, $\lambda = 532$ nm and tilt angle $\Psi = 25^\circ$ yields a depth resolution $\delta z = 25.7$ μm.

From eqn. 5.17, we can derive the optimum parameters to obtain maximum depth resolution. The optimum crystal length is obtained by fixing the crystal tilt angle and focal length and taking the derivative of 5.17 with respect to L :

$$L = \frac{f \cos(\psi)}{2F_{\#} C(\psi)}. \quad (5.18)$$

Eqn. 5.18 satisfies condition 5.16. In a similar calculation, the optimal focal length f and tilt angle ψ yield the same expression as eqn. 5.18. The function $D(\psi) = \frac{C(\psi)}{\cos(\psi)}$ is plotted in fig. 5.10. This function reaches a maximum value of 0.1 at $\psi = 53.1^\circ$ (at

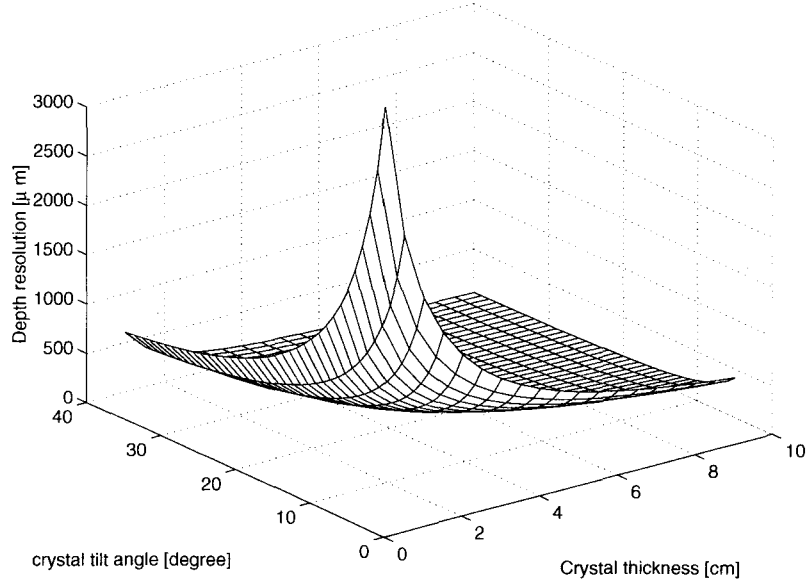


Figure 5.9: Depth resolution of the scanning conoscopic system as a function of the crystal tilt angle and the crystal thickness.

$\lambda = 632.8$ nm). The parameters f , L , $F_{\#}$ and ψ yielding maximum depth resolution are related to each other by expression 5.18. The optimal depth resolution is found by substituting eqn. 5.18 into eqn. 5.17 giving:

$$\Delta z_{optimal} = \frac{\lambda}{4} F_{\#}^2. \quad (5.19)$$

The optimal depth resolution varies as the square of the lens $F_{\#}$. However, for eqn. 5.19 to be valid, the other parameters must satisfy eqn. 5.18. For example, choosing $F_{\#}=1$ and $f = 2$ cm would require a crystal thickness of 10 cm. With a smaller focal length such as $f = 2$ mm, the crystal thickness is reduced to 1 cm. The maximum depth range is limited by the camera pixel size b . We set the minimum fringe size to be twice the pixel size: $\Delta x \geq 2b$. Δx is given by eqn. 5.14. The maximum depth range z_{max} is given by:

$$z_{max} \leq \frac{\lambda f^2}{LC(\psi)2b}. \quad (5.20)$$

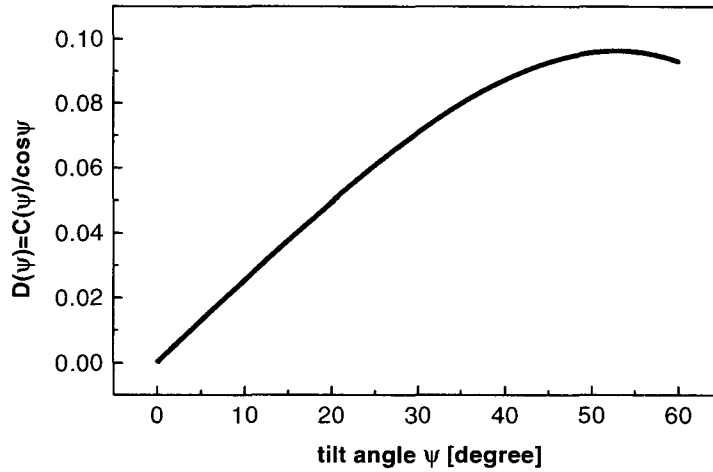


Figure 5.10: Function $D(\psi) = \frac{C(\psi)}{\cos(\psi)}$ versus crystal tilt angle ψ .

The space bandwidth product defined by $SBP = \frac{z_{max}}{z_{min}}$ is equal to:

$$SBP = \frac{f}{4b \cos(\psi) F_{\#}} \quad (5.21)$$

where the parameters are related by eqn. 5.18.

5.3.1 Fringe interpolation

Higher resolution can be obtained by interpolating the fringes of the conoscopic pattern. We present an interpolation method that is robust to noise in the interferogram. A reference interferogram such as the one displayed in fig. 5.5 is grabbed by the CCD camera and normalized between 0 and 1. The interferogram obtained after a defocus $\delta(\Delta f)$ is also normalized between 0 and 1 and then subtracted from the reference interferogram. The resulting difference-interferogram is shown in fig. 5.11. Theory (solid lines) and experimental values (black circles) agree very well. The shape of the subtracted interferogram is explained as follows: The path difference $G(x)$ is proportional to both the defocus Δf and the distance x from the optical axis of the

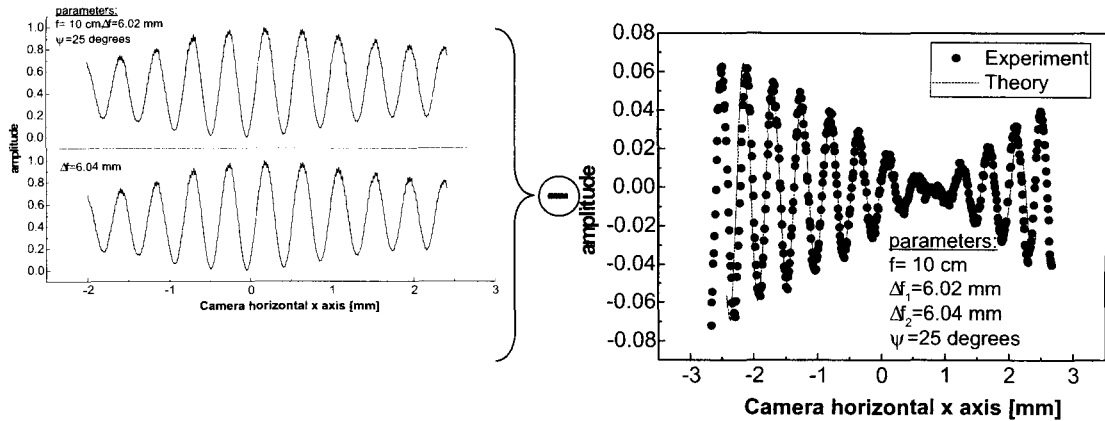


Figure 5.11: Fringe interpolation by subtraction of two translated interferograms.

system. Therefore, along the optical axis of the system ($x=0$), there is no variation upon defocus and for all other points on the x axis, the path difference increases linearly resulting in a modulated interferogram.

The modulation amplitude of the subtracted interferogram increases as the defocus increases as shown in fig. 5.12. We measure the amplitude modulation by the slope computed by linear regression of the first 3 maximas of the subtracted interferograms (black circles in fig. 5.12). For this measurement, a resolution better than 10 micrometers could be obtained with a large focal length and $F_{\#}(10 \text{ cm}, F_{\#}=5)$.

5.3.2 Application: corneal curvature change

The profilometer described in this chapter can be applied to measure the spherical curvature of reflective objects. A particularly interesting application is the measurement of the corneal curvature change during eye surgery (see chapter 6 for detailed explanation). Fig. 5.13 illustrates the set-up for curvature measurement. The measurement procedure effectively determines the overall spherical curvature of the object in the direction of the crystal tilt.

In this experiment, a plastic (PMMA) replica of a human cornea is taken as the object. Its radius of curvature is 7.8 mm. The focal length of the collimating lens is 5 cm which is a working distance large enough for the eye mapper to be integrated

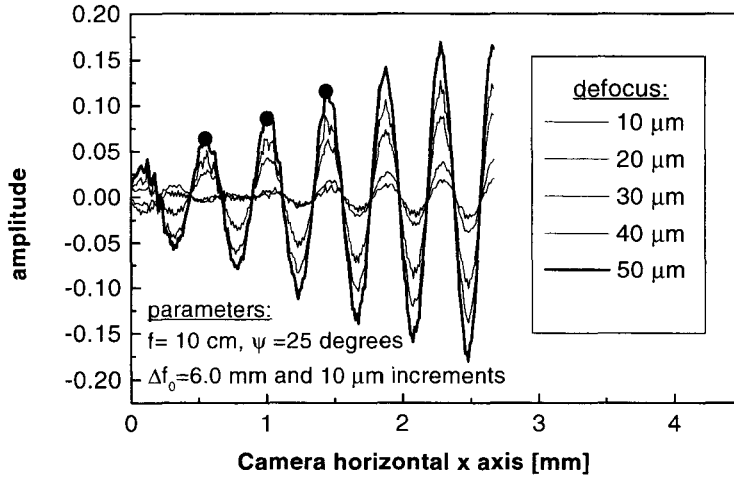


Figure 5.12: Subtracted interferograms with increasing defocus.

under an eye surgery laser. The crystal tilt is 25 degrees. The $F_{\#}$ of the lens is 2.5. To simulate a change in curvature (obtained by cornea ablation in the procedure), the plastic cornea is placed on a micrometer controllable stage ($0.1 \mu\text{m}$ resolution) which translates the object in the direction of the optical axis of the system. A shift δz of the plastic cornea effectively produces a defocus change $\delta(\Delta f)$:

$$\delta(\Delta f) = \left(\frac{1}{(f - z_o)^2 \left(\frac{2}{R} - \frac{1}{f - z_o} \right)^2} + 1 \right) \delta z. \quad (5.22)$$

where $\delta(\Delta f)$ is the defocus change due to a shift δz of a spherical surface placed at a distance z_o from the lens of focal length f . Similarly, a change of curvature ΔR of a spherical surface of radius R illuminated by a beam of diameter D introduces a defocus change equal to:

$$\delta(\Delta f) = \frac{1}{R^2 \left(\frac{2}{R} - \frac{1}{f - z_o} \right)^2} \Delta R. \quad (5.23)$$

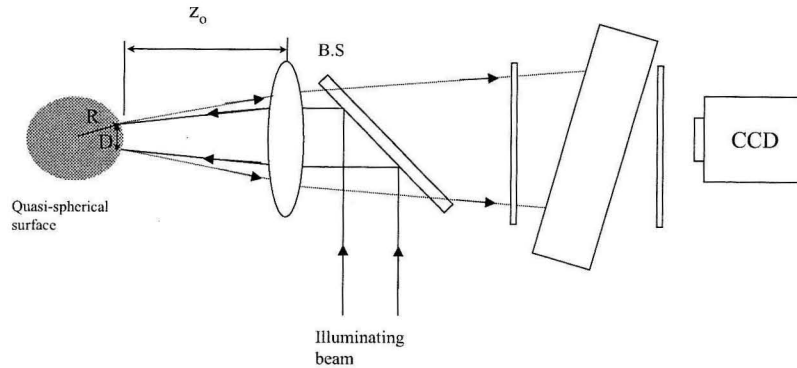


Figure 5.13: Curvature measurement set-up.

Ophthalmologists prefer to use units of diopters change ΔD instead of radius of curvature change ΔR . The relation between these two quantities is $\Delta R = \frac{\Delta D}{\Delta n} R^2$, where Δn is the change of refractive index. The working distance between a measuring system and a human eye *in vivo* is typically several centimeters. This constraint limits the focal length of the lens to a minimum of 5 cm. The radius of curvature of the human cornea is approximately 7.8 mm. The relation between the depth change δz and the defocus change $\delta(\Delta f)$ is computed by eqn. 5.22. The numerical result gives $\delta(\Delta f) = 1.58 \delta z$. The distance is coded as the slope of the modulated envelope as described in section 5.3.1. Fig. 5.14 shows the results of the measurements with error bars obtained from 10 separate measurements. The experimental results show that a shift δz of $2 \mu\text{m}$ can be detected which means that this system can resolve a defocus change $\delta(\Delta f)$ of $3.1 \mu\text{m}$. From eqn. 5.23, this resolution results in a detectable diopter change equal to 0.015 diopters. Measurement accuracy of 0.2 diopter is considered enough by ophthalmologist to yield 20/20 vision. The method described is capable of detecting the overall variation of radius of curvature with enough accuracy. However, this method gives no information about the topography. In the next section, a wavefront sensor is developed that overcomes this limitation.

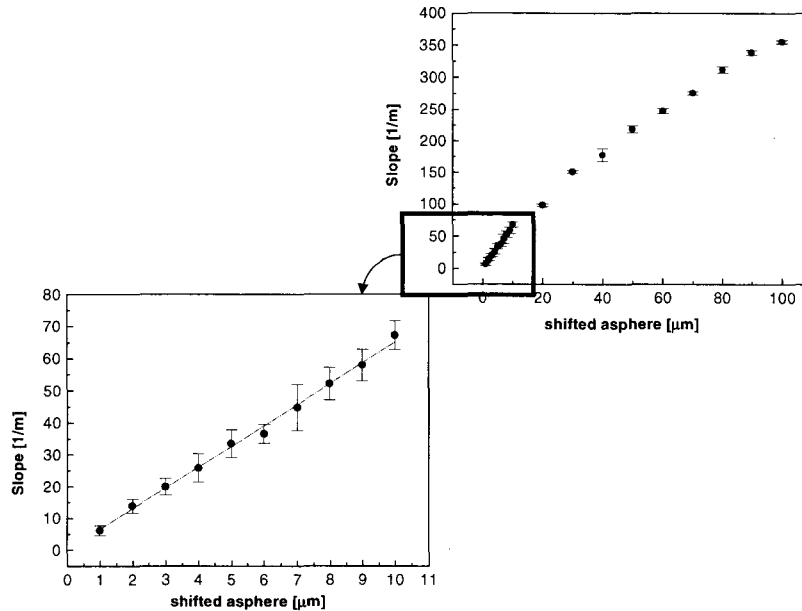


Figure 5.14: Experimental measurement of curvature change by translating a plastic cornea.

5.4 3-D measurements using shear conoscopy

5.4.1 Introduction

Optical devices capable of measuring an entire optical wavefront at once are used for fast testing of optical components. Several interferometer systems based on Sagnac, Fizeau and Michelson design are routinely used by manufacturers of optical components because of their very high accuracy. We concentrate here on an ophthalmologic application which could not be solved by the standard optical testing systems mentioned above. The challenge is to measure the topography of a human cornea *in vivo* while its surface is ablated during a laser correction procedure. The environmental conditions during the procedure are such that standard interferometers are not robust enough to vibrations and air fluctuation. Several systems have been

investigated for that purpose, reaching only a moderate level of success.

A simple lateral-shearing interferometer has been developed. The shearing mechanism is based on the double refraction at the interface of a birefringent crystal. The shear interferometer is little affected by mechanical vibrations and air turbulence because the beam splitting and recombining take place within a birefringent crystal. A phase-reconstruction method for wavefront analysis in lateral shearing interferometry is presented. Hermite polynomial functions describe the differential wavefronts and are related to Hermite polynomial functions of the original wavefront. This method is recursive and does not require a matrix inversion as it is required for other polynomial decompositions [99]. Hermite polynomial decomposition is therefore computationally very efficient. A plastic aspherical surface modeled after a human cornea is measured with the shear interferometer. The aspherical surface was also measured by a Twyman-Green interferometer to compare the error with that measured by the lateral-shearing interferometer. The experimental results agreed well with those measured by the lateral-shearing interferometer.

5.4.2 Phase extraction from a shear interferogram

A wavefront is generated using the set-up of fig. 5.13. The spherical or aspherical surface is placed in the field of view of a collimating lens. The distance between the surface under inspection and the collimating lens is adjusted such that the reflected wavefront is captured by the lens and collimated towards the birefringent crystal. By measuring the wavefront distortion, the topography of the surface can be inferred. The wavefront incident on the crystal, tilted around the y -axis, is split into the e -mode and the o -mode, producing two copies of the wavefront shifted by a distance h as shown in fig. 5.15. After the analyzer, the two wavefronts $\phi(x, y)$ and $\phi(x + h, y)$ corresponding to the e -mode and o -mode, respectively, interfere and generate a shear interferogram written as:

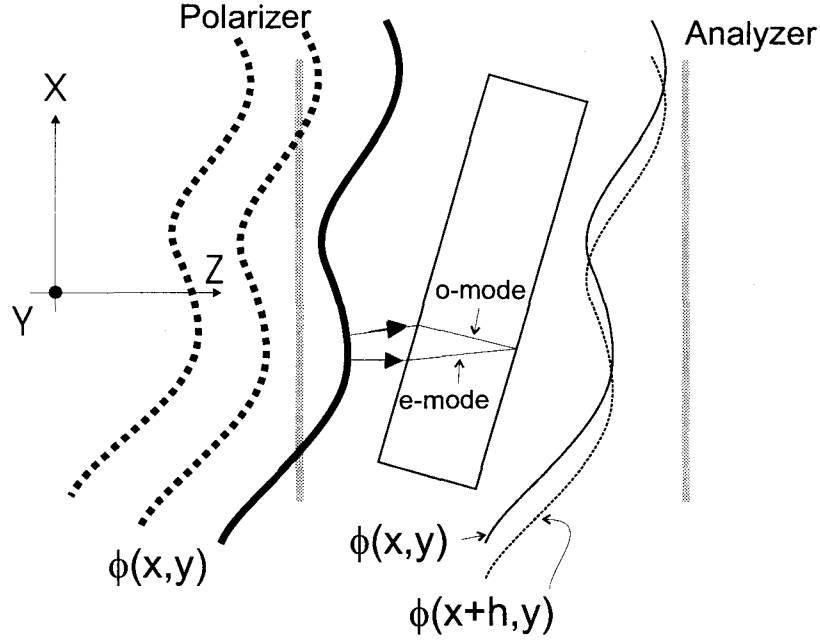


Figure 5.15: The incident wavefront is laterally sheared by double refraction in a birefringent crystal.

$$I(x) = I_b (1 + \gamma \cos \{w(x, y) + \text{const.}\}) \quad (5.24)$$

$$w(x) = \phi(x + h, y) - \phi(x, y). \quad (5.25)$$

where I_b is the mean light intensity and γ is the modulation depth. h is the constant lateral shear produced by double refraction. Eqn. 5.25 is valid provided that the lateral shear h does not vary appreciably along the wavefront. The lateral shift h depends on the incident angles Θ_o and Θ_e and the crystal tilt angle as:

$$h = L \cos \psi \left(\frac{no}{nne} \frac{\sin(\psi - \theta_e)}{\sqrt{nne^2 - \sin^2(\psi - \theta_e)}} - \frac{\sin(\psi - \theta_o)}{\sqrt{no^2 - \sin^2(\psi - \theta_o)}} \right). \quad (5.26)$$

We derived this equation by assuming that the c-axis is oriented along the direction orthogonal to the optical axis of the system. The mathematical relations developed earlier in this chapter are still valid. Only the indices of refraction need to be changed

($n_o \rightarrow n_e, n_e \rightarrow n_o$).

Phase extraction is more complicated than a simple inversion of the cosine in eqn. 5.25, because of possible non-uniformities in $I_b(x, y)$ and unknown γ . We use a conventional phase-shifting method to extract the phase [?]. This method requires five intensity measurements of the same interference pattern:

$$I_{\Delta\omega=0}(x, y), I_{\pi/2}(x, y), I_{\pi}(x, y), I_{3\pi/2}(x, y), I_{2\pi}(x, y). \quad (5.27)$$

These five patterns are generated by successively tilting the crystal by an angle:

$$\Delta\psi \approx \frac{n_o^2 n_e}{n_e^2 - n_o^2} \frac{\lambda}{4L\psi}$$

between measurements, where ψ is the initial tilt angle, λ is the wavelength of the monochromatic light and L is the length of the crystal in the direction of the optical axis of the system. The phase difference $w(x, y)$ is obtained from:

$$w(x, y) = \arctan \left(\frac{2(I_{\pi/2}(x, y) - I_{3\pi/2}(x, y))}{I_0(x, y) + I_{2\pi}(x, y) - 2I_{\pi}(x, y)} \right). \quad (5.28)$$

Figs. 5.16 shows the five phase shifted interferograms. The result of the extracted phase difference $w(x, y)$ computed from eqn. 5.28 is shown in fig. 5.17.

The original wavefront $\phi(x, y)$ is extracted from the measured wavefront difference $w(x, y)$ by decomposing $w(x, y)$ into Hermite polynomial expansion. For simplicity, the method is described for a one-dimensional wavefront $\phi(x)$. The generalization for

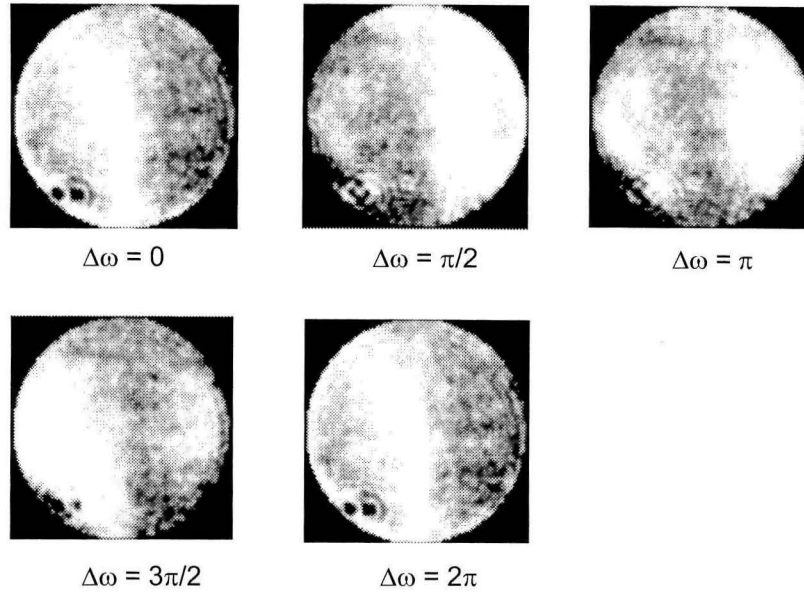


Figure 5.16: Five phase shifted conoscopic interferograms.

two dimensions follows trivially. The decomposition is as follows:

$$\begin{aligned}
 \phi(x) &= \sum_{j=1}^J b_j H_j(x) \\
 w(x) &= \sum_{j=0}^J b_j [H_j(x+h) - H_j(x)] \\
 &= \sum_{j=0}^{J-1} c_j H_j(x).
 \end{aligned}$$

The order of the polynomial should be taken from some a priori knowledge of the surface. The coefficients $c_j (j = 0, \dots, J-1)$ are determined directly by projecting $w(x)$ onto the basis of Hermite polynomials. The coefficients $b_j (j = 1, \dots, J)$ are computed from the coefficients c_j using a property of the Hermite polynomials:

$$H_j(x+h) - H_j(x) = \sum_{k=0}^{j-1} \binom{j}{k} (2h)^{j-k} H_k(x).$$

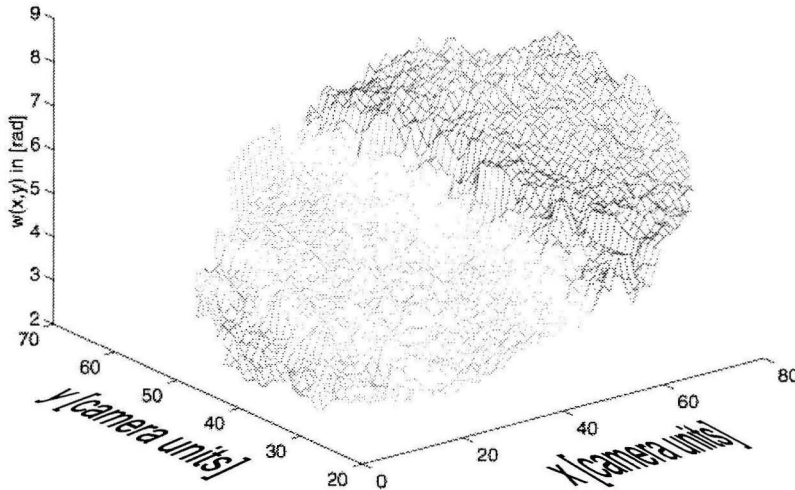


Figure 5.17: Phase difference $w(x, y)$ computed with the phase shifting method.

The b_j 's are then obtained using the recursive formula:

$$b_J = \frac{c_{J-1}}{2Jh}, \quad (5.29)$$

$$b_j = \frac{1}{2jh} \left[c_{j-1} - \sum_{k=j+1}^J \binom{k}{j-1} (2h)^{k-j+1} b_k \right]. \quad (5.30)$$

Note that b_0 , representing uniform translation along the optical axis, remains undetermined, because the DC information is lost during the shear process.

The surface under inspection is an asphere modeled after a human cornea made out of PMMA (plastic). The experiment is performed with the set-up of fig. 5.13. The measured area on the test surface is $4mm^2$. This area can be increased if a bigger aperture lens is used. The wavefront difference shown in fig. 5.17 is decomposed into two-dimensional hermite polynomials up to degree six. Higher degree polynomials did not improve the results. The components of the original wavefront are then computed recursively using eqn. 5.30. The result of the original wavefront reconstruction is shown in fig. 5.18. The same wavefront is measured with a Twyman-Green interferometer and subtracted from the measurement performed with the shear in-

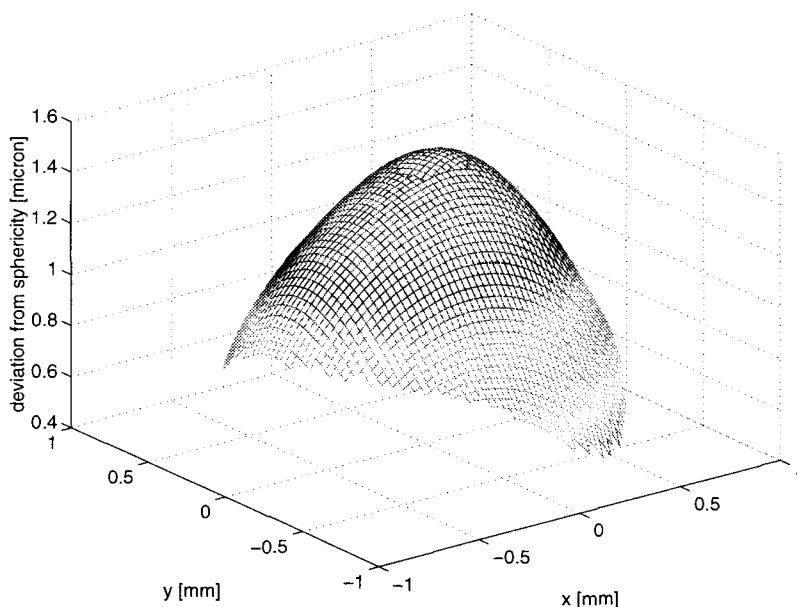


Figure 5.18: 3-D extraction of an aspherical surface using the shear lateral interferometer and the hermite polynomial expansion. The plot shows the wavefront reconstruction.

terferometer. The result is shown in fig. 5.19. We observe deviations of $\pm 0.1 \mu\text{m}$ between the two measurements.

Experiments were performed on a pig's eye *in vitro*. The surface of the eyes were rough because the epithelial layer is destroyed when it is not constantly humidified. The light from a He-Ne laser produced speckles by reflection off the eye's surface. The poor quality of the interferogram did not allow further processing. In the next chapter, a method based on feature projection yielded better results for the particular application of corneal mapping.

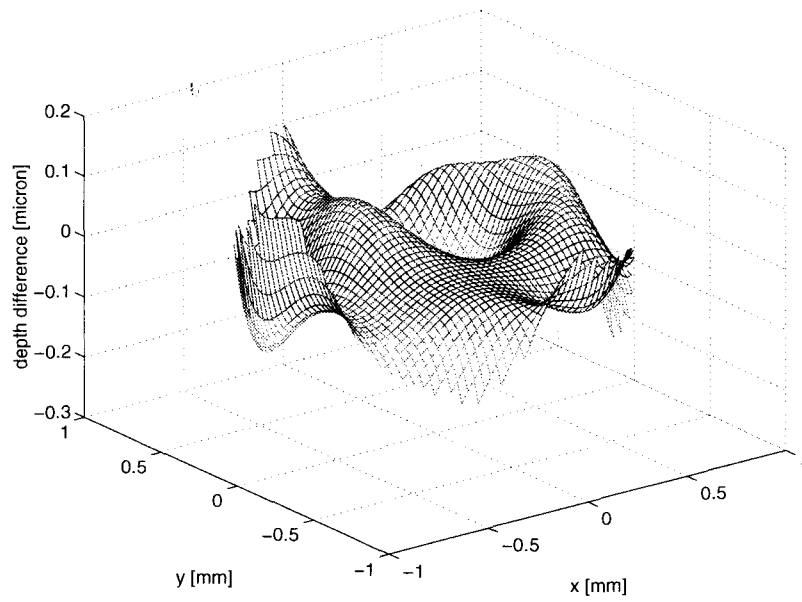


Figure 5.19: Measured wavefront difference between the lateral shear interferometer and the Twyman-Green interferometer.

Chapter 6 Feasibility study of Intraoperative Corneal Topography Monitoring During Photorefractive keratectomy

6.1 Introduction

We propose a feasibility study of a new corneal topography technology with the aim of monitoring intraoperative corneal topography during Excimer laser keratectomy (PRK). PRK is a laser-based vision correction procedure. An interesting topographer for PRK [101, 102] is the PAR system, which uses a single grid projection and triangulation [103, 104]. Unfortunately, this topographer requires fluorescent fluid to be deposited on the corneal surface for shape extraction. We propose and demonstrate a corneal topographer based on feature projection as well but that does not require additional fluid. We use a binary liquid crystal spatial light modulator (SLM) to display multiple fringe patterns onto the cornea. The topography is retrieved by digitally processing the fringes with an algorithm based on triangulation. The depth accuracy of the topographer is measured using a white reflected test sphere mounted on a micrometer translation stage. The performance of the topographer is tested on de-epithelialized swine eyes *in vitro* ablated by a PRK laser. The depth accuracy on the test sphere is $0.5 \mu\text{m}$ and standard deviation is $0.75 \mu\text{m}$ over an area of 17.6 mm^2 . On swine de-epithelialized cornea, ablation at the apex of the cornea treated with an excimer laser can be measured without addition of fluorescein. The topographer achieves an adequate level of accuracy on a test sphere. We demonstrate that it is feasible to measure de-epithelialized cornea without addition of fluorescent fluid.

The blurring effect of images reflected by corneas produces noise in the measurement. This effect hinders the topographer from improving the reliability of the Excimer laser surgery.

6.2 Material and methods

We propose to further improve the reliability of PRK surgery by monitoring the shape of the cornea while it is ablated, thus removing uncertainty due to the variable ablation rate of corneas and laser power fluctuations. Non-contact optical corneal topography methods can be classified in three different groups corresponding to the degree of light coherence:

- Coherent light measuring methods use interference between a reference wave and a wave reflected from the surface under inspection to extract the topography. An example of a robust interferometer for eye topography is presented in chapter 5. While giving sub-micrometer depth accuracy, coherent light gives speckles (grainy images) which are produced by surfaces with roughness on the order of a wavelength of light. A de-epithelialized eye has a roughness on the order of a wavelength of light yielding noisy interferograms [105].
- Partially coherent light has properties lying in-between those of purely coherent (laser) and incoherent light (ordinary incandescent lamps). Speckles are reduced with partially coherent light while still maintaining some phase coherence for interferometry [106].
- Incoherent light has the advantage of producing speckle free images. It is therefore a potential solution to the problem encountered with partially and purely coherent light. The topographer system presented in this chapter belongs to that category.

An approach which yields moderate success for PRK monitoring is the method taken by the *PAR* system. *PAR* uses a grid projection and triangulation. Unfortunately, the system requires the addition of fluorescein on top of the corneal surface for measurements. The *PAR* system was tested with an erbium:YAG laser at a wavelength of 2.94 μm . Fluorescein reportedly had no effect on the ablative nature. It

has not been investigated on other photoablative lasers like the excimer laser used in these experiments. Beyond the scope of this paper, our vision is that the corneal shape is computed between every two successive pulses and an automatic feedback based on the extracted corneal shape is sent to the Excimer laser to stop it when the optimal desired corneal shape is reached. The repetition rate of Excimer lasers is a few hertz (5 Hz for the VISX laser used in the experiments). Every 200 ms, a pulse ablates on average $0.25 \mu\text{m}$ of corneal tissue. This repetition rate constrains the shape extraction to be computed within 200 ms time scale. Here we propose and demonstrate a novel topographer technology based on structured incoherent visible light projection and triangulation that do not require addition of fluorescent fluid.

The surface of the cornea is featureless; therefore, landmarks must be projected onto its surface in order to establish correspondence between identical points in subsequent frames taken by the camera. If two cameras were to see the same feature-point from two different viewpoints, depth extraction could be recovered from triangulation. A feature projector can replace one of the cameras. The projector replaces the second camera and at the same time projects landmarks. The experimental design is shown in fig. 6.1.

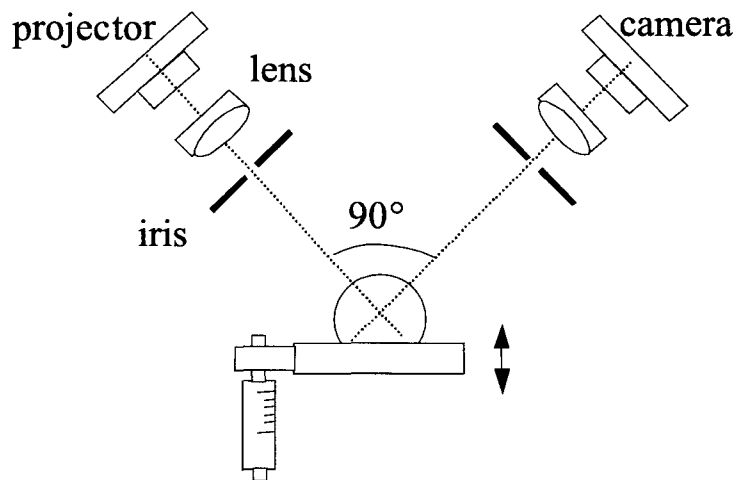


Figure 6.1: Topographer principle. Projection and triangulation are used to measure the three-dimensional shape of the object.

The charge coupled device camera has 786×652 pixels with video NTSC output

(GBC camera, ChelseaIndustries International, Inc., USA). Each pixel is $9.1 \times 8.2 \mu\text{m}$. The frame grabber is the model dt3155 (Data Translation, Marlboro, MA, USA). It produces a sampled image of $640 \times 480 \times 8$ bits array. The projector is a liquid crystal spatial light modulator (Kopin Corporation, Tauton, MA); it features 320 by 240 binary pixels, $15 \times 15 \mu\text{m}$ pixel size. The SLM can be driven at 30 frames/second by the VGA output of a computer. The computer used in the series of experiments described in this paper is an Intel pentium-pro 200 MHz. The size of the spatial light modulator (SLM) is $4.8 \times 3.6 \text{ mm}^2$. The imaging optics consist of one achromat doublet lens (Melles Griot, Irvine, CA). A magnification factor of 1.2 yields an image size onto the cornea of $5.9 \times 4.4 \text{ mm}^2$. The technique is not limited in size: larger SLMs or a higher magnification can give a larger image size onto the cornea. The imaging optics is the same as for the projecting optics. Depth of focus is 2 mm.

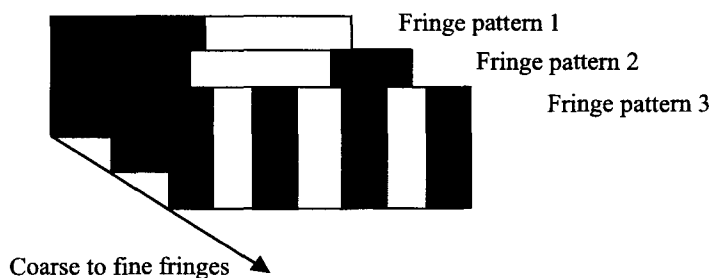


Figure 6.2: Binary fringe patterns of increasing spatial frequency projected by the SLM.

A halogen lamp illuminates the binary SLM. The light power incident at an angle (see fig. 6.1) onto the cornea is $50 \mu\text{W}$. At that power level, the eye is not irritated. This light power level is limited by the SLM, which does not function well when more light power is applied (reduced contrast). Seven binary fringe patterns of increasing spatial frequency are successively projected onto the cornea (the first three projected fringe patterns are shown in fig. 6.3). These seven patterns generate a total of $2^7 = 128$ edges given by the transition from a black fringe to a white fringe and vice versa. The next step consists of precisely extracting the location of these edges with image processing. The transition from black to white or white to black can be determined with a threshold. The threshold value depends strongly on the

illumination intensity. We can get rid of the intensity dependence by using a method involving the projection of the video inverse of each projected binary image [107, 108]. The images of this dual projection are shown in fig. 6.3. In order to extract the edge boundaries between black and white regions, the original and video inverse images are subtracted pixel-wise. The mean intensity is reduced to zero using this method. The resulting signal oscillates symmetrically between positive and negative values. This powerful method is light intensity insensitive and provides subpixel accuracy, because the zero-crossings (location of edges) are found by linear interpolation between two pixels located across the x-axis. When boundary points are extracted as described above, triangulation is performed using parameters such as the relative position of the camera with respect to the projector, optics distortion and focal length. Lens aberration effects from projection and imaging optics are taken into account by a modeled ray-tracing program. These parameters are calibrated at every new measurement before surgery, because relative position between camera and projector may vary. The full calibration procedure and shape computation is not described here; we refer the reader to [108] for details on shape extraction and calibration. The result of triangulation gives a three-dimensional representation of the object in space.

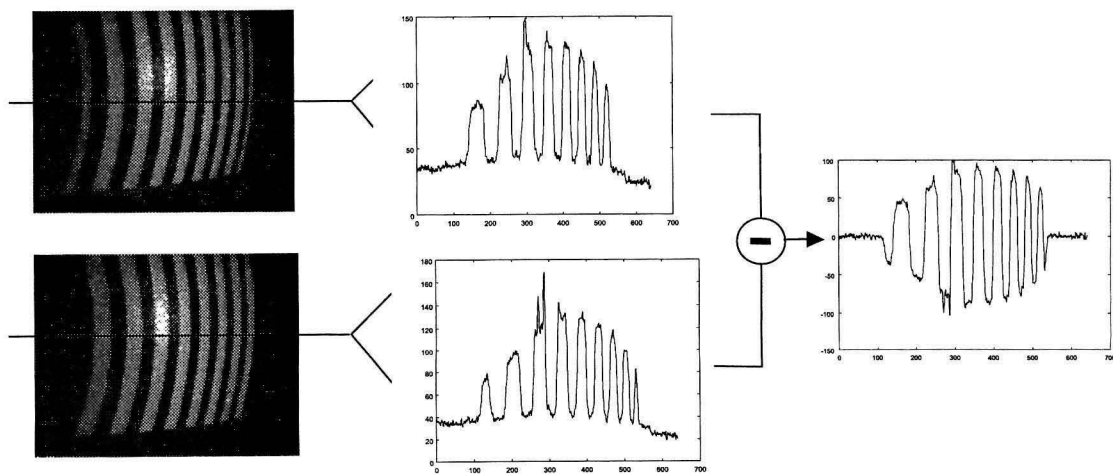


Figure 6.3: Example of a fringe pattern and its video inverse. Subtraction yields zero mean signal.

In order to have a ground measure of our topographer accuracy, we positioned a

white reflected sphere that approximates the human corneal curvature on a vertical micrometer translation stage (fig. 6.1). The sphere can be translated vertically with $0.1 \mu\text{m}$ precision. For our application, only depth change is important. The vertical translation of the sphere implements the effect of ablation (depth change). The sphere is translated vertically by $2 \mu\text{m}$. The three-dimensional shape of the sphere is computed, before and after translation, by the algorithm described above. Depth change is computed from the three-dimensional data.

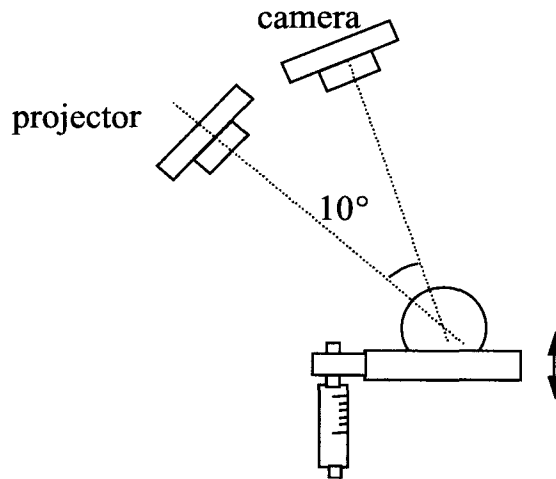


Figure 6.4: Modification of the system to reduce the effect of scattering on images of projected fringes.

The topographer was tested on swine eyes *in vitro*. The eyes are secured on the topographer, which is mounted under the excimer laser. The topographer does not interfere with the pathway of the photoablating beam. Fig. 6.5 shows the prototype topographer under the excimer laser at the Doheny Eye Institute.

The laser pulses ablate the cornea at a repetition rate of 5 Hz with fluence $160 \text{ mJ}/\text{cm}^2$. The corneal surface was not covered by fluorescent liquid. The triangulation geometry is modified as shown in fig. 6.4 to obtain better accuracy (see discussion section). The camera is positioned at an angle of ten degrees with respect to the direction of illumination. We noticed that beyond ten degrees, the edges of a projected fringe pattern become very blurry. This severely hampers shape extraction. We used five swine eyes *in vitro* for this experiment. The first seventy pulses of

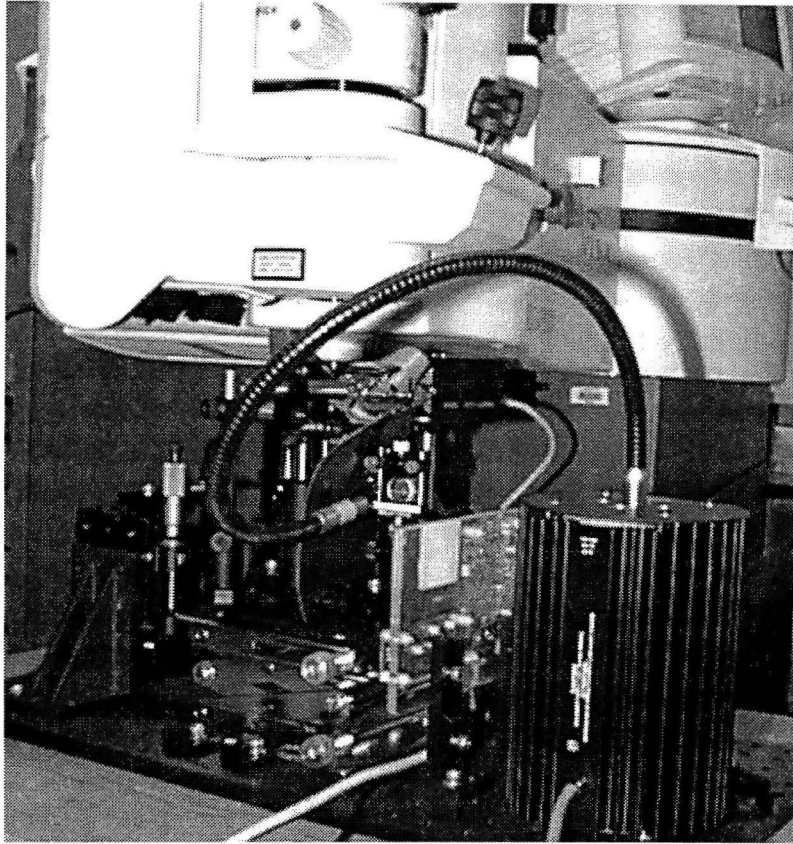


Figure 6.5: Prototype of the topographer under the VISX excimer laser at the Doheny Eye Institute facility.

the excimer laser were used to remove the epithelial layer. Then, after every twenty pulses, the laser is stopped to obtain the topographic data (the images are stored on hard disks before they are processed). 120 pulses are shot at the eyes, providing a total correction of $\simeq 3$ diopters. This process was repeated for each of the 5 swine eyes. For each eye, a series of six topographic maps (0, 20, 40, 60, 80, 100 pulses) are computed using feature points located in the apex of the cornea on a surface of $0.5 \times 0.5 \text{ mm}^2$. From these topographic maps, a depth change is computed between the topographic maps computed every 20 pulses and the topographic map computed before the series of pulses.

Swine eyes were used to test the topographer. These were obtained from a local ablatoir (Farmer John, Vernon, CA). The laser keratectomy procedures were performed using a commercially available excimer laser (VISX, Santa Clara, CA) at the

laser facility of the Doheny Eye Institute at the University of Southern California School of Medicine.

6.3 Results

6.3.1 Performance of the topographer

The depth accuracy of the topographer was successfully measured on a test reflecting sphere. The experimental depth accuracy is $0.5 \mu\text{m}$ and standard deviation (SD) is $0.75 \mu\text{m}$. The topographer was integrated into a commercial Excimer laser system (VISX, Santa Clara, CA). The central ablation depth of swine eyes in vitro could be measured with a depth accuracy of $27 \mu\text{m}$ and a standard deviation of $45 \mu\text{m}$.

6.3.2 Topographer accuracy on test sphere

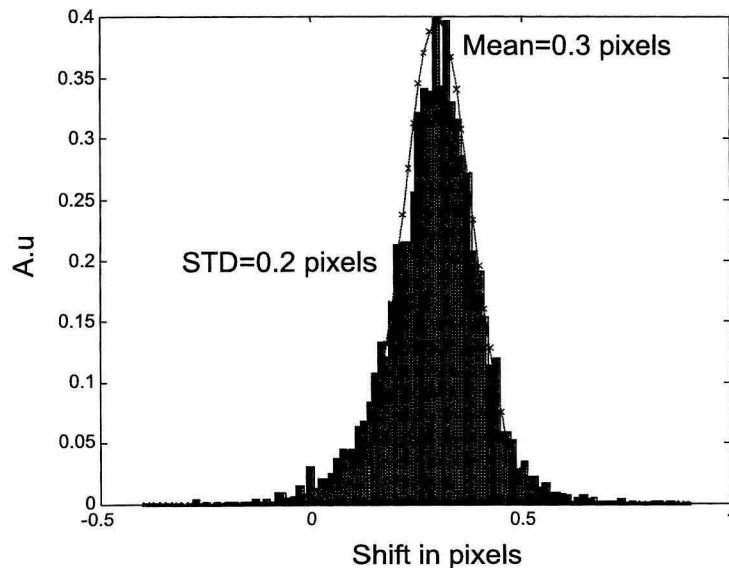


Figure 6.6: Histogram showing the shift between extracted feature points before and after translating the sphere by 2 micrometers.

The histogram in fig. 6.6 shows the distribution of the depth change in terms of camera pixels. A gaussian function is fitted to the experimental values. The mean

shift value is centered at 0.3 pixels. SD is equal to 0.2 pixels. The result is expressed in pixels rather than in micrometers to demonstrate that subpixel accuracy can be achieved with the method of dual projection. 0.3 pixels corresponds to $1.5 \mu\text{m}$. The repeatability of the measurement is tested by taking successive measurements of the sphere at a fixed position. The mean value is close to zero pixels as expected, and SD is 0.2 pixels.

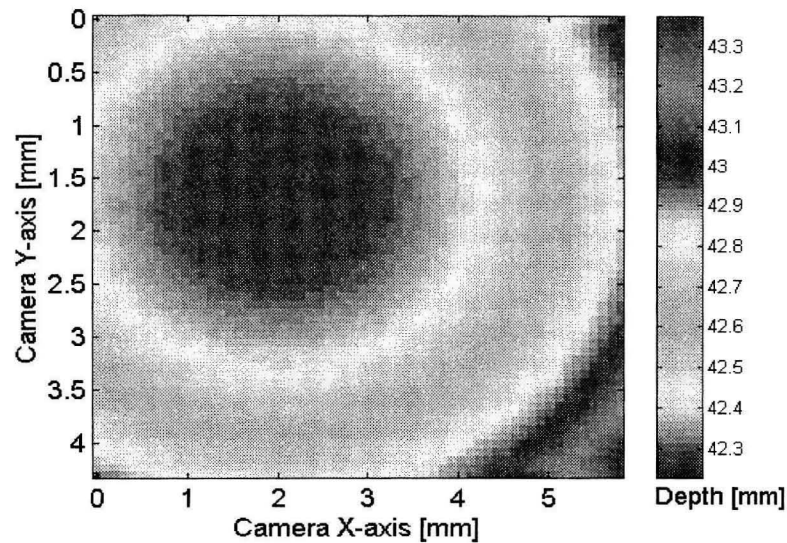


Figure 6.7: Elevation map of the test sphere.

Fig. 6.7 shows an elevation map of the sphere. The computed depth change of $1.5 \mu\text{m}$ and SD of $0.75 \mu\text{m}$ is in good experimental agreement with the $2 \mu\text{m}$ sphere translation. A full accuracy study would require a number of spheres covering a range of curvature. The purpose of this measurement is to obtain an approximate value for the relative ground accuracy of the topographer. The ground relative depth accuracy of the topographer is $\pm 0.5 \mu\text{m}$ with a standard deviation of $0.75 \mu\text{m}$.

With the SLM used in the experiment, the fringe patterns are projected every 30 ms. The entire set of 12 images require a total projection time of 360 ms. This projection time is equal to twice the time allocated for projection and shape extraction. A low cost solution to this problem is to use ferro-electric SLM's which can display binary images every 1-ms and use a standard camera and frame grabber that

can work at 60Hz. A much higher cost solution is to use high frame rate cameras that can acquire 1000 frames/second. In this study, we did not address the problem of eye movement during the projection time. It is certainly a major factor that determines the maximum total projection time. The number of features points produced on the cornea by the fringe projection system is equal to 30,720 (64 edges/rows produced by 12 projected images multiplied by 480 rows, which is the number of rows of the camera). The computational cost of extracting 30,720 points is very low because the algorithm is reduced to finding zero crossings [108].

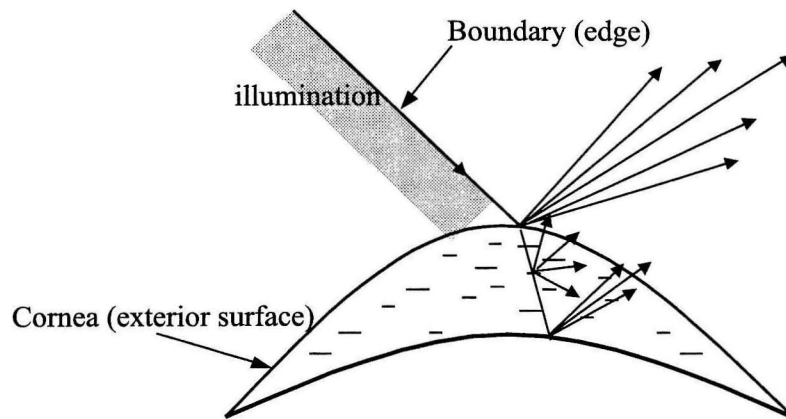


Figure 6.8: Spurious scattering by fibrils within the cornea and by the anterior surface of the cornea.

6.3.3 Topographer accuracy on de-epithelialized swine eyes *in vitro*

Blurred boundaries in images reflected by the cornea are due to scattering by the stroma containing very small collagen fibrils and intercellular substances [109, 110]. Reflections from the internal surface of the cornea contribute as well to the blurring. An illustration of the formation of blurred edges is sketched in fig. 6.8. Due to the exterior surface roughness of the cornea, light rays are scattered. We noticed that the major fraction of light is scattered specularly causing an intensity saturation of the camera in the specular direction. A polarizer with axis orientated at 90° from the incident polarization cuts off a major part of the specular reflected light. In practice,

we could always find an orientation of the cornea such that the remaining specular reflection comes out of the region of interest. The refracted portion of the rays inside the cornea is scattered uniformly by fibrils. It is known that scattering within the cornea is increased with corneal hydration [111]. We injected water in the vitreous cavity with a syringe in order to obtain a ripple free corneal surface. Hydration is therefore changed by additional pressure compressing the fibrils, producing larger scattering than for eyes *in vivo*. The various scattering mechanisms within the cornea contribute to the blurring of image edges captured by the camera. All 20 swine corneas showed blur in the images. The effect of scattering from the interior cornea and by the fibrils can be reduced with the topographer configuration shown in fig. 6.4.

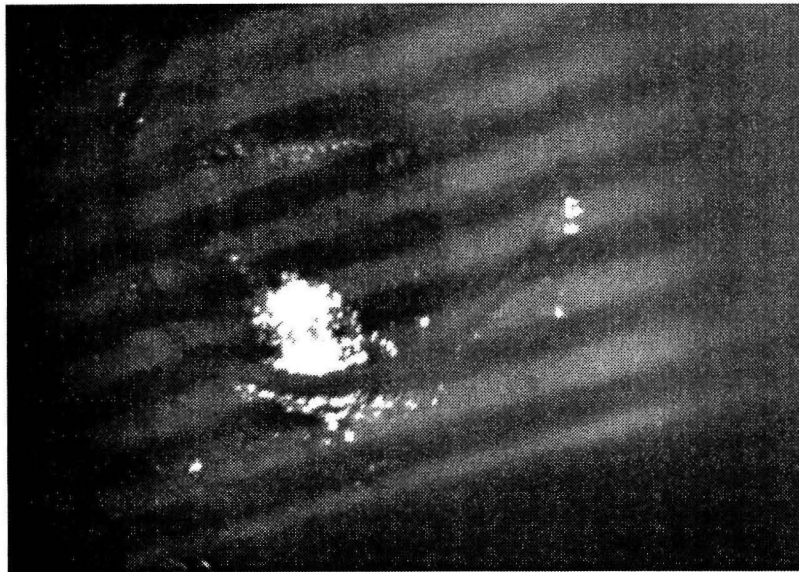


Figure 6.9: Stripes generated on the cornea using the set-up of fig. 6.8.

The illumination and the camera make an angle of approximately 10° . Indeed, images of a projected fringe pattern show sharper edges with this geometry (fig. 6.9). Fig. 6.10 (left) shows a vertical cross section of fig. 6.9. Extracting boundaries from the graph of fig. 6.10 (left) is difficult because the threshold is position dependent and the amplitudes are low. The process of taking the difference (pixel-wise) of a fringe pattern and its video inverse allows a subsequent noise reduction because it discounts the non-uniform average illumination reflected by the cornea. This is illustrated in

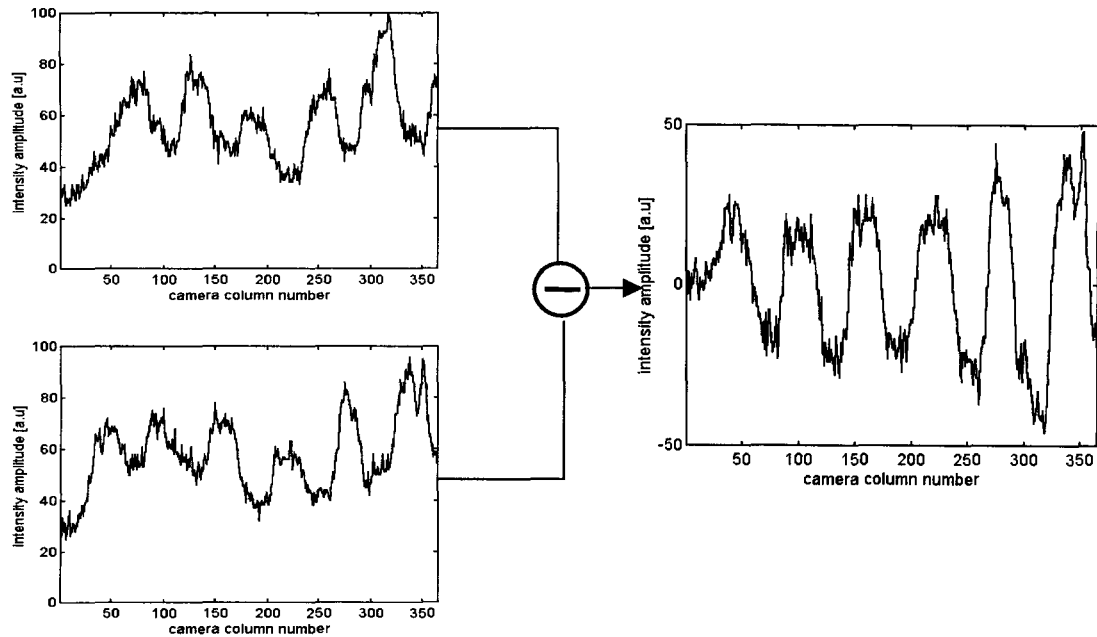


Figure 6.10: Vertical cross section of fig. 6.9. Subtraction of a fringe pattern and its corresponding video inverse (left) produces clean zero-crossings (right).

fig. 6.10 (right).

This triangulation geometry plus the dual fringe pattern projection and the large number of feature points that can be extracted represent new contributions to the PAR system that allow measurement of de-epithelialized cornea without addition of fluorescein.

Fig. 6.11 shows an histogram of the ablation depth after 80 pulses. A gaussian fit yields a mean equal to $27 \mu\text{m}$ and a standard deviation of $45 \mu\text{m}$. Fig. 6.12 shows a graph correlating the number of Excimer laser pulses and the computed ablation. The error bars are equal to the standard deviation of the ablation depth. The slope of the curve in fig. 6.12 is calculated by linear regression and is equal to $0.35 \mu\text{m}/\text{pulse}$. The tabulated ablation rate of pigs' corneas is $0.25 \mu\text{m}/\text{pulse}$. The depth of surgical ablation needed for a refractive change of 0.25 diopter is $3 \mu\text{m}$. To achieve an accuracy of 0.25 diopters, adequate to give 20/20 vision to most patients, the central cornea needs to be measured with an accuracy of $3 \mu\text{m}$. At the present state of study, this new topographer does not improve the reliability of the Excimer laser surgery. It

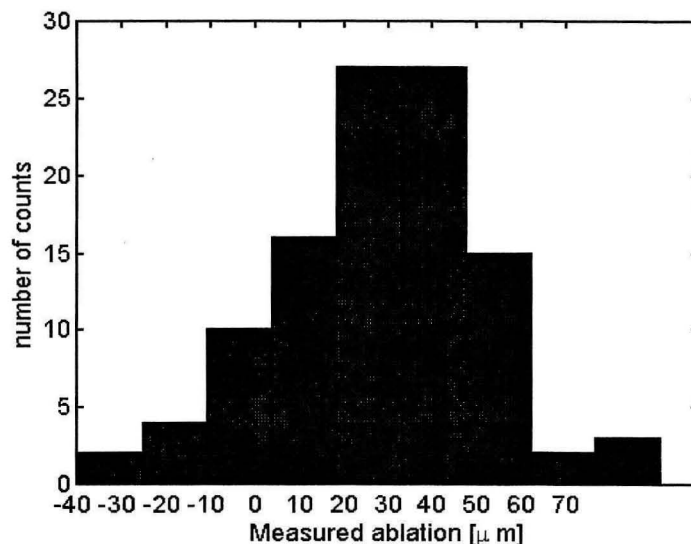


Figure 6.11: Histogram of the difference between the three-dimensional reconstruction of the cornea surface before and after 80 pulses ablation over an area of 1.25 mm^2 at the apex of the cornea.

seems that, potentially, this new technology can become practical for interoperative PRK monitoring if the blurring effect of fringes caused by corneas can be solved.

We suggest that potential improvement can be achieved by changing the wavelength of illumination. Since scattering is due to fibrils within the cornea, we expect to decrease its influence by choosing a wavelength in the range where the cornea absorbs light, yielding only a response from the outer cornea's surface. The cornea absorbs light in the range $1.3\text{-}1.4 \mu\text{m}$ and in the deep ultra-violet range near 200 nm . Experiments performed with infrared light at $1.4 \mu\text{m}$ did not give better contrast because the cornea behaves like a reflecting surface at that wavelength reflecting light only specularly. We believe that illumination in far ultra-violet can increase the contrast, because scattering by the top surface is increased due to the shorter illumination wavelength. Moreover, unwanted scattering by fibrils within the anterior cornea chamber can be avoided due to the fact that far ultraviolet light only penetrates a few micrometers below the cornea's top surface.

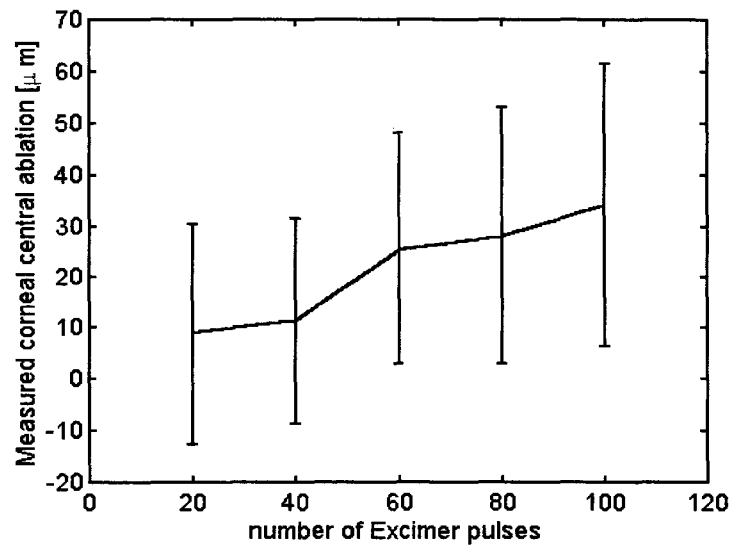


Figure 6.12: Central ablation depth versus the number of Excimer pulses incident on the cornea.

Chapter 7 Conclusion

In this thesis, I have addressed the use of localized holograms for optical data storage. I have shown that it is possible to record up to one hundred holograms in a layered architecture and retrieve them with high fidelity [115]. The time necessary to record the whole memory is similar to that of conventional holographic memories [44]. The method of localized recording in $\text{LiNbO}_3:\text{Fe,Mn}$ enables multiple erasure and writing cycles without the need to rewrite the entire memory. Any hologram can be written independently without an exposure schedule. The flexibility and simplicity of the layered memory is a step towards a real application. The memory capacity is limited by diffraction of a focused reference beam. By using phase conjugation, I have shown that the capacity could be further increased by a factor of 10. Although the localized method can yield diffraction efficiencies for M holograms that vary inversely proportional to M , the experimental results showed that scattering by the gating light erases the hologram in the adjacent layers [46]. If scattering effects could be reduced, the method outlined could record arbitrary diffractive optical element with maximal efficiency.

A hologram recorded with a spatial amplitude modulation can be transferred into a temporal modulation of a diffracted ultra-fast pulse. I show that the gating light can spatially modulate the recordable areas in doubly doped lithium niobate. The hologram is therefore amplitude modulated and a single femtosecond pulse diffracted off the hologram could produce a stream of ten pulses with very good homogeneity and signal to noise ratio.

I have presented a new multiplexing method based on the confinement of a spherical beam in a slab waveguide. Although the spherical beam is localized in two dimensions, the shift selectivity is that of conventional shift selectivity in volume crystals. The advantage of that method is that confinement enables thin memory designs. I show a read-only memory design that is 1 mm thin and contains no moving parts.

The memory holds 1 Gbits with a read-out rate up to 2.5 Gb/s [116].

New wavelength selective materials have been fabricated and tested for spectral hole burning. These materials are sensitive around 800 nm. The ratio between the inhomogeneous linewidth and the homogeneous linewidth determines the number of holograms that can be recorded by tuning the wavelength. Ratios up to 10^5 have been measured in these polymer films. I show that additional holograms can be recorded using Bragg multiplexing at each frequency channel. The $M/\#$ of the material is very low (0.05) because holograms are recorded by absorption modulation rather than index modulation. The low $M/\#$ limits the number of bragg-multiplexed holograms to approximately 10 [117].

All-optical ultra-fast gates have been investigated as a tool for controlling ultra-fast pulses. A stream of pulses can be generated by the pulse shaper and stored in the spectral hole burning memory developed in the frame of this thesis. I experimentally realized an AND, OR and XOR gate by non-linear mixing in BBO crystals. The energy per gate is estimated at 0.1 nJ/pulse. With a clock of 1 THz, the power consumption per gate is 100 W.

A wavefront sensor was investigated based on conoscopic patterns. When the wavefront is quasi-planar, the conoscopic pattern is formed by the lateral shear of the wavefront. We show that the phase of the wavefront can be recovered by decomposition into Hermite polynomials. The wavefront reconstruction error was less than 100 nm. A second sensor based on structured lighting was developed for an application in ophthalmology. The absolute accuracy of the topographer was $\pm 1 \mu\text{m}$. Tests on swine eyes showed that the depth accuracy was mainly limited by the multiple reflections occurring inside the cornea [118].

Appendix A moving-edge method

To determine the width of the focused beam, a sharp edge is moved through the beam, perpendicular to its direction of propagation. At several positions along the beam profile, the transmitted power is detected. The transverse intensity distribution

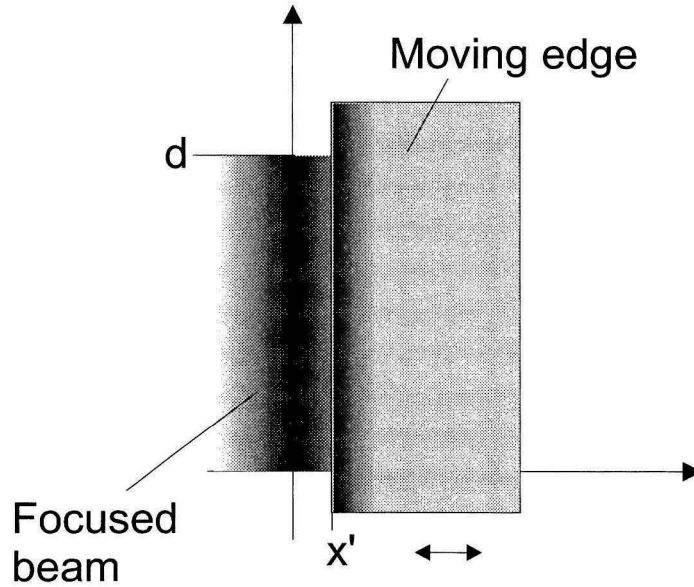


Figure A.1: Principle of measuring the beam width with the moving-edge method.

of a focused Gaussian is described by:

$$I(x, y, z) = I_0(z, y) \cdot e^{-2\frac{x^2}{w_e^2}}. \quad (\text{A.1})$$

where w_e is the beam waist (for $x = w_e$, the power has decreased to $1/e^2$ (13.5%)). The measurement of the transmitted power as a function of the position of the edge x' corresponds to an experimental integration:

$$\begin{aligned} P_T(x) &= \int_{-\infty}^{x'} I_0 d \cdot e^{-2\frac{x^2}{w_e^2}} dx = \frac{w_e}{2} I_0 d \cdot \int_{-\infty}^{2\frac{x'}{w_e}} e^{-\frac{t^2}{2}} dt \\ &= \sqrt{\frac{\pi}{2}} w_e I_0 d \cdot \Phi\left(2\frac{x'}{w_e}\right) = P_0 \cdot \Phi\left(2\frac{x'}{w_e}\right), \end{aligned} \quad (\text{A.2})$$

where d is the transverse expansion of the beam in the y direction, Φ the Gaussian errorfunction and P_0 the total power

$$P_0 = \int_{-\infty}^{\infty} I_0 d \cdot e^{-2\frac{x^2}{w_e^2}} dx = \sqrt{\frac{\pi}{2}} w_e I_0 d. \quad (\text{A.3})$$

At the position $x'_1 = -\frac{w_e}{2}$ of the edge, the errorfunction delivers a transmitted power of $P_T = P_0 \cdot 0.16$. At the position $x'_2 = \frac{w_e}{2}$ the power is $P_T = P_0 \cdot 0.84$.

By measuring the two positions of the edge, where 16% and 84% of the beam power are transmitted, the Gaussian beam width at the position of the edge can be determined as $w_e = x'_2 - x'_1$.

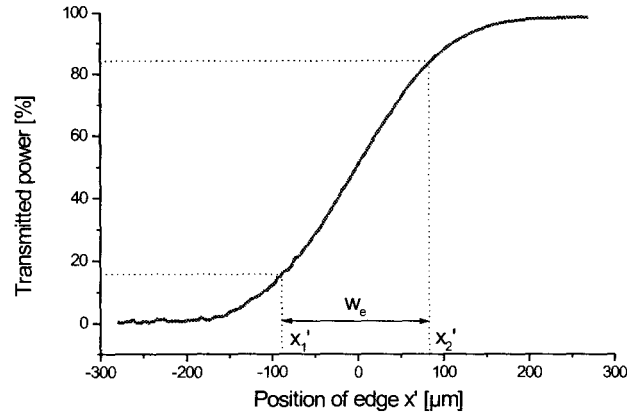


Figure A.2: Measurement of the transmitted power as a function of the edge position x' , and determination of the beam width w_e .

Bibliography

- [1] “Historical notes about the Cost of Hard Drive Storage space”
<http://www.altis.net/ns1625/winchest.html>
- [2] H. J. Coufal, D. Psaltis and G. T. Sincerbox, “Holographic Data Storage”
Springer Series in Optical Sciences ISDN 0342-4111, 2000.
- [3] D. Psaltis, “Parallel optical memories,” *Byte*, 17(9):179, 1992.
- [4] D. Psaltis and F. Mok, “Holographic memories,” *Sci. Am.*, 273(5):70–76, 1995.
- [5] G. W. Burr, F. H. Mok, and D. Psaltis, “Angle and space multiplexed storage using the 90° geometry,” *Opt. Commun.*, 117(1-2):49–55, 1995.
- [6] F. S. Chen, J. T. LaMacchia, and D. B. Fraser, “Holographic storage in lithium niobate,” *Appl. Phys. Lett.*, 15(7):223–225, 1968.
- [7] G. W. Burr, X. An, F. H. Mok, and D. Psaltis, “Large-scale rapid-access holographic memory (Paper F2.3),” in *SPIE Optical Data Storage Topical Meeting*, San Diego, 1995.
- [8] Geoffrey W. Burr, *Volume holographic storage using the 90° geometry*, PhD thesis, California Institute of Technology, 1996.
- [9] I. McMichael, W. Christian, D. Pletcher, T. Y. Chang, and J. Hong, “Compact holographic storage demonstrator with rapid access,” *Appl. Opt.*, 35(14):2375–2379, 1996.
- [10] J.-J. P. Drolet, E. Chuang, G. Barbastathis, and D. Psaltis, “Compact, integrated dynamic holographic memory with refreshed holograms,” *Opt. Lett.*, 22(8):552–554, 1997.

- [11] F. H. Mok, G. W. Burr, and D. Psaltis, "Angle and space multiplexed random access memory (HRAM)," *Optical Memory and Neural Networks*, 3(2):119–127, 1994.
- [12] K. Buse, A. Adibi, and D. Psaltis, "Non-volatile holographic storage in doubly doped lithium niobate crystals," *Nature* 393:665, 1998.
- [13] A. Adibi, K. Buse, and D. Psaltis, "Effect of annealing in two-center holographic recording," *Appl. Phys. Lett.* 74(25):3767–3769, 1999.
- [14] A. Adibi, K. Buse, and D. Psaltis, "Sensitivity improvement in two-center holographic recording," *Opt. Lett.* 25(8):539–541, 2000.
- [15] A. Adibi, "Persistent holographic storage in photorefractive crystals," *Thesis*, California Institute of Technology, 2000.
- [16] Y. W. Liu, L. R. Liu, and L. Y. LY, "Experimental study of non-volatile holographic storage in doubly- and triply-doped lithium niobate crystals," *Opt. Commun.* 181(1-3):47–52, 2000.
- [17] N.V. Kukhtarev, "Kinetics of hologram recording and erasure in electrooptics crystals," *Sov. Tech. Phys. Lett.* 2:438, 1976.
- [18] P. Yeh, "Introduction to photorefractive nonlinear optics," *Wiley Series* Chap. 3, p. 108, 1993.
- [19] T. J. Hall, R. Jaura, L. M. Connors, and P. D. Foote, "The photorefractive effect – a review," *Progress in Quantum Electronics*, 10(2):77–145, 1985.
- [20] H. C. Kulich, "A new approach to read volume holograms at different wavelengths," *Opt. Comm.* 64:407–411, 1987.
- [21] G. A. Rakuljic, V. Levya, and A. Yariv, "Optical data storage by using orthogonal wavelength–multiplexed volume holograms," *Opt. Lett.*, 17(20):1471–1473, 1992.

- [22] D. Psaltis, F. Mok, and H.Y.-S. Li, "Nonvolatile storage in photorefractive crystals," *Opt. Lett.*, 19(3):210–212, 1994.
- [23] G. Barbastathis, and D. Psaltis, "Shift-multiplexed holographic memory using the two-lambda method," *Opt. Lett.* 21(6):432–434, 1996.
- [24] E. Chuang, and D. Psaltis, "Storage of 1000 holograms with use of a dual-wavelength method," *Appl. Opt.* 36(32):8445–8454, 1997.
- [25] A. Yariv, S. Orlov, G. Rakuljic, and V. Leyva "Holographic fixing, readout and storage dynamics in photorefractive materials," *Opt. Lett.* 20(11):1334–1336, 1995.
- [26] X. An, G. W. Burr, and D. Psaltis, "Thermal fixing of 10,000 holograms in $\text{LiNbO}_3\text{:Fe}$," *Appl. Opt.* 38(2):386–393, 1999.
- [27] J. F. Heanue, M. C. Bashaw, A. J. Daiber, R. Snyder, and L. Hesselink, "Digital holographic storage system incorporating thermal fixing in lithium niobate," *Opt. Lett.* 21:1615–1617, 1996.
- [28] G. Montemezzani, and P. Guenter, "Thermal hologram fixing in pure and doped KNbO_3 crystals," *J. Opt. Soc. Am.* 7(12):2323–2328, 1990.
- [29] J. J. Amodei, and D. L. Staebler "Holographic pattern fixing in electro-optics crystals," *Appl. Phys. Lett.* 18:540–542, 1971.
- [30] Y. Qiao, S. Orlov, D. Psaltis, and R. R. Neurgaonkar, "Electrical fixing of photorefractive holograms in $(\text{Sr}_{0.75}\text{Ba}_{0.25})\text{Nb}_2\text{O}_6$," *Opt. Lett.*, 18(12):1004–1006, 1993.
- [31] J. A. Ma, T. Chang, J. Hong, R. Neurgaonkar, G. Barbastathis, and D. Psaltis, "Electrical fixing of 1000 angle-multiplexed holograms in SBN:75 ," *Opt. Lett.* 22(14):1116–1118, 1997.

- [32] G. Barbastathis, D. Psaltis, T. Chang, J. Hong, and R. R. Neurgaonkar, "Electrical fixing of angularly multiplexed holograms in SBN:75," in *OSA Annual Meeting '95*, Portland, Oregon, 1996.
- [33] M. Horowitz, A. Bekker, and B. Fischer, "Image and hologram fixing method with $(\text{Sr}_x\text{Ba}_{1-x})\text{Nb}_2\text{O}_6$ crystals," *Opt. Lett.*, 18(22):1964–1966, 1993.
- [34] H. Guenther, G. Wittmann, R. M. Macfarlane, and R.R Neurgaonkar, "Intensity dependence and white-light gating of two-color photorefractive gratings in LiNbO_3 ," *Opt. Lett.* 22:1305–1307, 1997.
- [35] D. Von der Linde, A. M. Glass, and K. F. Rodgers "Multiphoton photorefractive processes for optical storage in LiNbO_3 ," *Appl. Phys. Lett.* 25:155–157, 1974.
- [36] G. T. Sincerbox, "Selected papers on Holographic storage," SPIE Milestone Series, vol. MS 1995.
- [37] A. Adibi, K. Buse, and D. Psaltis, "Multiplexing holograms in $\text{LiNbO}_3 : \text{Fe} : \text{Mn}$ crystals," *Opt. Lett.*, 24: 652, 1999.
- [38] L. d' Auria, J. P. Huignard, C. Slezak, and E. Spitz, "Experimental holographic read-write memory using 3-D storage," *Appl. Opt.*, 13(4):808–818, 1974.
- [39] K. Buse, L. Holtmann, and E. Kratzig, "Activation of BaTiO_3 for infrared holographic recording," *Opt. Commun* 85: 183, 1991.
- [40] L. Hesselink, S. Orlov, A. Liu, A. Akella, D. Lande, and R. R. Neurgaonkar, "Photorefractive materials for nonvolatile volume holographic data storage," *Science* 282:1089, 1998.
- [41] D. A. Parthenopoulos, and P. M. Rentzepis, "3-Dimensional optical storage memory," *Science* 245:843, 1989.
- [42] M. M. Wang, S. C. Esener, F. B. McCormick, I. Okgr, A. S. Dvornikov, and P. M. Rentzepis, "Experimental characterization of a two-photon memory," *Opt. Lett.* 22:558, 1997.

- [43] F. Mok, G. W. Burr, and D. Psaltis, "A system metric for holographic memory systems," *Opt. Lett.*, 21(12):896–898, 1996.
- [44] C. Moser, B. Schupp, and D. Psaltis, "Localized holographic recording in doubly doped lithium niobate," *Opt. Lett.* 25:162, 2000.
- [45] A. Adibi, K. Buse, and D. Psaltis, "Sensitivity improvement in two-center holographic recording," *Opt. Lett.* 25(8):539–541, 2000.
- [46] C. Moser, I. Maravic, B. Schupp, A. Adibi, and D. Psaltis, "Diffraction efficiency of localized holograms in doubly doped LiNbO_3 crystals," *Opt. Lett.* 25(17):1243–1245, 2000.
- [47] A. M Weiner, and D. E. Leaird, "Generation of Terahertz-rate trains of femtosecond pulses by phase-only filtering," *Opt. Lett.* 15: 51–53, 1990.
- [48] A. M Weiner, D. E. Leaird, J. S. Patel, and J. R. Wullert, "Programmable femtosecond pulse shaping by use of a multielement liquid-crystal phase modulator," *Opt. Lett.* 15: 326–328 1990.
- [49] D. J. Brady, A. G.-S. Chen, and G. Rodriguez, "Volume holographic pulse shaping," *Opt. Lett.* 17(20):610–612, 1992.
- [50] K. B. Hill, and D. J. Brady, "Pulse shaping in volume reflection holograms," *Opt. Lett.* 18(20):1739–1741, 1993.
- [51] K. B. Hill, and D. J. Brady, "Impulse response of strong reflection holograms," *App. Opt.* 32(23):4305–4316, 1993.
- [52] D. Psaltis, M. Levene, A. Pu, G. Barbastathis, and K. Curtis, "Holographic storage using shift mutliplexing," *Opt. Lett.* 20(7):782–784, 1995.
- [53] G. Barbastathis, M. Levene, and D. Psaltis, "Shift multiplexing with spherical reference waves," *Appl. Opt.* 35(14):2403–2417, 1996.

- [54] K. Curtis, and D. Psaltis, "Characterization of the Du-Pont photopolymer for 3-dimensional holographic storage," *Appl. Opt.*, 33(23):5396–5399, 1994.
- [55] H.-Y. S. Li, and D. Psaltis, "Three dimensional holographic disks," *Appl. Opt.*, 33(17):3764–3774, 1994.
- [56] D. Psaltis, and A. Pu, "Holographic 3-D disks," *Optoelectron-Devices* 10(3):333–342, 1995.
- [57] Allen Pu, *Holographic 3D disks and optical correlators using photopolymer materials, PhD thesis*, California Institute of Technology, 1997.
- [58] S. Q. Tao, Z. Q. Jiang, Q. Yuan, et al., "Multi-track storage of 10000 holograms in a disk-type photorefractive crystal," *Chinese Phys. Lett.* 17(9):675–677, 2000.
- [59] F. H. Mok, "Angle-multiplexed storage of 5000 holograms in lithium niobate," *Opt. Lett.*, 18(11):915–917, 1993.
- [60] G. Barbastathis, "Intelligent Holographic Databases" *PhD Thesis*, California Institute of Technology, 1997.
- [61] A. S. Bablumian, T. F. Krile, D. J. Mehrl, et al. "M-type thick holograms in bacteriorhodopsin films with a high-divergence reference beam," *Appl. Opt.* 37(8):1350–1355, 1998.
- [62] Saleh, and C. Teich, "Fundamental of Photonics," J. Wiley & Sons, 1991.
- [63] A. Yariv, *Optical Electronics*, Saunders College, 4th edition, 1991.
- [64] J. W. Goodman, *Statistical Optics*, J. Wiley & Sons, 1985.
- [65] Y. N. Denisyuk, "Multiplexing of three-dimensional shift speckle holograms in layers of bichromated gelatin," *Opt. and Spectr.* 85(2):293–296, 1998.

- [66] Y. H. Kang, K. H. Kim, and B. Lee, "Angular and speckle multiplexing of photorefractive holograms by use of fiber speckle patterns," *Appl. Opt.* 37(29):6969–6972, 1998.
- [67] D. Brady, "Photorefractive volume holography in artificial neural networks," *PhD Thesis*, California Institute of Technology, 1990.
- [68] J. W. Goodman, *Introduction to Fourier Optics*, Mc Graw–Hill, 1998.
- [69] D. Psaltis, *Optical computing class notes*, California Institute of Technology, 1998.
- [70] S. Yin, H. Zhou, F. Zhao, M. Wen, Y. Zang, J. Zhang, and F. T. S. Yu, "Wavelength-multiplexed holographic storage in a sensitive photorefractive crystal using a visible-light tunable diode-laser," *Opt. Commun.*, 101(5-6):317–321, 1993.
- [71] B. Plagemann, F. R. Graf, S. B. Altner, A. Renn, and U.P. Wild,, "Exploring the limits of optical storage using persistent spectral hole-burning: holographic recording of 12,000 images," *Appl. Phys.B* 66, 1998.
- [72] A. V. Turukhin, and A. A. Gorokhovskiy, "Determination of quantum efficiency of persistent spectral hole burning using dispersive kinetics," *Chem. Phys. Lett.* 317(1-2):109–115, 2000.
- [73] R. Jankowiak, L. Shu, M. J. Kinney, and G. J. Small, "Dispersive kinetic processes, optical linewidths and dephasing in amorphous solids," *J. Lum.* 36(4-5):293–305, 1987.
- [74] A. Elschner, and H. Bassler, "Kinetics of growth and decay of spectral holes in a tetracene-doped MTHF glass," *Chem. Phys.* 123(2):305–315, 1988.
- [75] H. Talon, M. Orrit, and J. Bernard, "Model for burning kinetics and shape of fluence-saturated spectral holes," *Chem. Phys.* 140(1):177–185, 1990.
- [76] A. A. Gorokhovskii, R. K. Kaarli, and L. A. Rebane, *JETP Lett.* 20, 1974.

- [77] L. Kador, G. Schulte, and D. Haarer, "Relation between hole-burning parameters and molecular parameters free-base phthalocyanine in polymer hosts," *J. Chem. Phys.* 90(7):1264–1270, 1986.
- [78] W. E. Moerner, M. Gehrtz, and A. L. Huston, "Measurement of quantum efficiencies for persistent spectral hole burning," *J. Chem. Phys.* 88(25):6459–6460, 1984.
- [79] *Aldrich, Inc.*, <http://www.sigma-aldrich.com>
- [80] H. Suzuki, and T. Shimada, "Fast burning of persistent spectral holes in donor-acceptor electron-transfer systems," *Mol. Cryst.* 216:433–438, 1992.
- [81] W. H. Kim, T. Reinot, J. M. Hayes, and G. J. Small, "Hyperquenched glassy films of water- a study by hole burning," *J. Phys. Chem.* 99(19):7300–7310, 1995.
- [82] H. Kogelnik, "Coupled wave theory for thick hologram gratings," *Bell Syst. Tech. J.*, 48(9):2909–2947, 1969.
- [83] A. Rebane, S. Bernet, A. Renn, and U.P. Wild, "Holography in frequency selective media - hologram phase and causality," *Opt. Comm.* 86(1):7–13, 1991.
- [84] S. Bernet, B. Kohler, A. Rebane, A. Renn, and U. P. Wild, "Holography in frequency selective media. 2. Controlling the diffraction efficiency," *J. Lum.* 53(1-6):215–218, 1992.
- [85] T. W. Mossberg, "Time-domain frequency-selective optical data storage," *Opt. Lett.*, 7(2):77–79, 1982.
- [86] X. A. Shen, E. Chaing, and R. Kachru, "Time-domain holographic image storage," *Opt. Lett.*, 19(16):1246–1248, 1994.
- [87] R. A. Barry, V. W. S. Chan, K. L. Hall, E. S. Kintzer, J. D. Moores, K. A. Rauschenbach, E. A. Swanson, L. E. Adams, C. R. Doerr, S. G. Finn,

- H. A. Haus, E. P. Ippen, and W. S. Wong, "A Precompetitive Consortium on Wide-Band All-optical Networks," *J.Sel. Areas Commun./J. Lightwave Techn.* Special issue on optical networks 11:714, 1995.
- [88] K. L. Hall, and K. A. Rauschenbach, "100-Gbits/s bitwise logic," *Opt. Lett.* 23:1271–1273, 1998.
- [89] A. M. Weiner, "Effect of group velocity mismatch on the measurement of ultrashort optical pulses via second harmonic generation," *IEEE J. Quant. Elect.* 19:1276–1283, 1983.
- [90] S. Takeuchi, T. Masuda, and T. Kobayashi, "Visible to near-infrared femtosecond dynamics of photoexcited gap states in substituted polyacetylenes," *J. Chem. Phys.* 105(7):2859–2873, 1996.
- [91] G. Barbastathis, M. Balberg, and D.J. Brady, "Confocal microscopy with a volume holographic filter," *Opt. Lett.* 24(12):811–813, 1999.
- [92] G. Sirat, and D. Psaltis, "Conoscopic holography," *Opt. Lett.* 10(1):4–6, 1985.
- [93] G. Sirat, and D. Psaltis, "Conoscopic holograms," *Opt. Commun.* 65(4):243–249, 1988.
- [94] G. Sirat, "Conoscopic holography. I. Basic principles and physical basis," *J. Opt. Soc. Am. A* 9(1):70–83, 1992.
- [95] G. Sirat, "Conoscopic holography. II. Rigorous derivation," *J. Opt. Soc. Am. A* 9(1):84–90, 1992.
- [96] D. S. Marks, "Subwavelength structures optical diffraction, and optical disk memories," *PhD Thesis*, California Institute of Technology, 1996.
- [97] *UBM* <http://www.ubmusa.com>.
- [98] *Micro-photonics, Inc.* <http://www.microphotonics.com>.

- [99] G. Harbers, P. J. Kunst, and G. W. R. Leibbrandt, "Analysis of lateral shearing interferograms by use of Zernike polynomials," *Appl. Opt.* 35(31):6162–6172, 1996.
- [100] J. Bryanston-Cross, C. Quan, and T. R. Judge, "Holographic deformation measurements by Fourier transform technique with automatic phase unwrapping," *Opt-Eng.* 31(3):533–543, 1992.
- [101] P. J. McDonnell, and T. Seiler, "Excimer laser photorefractive keratectomy," *Surv. Ophthalmol.* 40:89–118, 1995.
- [102] P. J. McDonnell, "Excimer laser corneal surgery: new strategies and old enemies," *Ophthalmol. Vis. Science* 36(1), 1995.
- [103] W. Belin, "Intraoperative raster photogrammetry- the PAR Corneal Topography System," *J. Cataract. refract. surg.* vol 19, 1993.
- [104] H. J. Tiziani, "Topometry of technical and biological objects by fringe projection," *Appl. Optics*, 34(19):3644–3547, 1995.
- [105] H. Kasprzak, "Holographic measurement of changes of the central corneal curvature due to intraocular pressure differences," *Opt. Eng.*, 33(1):198-203, 1994.
- [106] C. Moser, G. Barbastathis, and D. Psaltis, "Conoscopic System For Real-Time Topography," *U.S. Patent*, No. 5,909,270.
- [107] M. Trobina, "Error Model of a Coded-Light Range Sensor," *Technical Report*, Communication Technology Laboratory, ETH-Zurich, Switzerland 1995.
- [108] J. Y. Bouguet, "Visual methods for three dimensional modeling," *PhD Thesis*, California Institute of Technology, 1999.
- [109] D. E. Freund, R. L. McCally, R. A. Farrell, S. M. Cristol, N. L. L'Hernault, and H. F. Edelhauser, "Ultrastructure in Anterior and posterior Stroma of Perfused Human and Rabbit Corneas," *Inv. Ophthalmol. Vis. Science*, 36(8): 1995.

- [110] G. T. H. Smith, N. A. P. Brown, G. Adrien, and Shun-Shin, "Light Scatter From the Central Human Cornea," *The Eye*, 4th edition, 4:584-588, 1990.
- [111] T. Olsen, "Light scattering from the human cornea," *Inv. Ophthalmol. Vis. Science*, 81-86, 1982.
- [112] C. Denz, G. Pauliat, and G. Roosen, "Volume hologram multiplexing using a deterministic phase encoding method," *Opt. Commun.*, 85:171-176, 1991.
- [113] K. Curtis, A. Pu, and D. Psaltis, "Method for holographic storage using peristrophic multiplexing," *Opt. Lett.*, 19(13):993-994, 1994.
- [114] J. B. Thaxter, and M. Kestigian, "Unique properties of SBN and their use in a layered optical memory," *Appl. Opt.*, 13(4):913-924, 1974.
- [115] C. Moser, and D. Psaltis, "Holographic memory using localized recording," *submitted to Appl. Opt.*
- [116] C. Moser, W. Liu, and D. Psaltis, "Folded shift multiplexing," *submitted to Opt. Lett.*
- [117] A. V. Turukhin, A. A. Gorokhovskiy, C. Moser, I. V. Solomatin, and D. Psaltis, "Spectral hole burning in naphthalocyanines derivatives in the region 800 nm for holographic storage applications," *J. Lumin.* 86(3-4):399-405, 2000.
- [118] C. Moser, J. Kampmeier, P. McDonnell, and D. Psaltis, "Feasibility of intra-operative corneal topography monitoring during photorefractive keratectomy," *J. Refract. Surg.* 16(2):148-154, 2000.